

Characterization and Modeling of the Purkinje System for Biophysical Simulations

© 2016 by Daniel Romero. All rights reserved.

Characterization and Modeling of the Purkinje System for Biophysical Simulations; Ph.D. thesis, Universitat Pompeu Fabra, Barcelona, Spain

This book was typeset using L^AT_EX2e and output as PDF. Cover: 3D triangular mesh of a biventricular heart model segmented from an MR scan. The model includes in colours an automatically generated Purkinje network. It is filled with fire, representing the electrical activity triggered during ventricular arrhythmias, and it is pumping liquid through the aortic valve. The scene was rendered with Paraview 4.4.0. and the layout done with Microsoft PowerPoint.

This thesis was printed with financial support from Physense (Universitat Pompeu Fabra), CoMM-Lab (Universitat de Valencia) and the Departament de Tecnologies de la Informació i les Comunicacions (Universitat Pompeu Fabra).

ISBN 0-000-00000-0

Characterization and Modeling of the Purkinje System for Biophysical Simulations

Daniel Romero Garcia

PhD Thesis / 2016

Department of Information and Communication Technologies
Universitat Pompeu Fabra, Barcelona, Spain



Supervisors: Dr. Oscar Camara
Universitat Pompeu Fabra, Barcelona, Spain
Dr. Rafael Sebastian
Universitat de València, València, Spain

Reading Committee: Prof. Dr. Javier Saiz
Universidad Politécnica de València, València, Spain
Dr. Maxime Sermesant
Inria, Nice, France
Dr. Sergi Valverde
Universitat Pompeu Fabra, Barcelona, Spain

The work described in this thesis was started in the Center for Computational Imaging and Simulation Technologies in Biomedicine, and completed in the group Physense, Universitat Pompeu Fabra (Barcelona) and the group CoMMLab, Universitat de Valencia (Valencia), Spain.

Financial support for this work was provided by the Spanish Ministry of Science and Innovation through projects CDTEAM (CEN-2005003), and SAFE-PLAI (TIN2011-28067), the European Commission through projects euHeart (FP7-ICT-2007-224495), and the Departament de Tecnologies de la Informació i les Comunicacions de la Universitat Pompeu Fabra.

Dedicada a Zoila -

“Mama vieja, yo le canto desde aquí, esta zamba que una vez le prometí.”

Lito Bayardo

Abstract / Resumen

Abstract - Over the last decade, multi-scale computer models of the heart have helped understanding the complex electrical interactions of its components, as well as electrical disorders and pathologies at cell, tissue and organ scales. The usability of those models depends mostly on their capacity to accurately represent heart anatomy, microstructure and function. However, integrating such a variety of biological data for a given patient is often not possible mainly due to technical limitations, e.g. acquisition of microscopic structural information. This is the case of the cardiac conduction system (CCS), a heterogeneous network of cells responsible for the fast and coordinated distribution of the electrical impulses that triggers the contraction of the heart. The CCS cannot be observed in in-vivo images because the size of its structures is in the order of cellular resolution. The CCS is mandatory in several cardiac modeling applications since it is known to be involved in arrhythmia initiation and maintenance, and plays a key role in other diseases such as left bundle block or bundle branch re-entry VT and fascicular (PK-related) VT and their associated therapies. Existing models developed for simulation of cardiac electrophysiology tend to neglect the CCS or simply emulate its function using non-physiological and simplified approaches.

The aim of this thesis is twofold: firstly, to show the importance of explicitly modeling the CCS structure and function for an accurate description of the electrical activation of the ventricles under normal and pathological conditions, and secondly, to present a novel technique to build automatically the structure of a CCS that meets physiological observations. Pursuing that goal has required an additional multidisciplinary effort to define a full pipeline to build computational models for cardiac electrophysiology simulation, and imaging techniques to acquire and analyze data of the CCS at macroscopic and microscopic scales.

Resumen - Durante la última década, los modelos computacionales multi-escala del corazón han ayudado a mejorar la comprensión tanto de las complejas interacciones eléctricas de sus componentes, como de los trastornos y patologías eléctricas a escala celular, de tejido y órgano. La usabilidad de estos modelos depende principalmente de su capacidad para representar con precisión la anatomía del corazón, su microestructura y su función. Sin embargo, la integración de tal amplia variedad de datos biológicos de un paciente dado a menudo no es posible debido principalmente a limitaciones técnicas, por ejemplo, adquisición de información estructural a nivel microscópico. Este es el caso del sistema de conducción cardíaco (CCS), una red heterogénea de células responsables de la distribución rápida y coordinada de los impulsos eléctricos que desencadena la contracción del corazón. El CCS no puede ser observado in vivo mediante técnicas de imagen clínica porque el tamaño de sus estructuras está en el orden de la resolución celular. Sin embargo, es imprescindible incluirlo en los modelos del corazón, ya que se sabe que está involucrado en la iniciación y mantenimiento de arritmias, y juega un papel importante en otras enfermedades como el bloqueo de rama izquierda o de reentradas rama-rama que desencadenan taquicardia ventricular (VT). Los modelos existentes desarrollados para la simulación de la electrofisiología cardíaca tienden a omitir el CCS o simplemente emulan su función utilizando enfoques no fisiológicos y simplificados.

El objetivo de esta tesis es doble: en primer lugar, mostrar la importancia de modelar explícitamente la estructura y función del CCS para obtener una descripción precisa de la activación eléctrica de los ventrículos en condiciones normales y patológicas, y en segundo lugar, presentar una nueva técnica para construir automáticamente la estructura de un CCS que cumpla con las observaciones fisiológicas. La persecución de este objetivo ha requerido un esfuerzo multidisciplinar adicional, consistente en definir un flujo de trabajo para la construcción de modelos computacionales para la simulación de la electrofisiología cardíaca, además de las técnicas de imagen necesarias para adquirir y analizar datos del CCS a escalas macroscópica y microscópica.

Contents

| | |
|--|------------|
| Abstract / Resumen | vii |
| 1 Introduction | 1 |
| 1.1 The cardiac conduction system | 1 |
| 1.2 Anatomy of the cardiac conduction system | 4 |
| 1.3 Cardiac cell electrophysiology | 9 |
| 1.4 The sequence of electrical activation | 10 |
| 1.5 Computational models of the cardiac conduction system | 12 |
| 1.6 Conclusions | 19 |
| 2 Effects of the Purkinje system and cardiac geometry on biventricular pacing | 21 |
| 2.1 Introduction | 22 |
| 2.2 Anatomical model construction | 23 |
| 2.3 Mathematical modeling of electrophysiology | 25 |
| 2.4 Results and discussion | 27 |
| 2.5 Conclusions | 34 |
| 3 Construction of an anatomical model of the cardiac conduction system | 35 |
| 3.1 Introduction | 35 |
| 3.2 Materials and methods | 36 |
| 3.3 Results and discussion | 38 |
| 3.4 Conclusions | 40 |
| 4 Characterization and modeling of the cardiac conduction system | 43 |
| 4.1 Introduction | 44 |
| 4.2 Materials and methods | 45 |
| 4.3 Results | 50 |
| 4.4 Discussion | 58 |
| 4.5 Conclusions | 61 |

| | | |
|----------|---|------------|
| 5 | Analysis of the microstructure of the cardiac conduction system with confocal microscopy imaging | 63 |
| 5.1 | Introduction | 64 |
| 5.2 | Materials and methods | 66 |
| 5.3 | Results | 69 |
| 5.4 | Discussion and conclusions | 75 |
| 5.5 | Conclusions | 79 |
| 6 | General Conclusions | 81 |
| 6.1 | Overview | 81 |
| 6.2 | Outlook | 83 |
| | Bibliography | 85 |
| | Acronyms | 98 |
| | Curriculum Vitae | 100 |
| | Publications | 102 |
| | Acknowledgements | 105 |

Introduction

1.1 The cardiac conduction system

The fast electrical cardiac conduction system (CCS) of the heart orchestrates and triggers the excitation-contraction function of the heart ventricles. The electrical impulse originates in the sino-atrial node (SAN), the natural pacemaker, located in the right atrium of the heart. From the SAN it advances to the atrio-ventricular node (AVN), which electrically delays the impulse and connects atrial and ventricular chambers. The electrical impulse travels through the His Bundle (HB), which is a collection of heart muscle cells specialized for electrical conduction that transmits the impulses from the AVN to the fascicular branches. The fascicular branches then lead to the Purkinje (PK) system that innervates the ventricles, causing the cardiac muscle of the ventricles to contract at a paced interval. The bulk myocardium is electrically activated at Purkinje-myocardial junctions (PMJ), which are scattered over the endocardial surface. Figure 1.1 shows a simplified representation of the electrical conduction system of the heart.

1.1.1 Pathologies

The distal areas of the CCS, and specifically the PK system, are key to guarantee a physiological sequence of activation and contraction of the heart. There are numerous cardiovascular pathologies that are directly related to malfunctioning of the CCS such as arrhythmias, fibrillation, or tachycardia. One critical case is left bundle branch block (LBBB), a cardiovascular conduction anomaly that can be directly detected from electrograms (ECG). In this condition, the activation of the LV is delayed, which makes the LV contract after the RV, decreasing the heart performance. Other important negative effects of abnormal activation of the CCS are the generation of electrical macro- or micro-reentries. This type of reentry is due to a unidirectional block in the CCS and can give rise to ventricular tachycardia. Another source of problems might originate from the PK system itself,

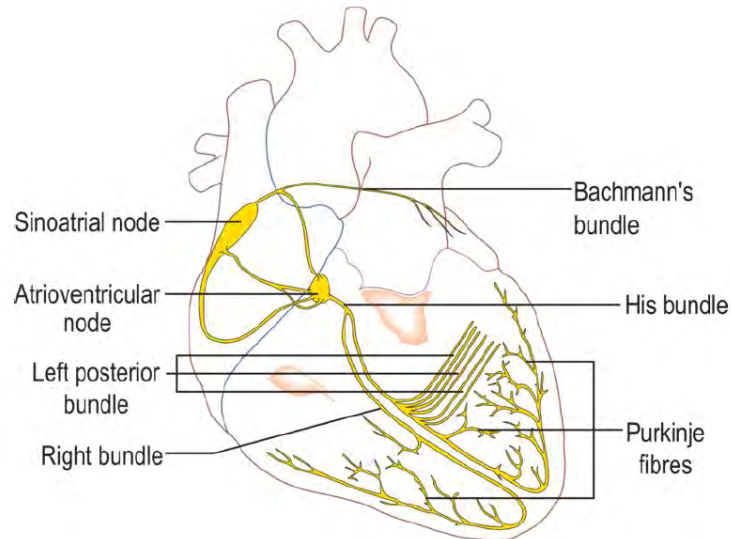


Figure 1.1: A graphical representation of the electrical conduction system of the heart showing the Sinoatrial node, Atrioventricular node, His Bundle, Purkinje fibres, and Bachmann's bundle. Image adapted from Wikipedia¹.

which can produce sub-endocardial focal activity i.e. early after-depolarizations (EADs) and delayed after-depolarizations (DADs), or micro-reentry under certain conditions. Although the role of the CCS in the normal electrical sequence of activation is well known, its functioning in abnormal conditions, or its interaction with electrical disorders that have their origin in other pathologies, such as infarctions, is not well understood yet. So as to better comprehend the underlying systems that prompt certain sorts of arrhythmia, it is critical to look for new tools that permit considering in detail the electrical coupling of the CCS and the myocardium under normal and pathological conditions in a simple way.

1.1.2 Modeling

Computational tools and integrative multi-scale computational models of the heart have the potential to improve understanding, diagnosis, treatment planning and plan interventions for cardio vascular disease. Biophysical models of cardiac electrophysiology are available at different scales [109, 110] and are able to reproduce the electrical activation of the heart. The opportunity of multi-scale modelling spanning multiple anatomical levels (sub-cellular level up to whole heart) is to provide a consistent, biophysically-based framework for the integration of the huge amount of fragmented and inhomogeneous data currently available. The combination of biophysical and patient-specific anatomical models of atria and ventricles allows simulating cardiac electrical activations for a given

¹ <http://upload.wikimedia.org/wikipedia/commons/d/d5/Conductionsystemoftheheart.png>

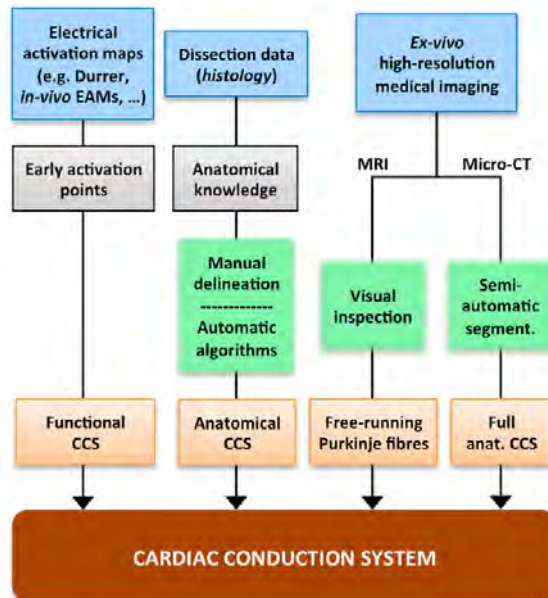


Figure 1.2: Main components required for the development of a cardiac conduction system model. Image from [96].

patient and has the potential for helping in decision-making processes for electrical therapies such as cardiac resynchronization therapy or radio-frequency ablation. One of the main drawbacks of current cardiac computational models is the difficulties for obtaining patient-specific data for all the anatomical components that take part in the electrical activation of the heart. Among them the CCS has remained largely elusive due to the impossibility to observe it in-vivo and the little amount of information available in the literature. Figure 1.2 lists the main components needed for a complete model of the CCS, as proposed in [96], together with the challenging data (e.g. invasive electro-anatomical maps, histology, ex-vivo) that can provide partial information about its anatomy and functional behaviour (i.e. electrophysiology). As a result, the CCS is often not modelled in computational models or is oversimplified. Among the most common approaches followed to avoid explicitly modelling the PK system, though still synchronously activating the ventricles, is the use of excitation points [88]. In this approach, a set of discrete scattered excitation points is placed all over the endocardium. Following the measurements from ex-vivo electrical mapping studies (see Durrer et al. [58]) the points are activated, as small pacemakers, thus creating a virtual activation map. More sophisticated approaches build simplistic PK trees that define the locations of the PMJs based on electrical landmarks [123, 173]. Although simple geometrical models allow including specific PK cellular models and PMJs, none of them tried to reproduce the pattern or structure of the PK system, or its complexity. In the following sections information about the cardiac conduction system, both anatomically and electrophysiologically, including the sequence of electri-

cal activation, from ex-vivo histological or microscopy studies in animals and human cadavers, is discussed. Subsequently, state-of-the-art in structural and electrophysiological models of the CCS is presented.

1.2 Anatomy of the cardiac conduction system

Because of the challenges for identifying conductive tissue, there has been considerable wheel spinning over the last century, often leading to contradictory results, thus controversy abounded. This is partly due to the lack of markers for this specific tissue. The understanding of the PK pattern was delayed for a long time. In 1845 Jan Evangelista Purkinje published his discovery of a part of the heart conduction system that we call PK fibres [81]. He observed these fibres in sheep hearts. In 1906, Sunao Tawara published the results of his two and a half year research. In his publication he described anatomy and histology of the electrical conduction system in several animal specimens and in humans and emphasized the morphological unit of transfer of the AVN to the atrioventricular bundle, bundle branches and PK network [167]. His research was essential for the knowledge of the CCS and PK fibres. Two years later, Einthoven used Tawara's research in the interpretation of the ECG [61]. In 1910, Aschoff [10] and Monckeberg [104] defined the three conditions to identify a structure as a part of the CCS: 1) the cells of the tract needed to be histologically discrete when compared to their neighbors; 2) the cells should be able to be traced from section to section in the histological series; 3) the cells of the tract should be insulated from their neighbors by a sheath of fibrous tissue. The cells of the SAN and of the AVN satisfied the first two criteria, whereas the pathways for the ventricular conduction system satisfy all the three. Several studies described the anatomy of the HB and its branches [7, 58, 100, 148, 167]. To visualize the net structure it is necessary to apply sub-endocardial injections of ink or stains. It is very difficult to observe the Purkinje-net system in humans, because these fibres do not stain well. Ex-vivo histological and microscopy animal data of the PK network is available due to the use of specific stains such as Indian Ink [8], Goldner Trichrome Stain [147] or immunolabeling markers [45], which can be analyzed afterwards from histological and microscopy images. The HB is one of the easiest parts to observe. It extends from the atrioventricular bundle and has a non-branching bundle, which is usually very short, and branches after perforating the septum in several fibres that form the LBB and in a compact group of fibres that form the right bundle branch (RBB), as shown in Figure 1.3 and Figure 1.4.

The most proximal portion of the RBB is identified at the top of the inter-ventricular septum. The bundle branch passes down the septum to the base of the anterior papillary muscle, and after crossing it fans out into multiple free running false tendons terminating on the free wall of the ventricle as a profuse sub-endocardial PK network [8, 148]. Fibres to the septum from the portion of the bundle branch proximal to the anterior papillary muscle are generally not visualized. However, there are consistently tracts of conducting fibres that reflect back from the base of the anterior papillary muscle and the apical free

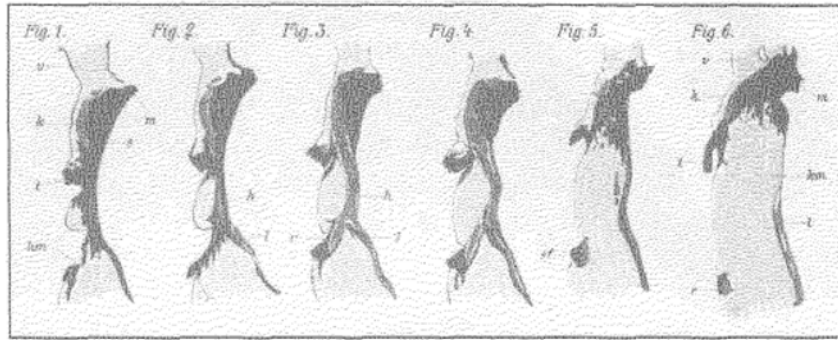


Figure 1.3: Serial examination of section of His Bundle and initial branches from a human heart. Image from [51].

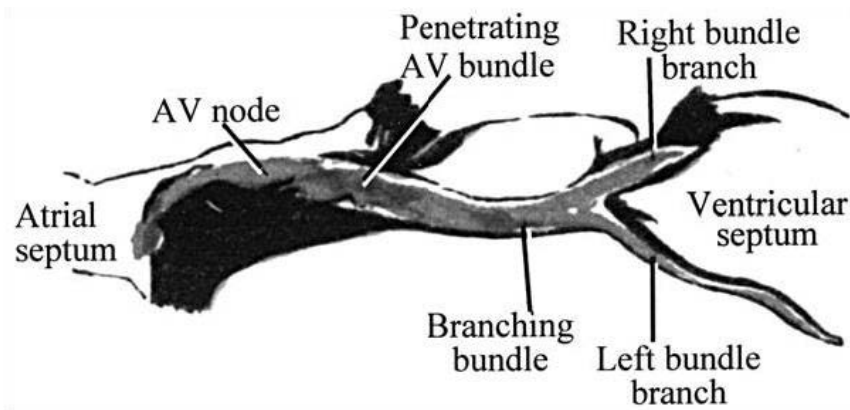


Figure 1.4: His Bundle described by Tawara [167]. Image from [7].

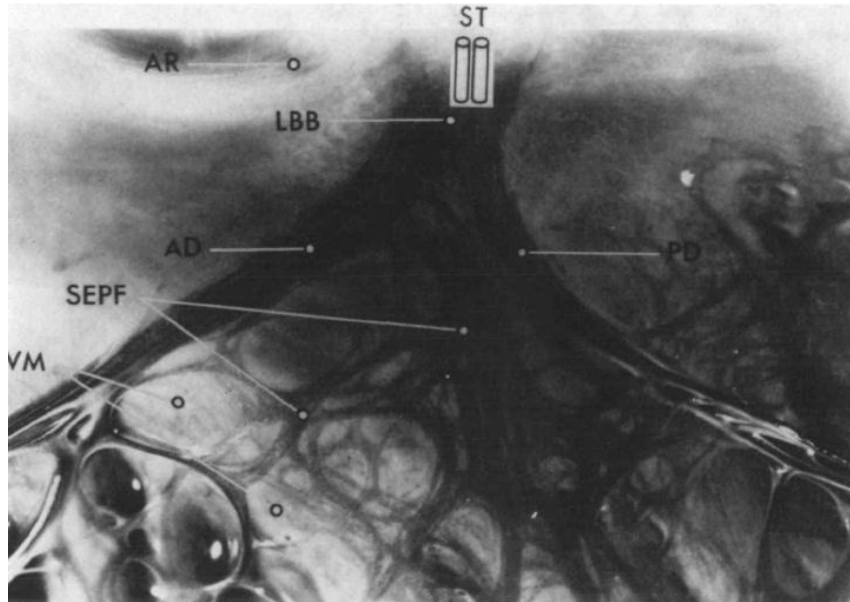


Figure 1.5: *Pertinent anatomic features of the proximal left ventricular conducting system.*
 Image from [107].

wall to the lower portion of the septum. The RBB is anatomically separated from the right septal muscle by fibrous tissue.

The left bundle branch (LBB) is buried deep in the muscle of the inter-ventricular septum and continues to the apex. The gross anatomy of the LBB system is much more complex than that of the right system. The short main LBB divides into two or three divisions high on the left side of the inter-ventricular septum. Large portions of the anterior (superior) division and the posterior (inferior) division course directly toward the two papillary muscles. A profuse sub-endocardial network of interlacing PK fibres courses through the septal endocardium, which is bordered by the two major divisions and the papillary muscles. Figure 1.5 depicts the main LBB and how it bifurcates into an anterior division (AD) and a posterior division (PD) that course toward the apical portions of both papillary muscles (out of picture). A network of sub-endocardial PK fibres (SEPF) is present between the two divisions. The endocardial true ventricular muscle tissue (VM) can be seen between the tracts of conducting tissue. In humans, it usually forks into three divisions: anterior, medial and posterior. The anterior bundle continues to the apex and forms a sub-endocardial plexus in the area of the anterior papillary muscle. The posterior bundle goes to the area of the posterior papillary muscle, divides into a sub-endocardial plexus and extends to the rest of the LV.

The RBB becomes sub-endocardial and forks near the junction between the inter-ventricular septum and the anterior wall of the RV. It passes under the septal endocardium to the papillary muscle and fragments to the network of PK for the walls of the RV.

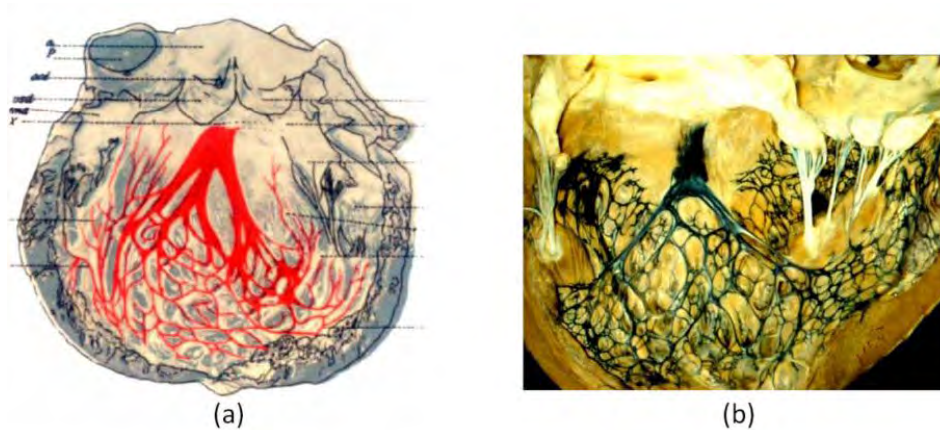


Figure 1.6: Purkinje network in the LV. Tawara's illustration is very similar to the real network in the photograph. (a) Tawara's illustration, showing the three divisions in human left bundle branch. (b) Purkinje network of a calf heart. Image from [167].

The PK network is, as mentioned above, the terminal part of the CCS (see Figure 1.6). In general, the sub-endocardial PK network has an elliptical disposition in both ventricles, as shown in Figure 1.6 (b). In humans, PK fibres only reach the endocardial layer and are connected to the working myocardial cells by intercalated disks. In some species, especially in large mammals, it has been reported the existence of intramural fibres that penetrate the ventricular wall and create new branches or anastomosis, forming a complex three-dimensional network in the ventricular muscle. Ryu et al. found PK cells within the mural myocardium of sheep ventricles, whereas no intramural Purkinje-type cells were detected within the human ventricles (see Figure 1.7) [147]. In the sheep septum, every intramural PK cell forms a three-dimensional network throughout the mural myocardium, which proximally connects to the sub-endocardial extension of the bundle branches and distally forms an occasional junction with ordinary working myocytes. Anatomical characteristics of the intramural PK or Purkinje-type myocytes are yet to be fully clarified in mammalian hearts.

Junctions between the PK network and the subjacent ventricular myocytes (PMJ) are electrophysiologically defined components of the CCS, where the electrical impulse is delivered to the sub-endocardial tissue after a certain delay of around 5ms [11, 169, 186]. PMJs are distributed along the course of the PK network that is in contact with the ventricular fibres. In several studies [7, 130, 166] there has been shown the existence of transitional cells between the terminal PK fibres and the ventricular fibres (see Figure 1.8). Transitional cells have been observed in pig, rabbit, dog and goat, but not in human or bovine where PK fibres gradually become smaller and eventually similar to ventricular myocytes.

Using rabbit RV, Cates et al. [40] successfully detected around 170 PMJ by recording unipolar electrograms from 528 electrodes, and studying fast electrical deflections (Purk-

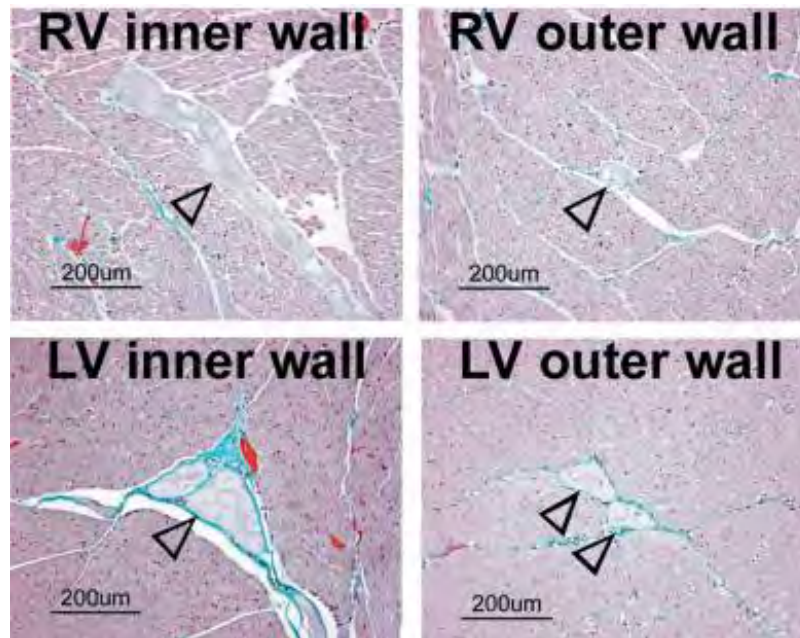


Figure 1.7: Purkinje cells within the right and left ventricular free walls of a sheep heart. The specialized myocyte with distinctive morphologies (open arrows) are found in both the inner and the outer layers of the ventricular walls. Image from [147].

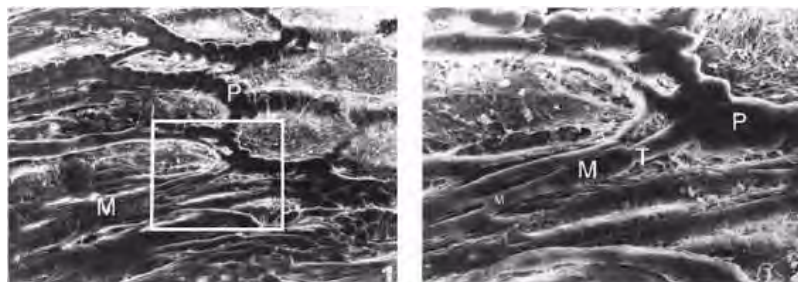


Figure 1.8: Scanning electron micrograph of the transitional cells of the sheep sub-endocardial network (a) and a close-up view of the ruled area(b). P (Purkinje), M (Myocardium), T (Transitional). Image from [166].

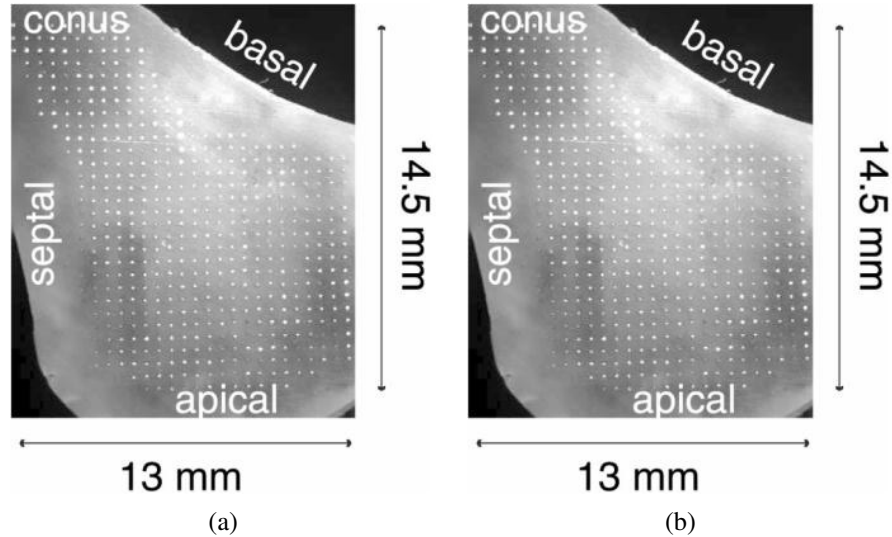


Figure 1.9: Schematic of the preparation including the position for the recording array (a) and (b) means \pm SD for the number of sites with P deflections during sinus mapping and endocardial pacing experiments. Image from [40].

inje) followed by >2 ms slow deflections (ventricular) (see Figure 1.9). They suggested a more continuous PMJ coupling where antegrade and retrograde conduction are mixed, which is in line with new findings that show a high electrical propagation velocity through trabeculae [105]. This hypothesis is supported by observations of ventricular deflections closely preceding PK deflections in endocardial electrograms in sinus rhythm [40], meaning that the PK and myocardial electrical wavefronts advance in parallel in some regions. More recent, studies of activation of PK fibres in pigs [57] and dogs [165] under fibrillation have also shown an intense activity of the PK fibres both antegrade and retrograde. Assuming a homogenous distribution of PMJs and considering the density of electrodes and size and properties of the endocardial rabbit RV [40], the mean number of PMJ can be estimated in the order of hundreds to thousands.

1.3 Cardiac cell electrophysiology

Cardiac excitation involves the generation of the action potential (AP) by individual cells and its conduction from cell-to-cell through intercellular gap junctions. The combination of a locally regenerative process (AP generation) with the transmission of this process through flow of electric charge is common to a broad class of reaction-diffusion processes. AP generation is accomplished through a complex interplay between nonlinear membrane ionic currents and the ionic milieu of the cell. The discovery by Hodgkin and Huxley (principles of nerve excitation) [77], made it possible to relate important properties of membrane ion channels to the generation of the AP. Later, evidence for electric

coupling of cardiac cells through low-resistance gap junctions was established [107]. This property is crucial for the propagation of the cardiac impulse. Over the past three decades, researchers have employed reductionist approaches to define the multitude of ion channels that contribute to transmembrane currents that generate the cardiac AP. For a single cardiac cell under space-clamp conditions, an equation can relate the transmembrane potential (V_m) to the total transmembrane ionic current (I_{ion}). There have been reported differences between AP in PK cells and the rest of myocardial cells. The AP duration (APD) is longer in PK fibres than in ventricular cells [16, 33]. The AP morphology observed in rabbit exhibit a prominent phase 1 of repolarization, a more negative plateau and a significantly longer APD90 (APD AT 90%) compared to ventricular cells [116]. The prolongation of the APD in PK cells compared to ventricular cells also has also been observed in canine fibres [137, 171]. The total amplitude of the AP and the maximal rate of rise of the AP upstroke (V_{max}) are much larger in PK fibres than in ventricular cells.

The heart is known to beat because an automatic electrical impulse is generated by a set of specialized cells. The full CCS consists of different types of those specialized cells that initiate and coordinate the contraction of the heart chambers. This system became understood within the 20th century. Knowledge of the time course and instantaneous distribution of the excitatory process of the normal human heart is of great value for a better understanding of the QRS complex for certain pathologies. To obtain information concerning the time course and instantaneous distribution of the excitatory process in the normal human heart, studies have been made on isolated human hearts and animals using techniques based on electro-anatomical and micro-electrode mappings [58, 107, 123, 173]. The overall activation sequence in healthy subjects is well understood in proximal sections. Distally, impulses of the CCS are transmitted first to the papillary muscles and then through the ventricular wall. At first, inter-ventricular septum is activated, then the RV and the anterior wall of the LV, following the lateral wall of the LV and, finally, the posterior wall of the LV. Figure 1.10 shows the path followed by the activation signal from the SAN to the ventricles (yellow arrows in the figure).

1.4 The sequence of electrical activation

Due to the complexity of the PK network, the distal section of the CCS, the sequence of activation in the ventricles is not fully understood, and only micro-electrode mapping has been able to bring some light into this complex process. Using 870 intramural micro-electrodes Durrer [58] was able to determine three endocardial areas that were synchronously excited 0 to 5 ms after the start of the left ventricular activity potential. These areas increased rapidly in size during the next 5 to 10 ms and became confluent in 15 to 20 ms. The order of activation of the left ventricular areas observed by Durrer was the following: (1) high on the anterior paraseptal wall just below the attachment of the mitral valve; (2) central on the left surface of the inter-ventricular septum; and (3) posterior paraseptal about one third of the distance from apex to base. The last part of

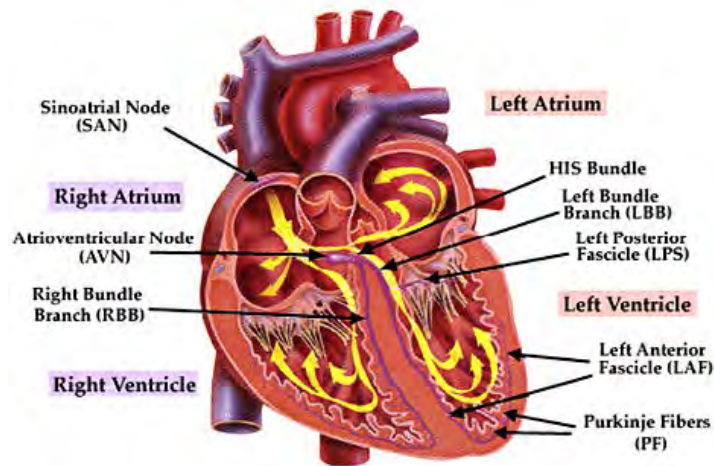


Figure 1.10: *Specialized electrical conduction system of the heart.* Yellow arrows indicate the path followed by the electrical impulses from the SAN to the PK fibres.

the LV to be activated usually was the postero-basal area. Endocardial activation of the RV was found to start near the insertion of the anterior papillary muscle 5 to 10 ms after onset of the LV cavity potential. Septal activation starts in the middle third of the left side of the inter-ventricular septum, somewhat anteriorly, and at the lower third at the junction of the septum and posterior wall. The epicardial excitation pattern reflected the movements of the intramural excitation wave. A nearly completely closed front is present after 30 ms, except at the postero-basal area. At this time, excitation has already reached the epicardial surface of those sites overlying the areas of earliest endocardial excitation. Figure 1.11 depicts the activation sequence obtained for a human subject.

In the different hearts processed in [58] the latest times of activation were: 71 ms (QRS, 0.08 s), 62 ms (QRS, 0.07 s), 65 ms (QRS, 0.07 s), 80 ms (QRS, 0.08 s), and 74 ms (QRS, 0.08 s). Detailed studies by Myerburg et al. [107] helped to better understand the activation sequence of the inter-ventricular septum. This area is especially relevant since it is one of first activated ones and its activation has a large influence due to the organization of the bundle branches. They found that most of the endocardium of the RV free wall is activated simultaneously whereas the LV muscle is activated in an apex-to-base sequence. Right septal activation is from apex to base, and the left septum is activated first at the junction of the middle and lower thirds of the septum and then as a bidirectional wave front toward the apex and the base. In particular, The RV sequence of activation of the conducting tissue starts from the bundle branch and goes to false tendons, and then to the sub-endocardial PK network on the free wall of the ventricle. The major ramifications of the bundle branch are a group of false tendons spreading throughout the free wall endocardium as a network of interconnecting tract of conducting tissue (see Figure 1.12 (a)). These major tracts were activated 10-15 ms and the RBB at the base of the papillary

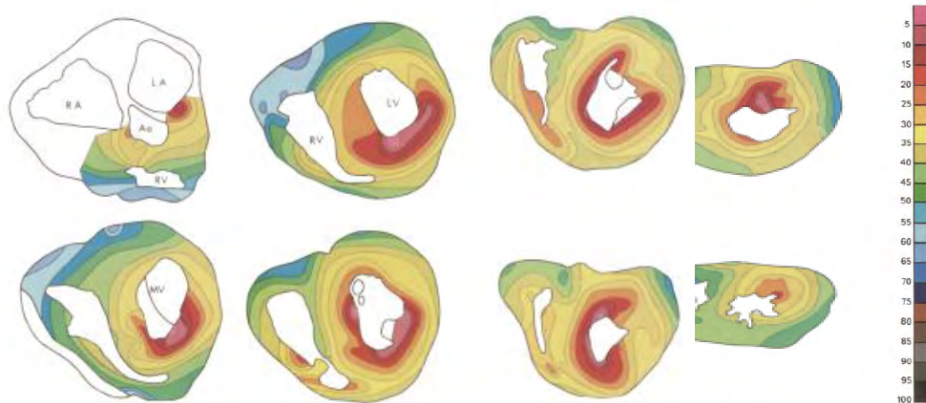


Figure 1.11: Representation of activation sequence by means of isochronal maps at different horizontal cuts of a human isolated heart obtained by Durrer using micro-electrodes. Scale is in milliseconds. Image from [58]

muscle 8 ms after the stimulus. The white numbers on black backgrounds represent intervals from stimuli to PMJ depolarization. The black numbers on white backgrounds are stimulus-to-muscle depolarization times. The earliest PMJs and muscle activated on the free wall are in the apex, but most of the free wall is activated a few milliseconds later. Only the most basal portion of the free wall is activated later (30-36 ms). In the LV septum (see Figure 1.12 (b)) the general pattern of activation of the upper two thirds of septum is from the bundle branch, along the major divisions and sub-endocardial PK fibres, to the junction of the middle and lower thirds of the septum, at which point muscle activation begins and travels back toward the base through ordinary muscle.

More recently, ECGI (Electrocardiographic imaging) has been used to image normal human cardiac activation and repolarization in vivo in seven intact hearts from healthy adults under completely normal physiological conditions [128], as illustrated in Figure 1.13. The first breakthrough occurs in the antero-paraseptal RV region during early QRS and is termed RV breakthrough (RVB). Its timing and location are salient features of normal RV activation. After RVB, additional breakthrough minima appear on RV and LV epicardium. During mid-QRS, more breakthroughs appear in the left-anterior paraseptal region, right-inferior RV, and apical RV region.

1.5 Computational models of the cardiac conduction system

1.5.1 Structural models

The structural models account for the anatomical properties of each tissue or part, e.g. cardiac geometry, the tissue heterogeneity or their structure. The distal section of the CCS

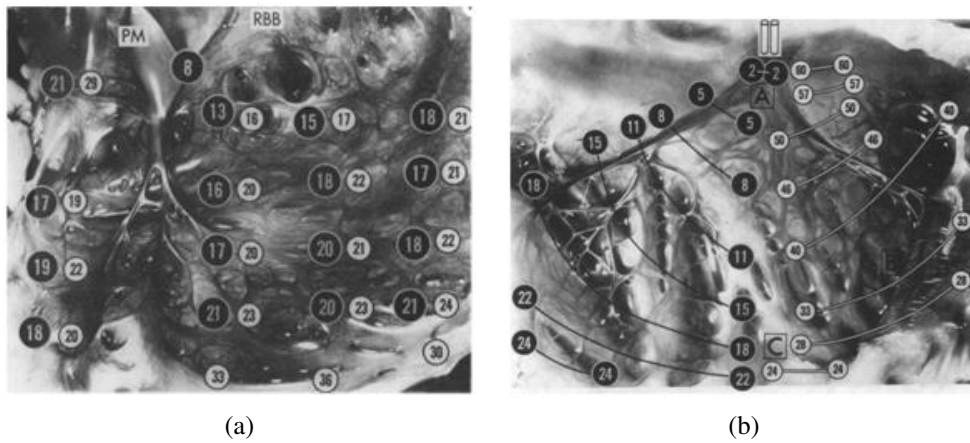


Figure 1.12: Activation of (a) the right ventricular free wall and (b) the left ventricular septum. Image from [107].

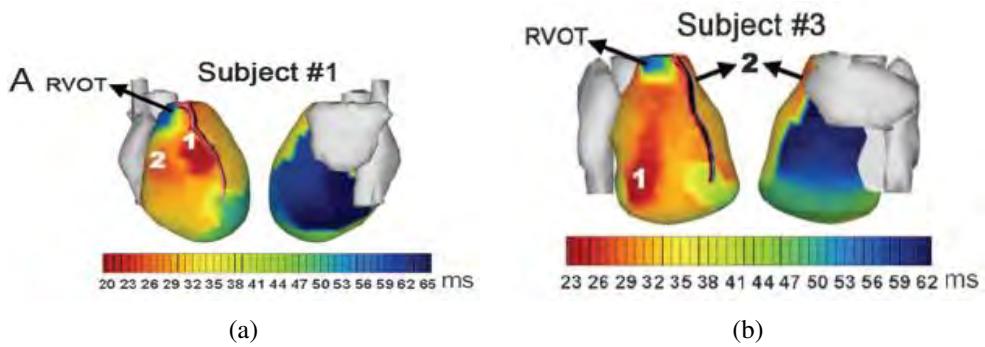


Figure 1.13: Ventricular and atrial isochrones. Ventricular epicardial isochrones from subjects number 1 (a) and 3 (b). Numbers in the figure indicate location of early activation sites. Image from [128].

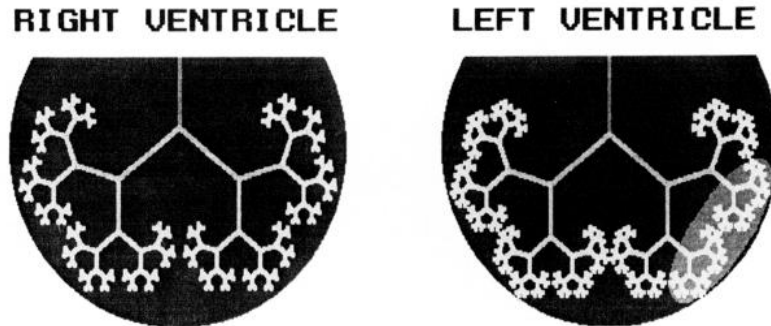


Figure 1.14: *Two-dimensional representation of the model with a damaged region in the LV represented by the light gray area. Image from [1].*

shows a very complicated structure, but it is still crucial to define models which resemble as much as possible to the patterns observed in histological studies. The simplest CCS models used to stimulate the ventricles lacked of any structure, and only aimed at reproducing the electrical activation patterns described in other electrophysiology studies by means of early activated sites. This is still the technique used by many researchers that use phenomenological electrical models or fast endocardial conductivities to simulate an infinite dense PK system. The first CCS models including structural information date from the late eighties and incorporated the HB and a few branches. Aoki et al. [9] model was composed of approximately 50000 cell units (spatial resolution of 1.5 mm.) arranged in a cubic close-packed structure according to anatomical data. The conduction system was composed of the bundle branches and PK fibres, consisting of a few hundred elements. Abboud et al. [1, 20] developed a finite-element three-dimensional model of the ventricles with a fractal conducting system. The two ventricles were modelled as prolate spheroids with a resolution of 0.3-0.4 m, containing around half a million elements. The PK system was modelled like a self-similar fractal tree, assuming that the shortening factor and the bifurcation angle are the same for each generation, as depicted in Figure 1.14. The model was used to simulate the high-resolution QRS complex of the ECG under normal conditions and ischemia.

Pollard and Barr [122] developed an anatomically based model of the human conduction system with almost 35000 cylindrical elements, although it was not incorporated in a ventricular model. The model was validated with activation time data. In their model, they defined a set of 35 endocardial points from which only 4 were extracted from studies of cardiac activation and draw a set of cables to connect them. The cables were highly refined to form small elements suitable for cardiac electrical simulation, and all the PMJ in the model were fully connected forming a closed network. The model did not show a high correlation with experiments, probably due to the little coupling and the scattered and low number of PMJ used.

Berenfeld and Jalife [19] proposed a CCS that also included 214 PMJs, based on

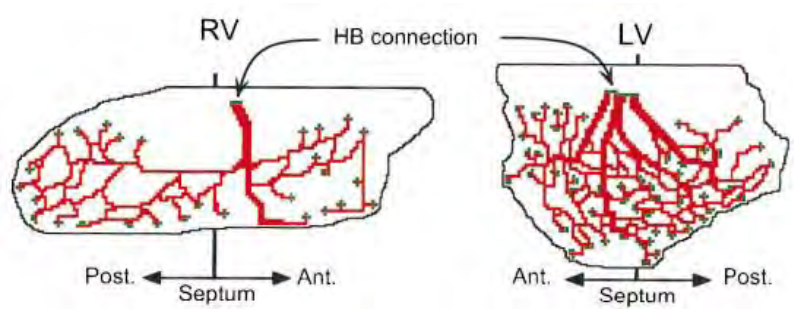


Figure 1.15: A two-dimensional representation of the left and right PK network superimposed on the flattened left and right endocardial surfaces. Post. Indicates posterior wall; Ant., anterior wall. Image from [19].

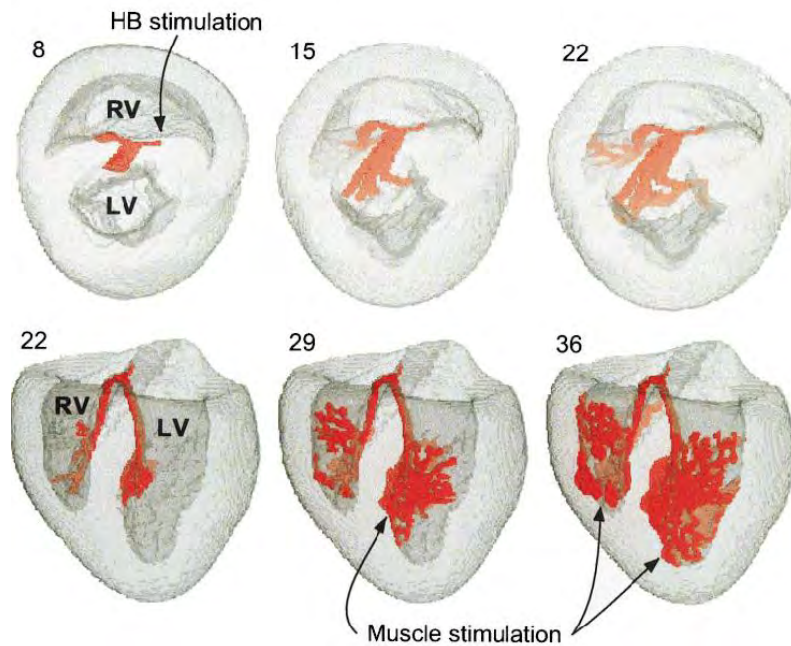


Figure 1.16: Normal excitation with propagation from the HB downstream past the bundle branches and into the right and left septum, and finally into the myocardium. Numbers indicate milliseconds. Image from [19].

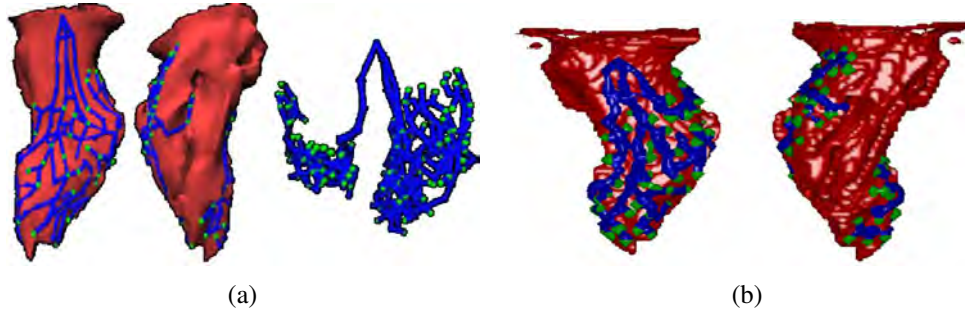


Figure 1.17: *The geometry of the conduction system observed from different angles. (a) Model from Simelius [157] and (b) Model from Ten-Tusscher [173]. The PMJs are shown as light green spheres.*

the procedure of [122], to study Purkinje-muscle reentries. The model tried to mimic the geometry of main PK strands visualized using stains [167]. Figure 1.15 shows the sites of interaction where the PMJs are indicated in green and the sites of interaction with the HB by arrows. Figure 1.16 shows snapshots of the excitation process following an external stimulation of the HB obtained in [19]. Excitation spreads rapidly from the HB (red) to the right and left bundle branches and their subdivisions. More recently, Simelius et al. [157] delineated a PK model for human ventricle by minimizing the difference between simulated isochrones and measurements by Durrer [58] (see Figure 1.17 (a)). Similarly, Ten-Tusscher and Panfilov [173] built the peripheral conduction system using a similar structure, which included 214 PMJs and followed descriptions available in the literature to place the main bundles (see Figure 1.17 (b)). Vigmond and Clements [179] developed a PK model by manually drawing the 2D tree structure in an unfolded rabbit ventricle that was afterwards adapted to the corresponding 3D ventricular heart to study sawtooth effects in the PK system. The model had a high spatial resolution and was made of cubic Hermite elements on the endocardial layer.

1.5.2 Electrophysiological models

Once the structural domain of the heart model is defined, a mathematical model is required to simulate the electrophysiological behaviour. Figure 1.18 summarizes the main components and different approaches for cardiac electrophysiological modelling, as proposed in [96]. Some of the earlier studies were based on cellular automata [101] but these simple approaches were soon replaced by equation-based models, which have two stages: the cellular-level equations and the tissue-level equations. The former are mainly based on the pioneering work of Hodgkin and Huxley that established their formalism more than 60 years ago [77]. In this formalism, the cellular action potential (AP) and the underlying ionic currents are characterized by a system of non-linear first order ordinary differential equations (ODEs) that models the kinetics of individual ionic channels, pumps and exchangers and the electrical interaction thereof [64]. Markov-type models, still under the

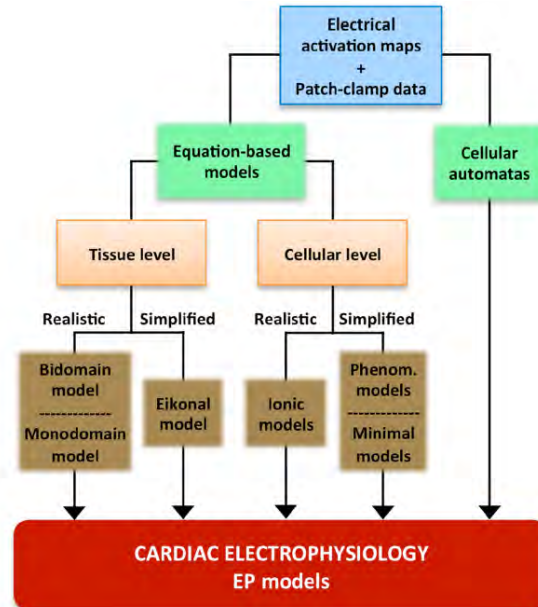


Figure 1.18: Main components and different types of cardiac electrophysiological models. Image from [96].

framework developed by Hodgkin and Huxley, have also been proposed to build more biophysically-based models of ion channels [146]. Observations on the dynamic properties of ion channels have been possible with extensive patch-clamp experiments performed during the past decades. Such information have provided unique data to formulate comprehensive mathematical descriptions of ionic currents of different animal species, heart portions (e.g. atria [99], ventricle [112], Purkinje cells [161]) and pathophysiological conditions (see [64, 136] for reviews on this topic).

Ventricular tissue is heterogeneous in nature, with cardiac myocytes having different properties (e.g. ionic currents and APs) in different regions of the heart. Electrophysiological heterogeneities in the ventricles include epicardial-endocardial [95], apico-basal [164] and left-right [182] differences in ion channels and thus in APs. Some the most advanced EP models include these regional differences such as the one proposed by O’Hara et al. [112] that assigns different behavior to endocardial, epicardial and mid myocardial cells. Other authors [75, 168] have also included other type of regional EP heterogeneities in the atria (e.g. Bachmann’s bundle, crista terminalis or pectinate muscles). Nevertheless, there are not experiments clearly demonstrating the boundaries between these different regions.

Electrical coupling between myocardial cells is needed to ensure current flow from one cell to its neighboring ones. Therefore, the EP models listed above require an additional tissue-level formulation where axial currents flow between cells through low re-

sistance gap junctions. This tissue-level model must include the anisotropic behaviour of the myocardium and the composition of the muscle tissue into intra- and extra-cellular media (domains), which are separated by cell membranes. A mathematical homogenisation of this formulation, referred as to the bidomain model, was originally proposed by Miller and Geselowitz [101]. This model is composed of two partial differential equations (PDEs) that provide extra- and intra-cellular potentials. The bidomain model equations (tissue level) are coupled to the cellular-level ones since membrane potentials depend on ionic currents. As a result, the complete bidomain model consists of the two tissue-level PDEs and a certain number of ODEs that are strongly non-linear. Intra- and extra-cellular conductivity tensors, which are determined by fibre orientation in the myocardium, are included in the two tissue-level PDEs of the bidomain model. In order to simplify this model Roth [143] proposed a mono-domain approach where equal anisotropy ratios are assigned for both intra- and extra-cellular domains, thus the two PDEs become uncoupled. In this way, one PDE is of the reaction-diffusion type and includes all the ionic current ODEs in its independent term. Membrane potentials can be obtained by solving this system, while extracellular potentials can be derived directly from the second ODE once membrane potentials are known.

There is a large variety of complexity in these models considering the number of state variables in the ionic models, which is related to the number of ODEs needed in the formulation. These systems of equations with PDEs and several ODEs represent a challenging mathematical and numerical problem that cannot be solved analytically, thus advanced numerical techniques (e.g. Finite-Element Methods, FEM) that are quite expensive computationally are needed. For this reason it is often desirable to make use of high-performance computing (HPC) facilities to run these models. An alternative, at the expense of losing realism in the mathematical description of the modelled phenomena, is to develop simplified and less mechanistic approaches that replicate observations such as phenomenological models, which in the case of EP models reduce the number of state-variables substituting the actual ionic current descriptions by simple mathematical equations. Fitzhugh [65] proposed the first of these phenomenological models, which was successfully adapted later to cardiac electrophysiology [4, 103]. These models cannot accurately represent complex dynamical patterns of excitation and repolarization since their state variables are not easily related to biophysical correlates in the form of ionic currents. Minimal models [32, 63] were proposed as an evolution of phenomenological ones to partially overcome these limitations by associating each term to actual but simplified ionic currents. The electrical wave propagation can also be simplified with the use of Eikonal models, where the reaction-diffusion equation is replaced by a simpler Eikonal equation [68, 86]. Some authors such as Relan et al. [131] developed a new strategy combining minimal and Eikonal approaches. These hybrid frameworks combining models of different complexity (e.g. mechanistic and phenomenological models) can be very convenient to assimilate available EP data for the most relevant parameters at relatively low computational demands (with phenomenological models) to initialize more realistic biophysical models [34].

1.6 Conclusions

Despite the significant advances in cardiac electrophysiological modelling in the past decades the cardiac conduction system is still often neglected or over-simplified with non-realistic structural models, although its relevance in the (patho-)physiological mechanisms of the heart is well-known. The main reason for this CCS ostracism is arguably the difficulties to obtain good quality data to personalize and validate the models, from the macroscopic (e.g. main bundle branches) to the microscopic (e.g. distal part of the CCS) levels and both structurally and functionally. In consequence, the main goal of this PhD is to develop computational models of heart electrophysiology including the CCS and study its role in a normal sequence of activation, when it is affected by electrical abnormalities and how it is related to existing cardiac therapies. Multi-resolution imaging experiments obtaining structural information at different parts of the cardiac conduction system are performed in order to improve the realism of the proposed EP models.

Research advances on the modelling of the CCS performed during this PhD is thoroughly in the following chapters, all of them adapted from articles published and submitted to high-impact journals. The structure of the manuscript is organized as follows. Chapter 2 presents a computational finite-element model to study the relevance of the CCS, in particular the PK system, for the optimization of Cardiac Resynchronization Therapy, including dilated and hypertrophic hearts. Therefore, Chapter 3 describes the methodology to automatically generate the CCS anatomy for a patient-specific realistic geometry of the left ventricle. Chapter 4 is devoted to an improved version of the CCS anatomical model which is personalized with macroscopic data acquired on experimental models. Furthermore, a detailed morphological analysis of the acquired data is complemented with electrophysiological simulations using the improved CCS model, illustrating the need for incorporating the CCS in EP models to generate realistic sequences of activation. Chapter 5 presents an analysis of the cardiac conduction system at the microscopic scale, characterizing the morphological architecture of the distal section of the Purkinje network on confocal microscopy imaging data acquired from rabbit hearts. Finally some general conclusions are given in Chapter 6.

Effects of the Purkinje system and cardiac geometry on biventricular pacing

Abstract - This chapter studies in a computational finite element model the importance of the cardiac conduction system, and in particular the Purkinje system, for the optimization of cardiac resynchronization therapy. While cardiac resynchronization therapy (CRT) is a recognized treatment for restoring synchronous activation, it is not clear how changes in cardiac shape and size affect the electrical pacing therapy. This study used a human heart computer model which incorporated anatomical structures such as myofiber orientation and a Purkinje (PK) system to study how pacing affected failing hearts. The PK system was modeled as a tree structure that reproduced its retrograde activation feature. In addition to a normal geometry, two cardiomyopathies were modeled: dilatation and hypertrophy. A biventricular pacing protocol was tested in the context of atrio-ventricular block. The contribution of the PK system was examined by removing it, as well as by increasing endocardial conductivity. Results showed that retrograde conduction into the PK system was a determining factor for achieving intra-ventricular synchrony. Omission of the PK system led to an overestimate of the degree of electrical dyssynchrony while assessing CRT. The activation patterns for the three geometries showed local changes in the order of activation of the lateral wall in response to the same pacing strategy. These factors should be carefully considered when determining lead placement and optimizing device parameters in clinical practice.

2.1 Introduction

Cardiac resynchronization therapy (CRT) is a pacemaker treatment for heart failure patients (New York Heart Association class III and IV). It improves systolic function in ventricular dyssynchrony [69], leading to amelioration of functional capacity, inverse remodeling, and reduction of morbidity and mortality [2, 41, 69]. Despite these benefits, clinical trials have demonstrated that around one third of patients do not respond favorably to CRT using standard clinical selection criteria. Sub-optimal resynchronization resulting from current pacing protocols has been proposed as a potential cause underlying treatment failure [2, 46].

As the use of whole heart computational models for electrophysiological simulations becomes more feasible [125, 177], they are starting to be considered as a practical way to explore certain hypotheses that are difficult to study *in vivo*. Various computational studies have undertaken the task of unveiling pathological substrates and assessing treatment methodologies. Current available cardiac models, ranging from single cell [62, 111, 172] to tissue level [76, 124] and organ level [110, 180], are sufficiently accurate to model complex processes, including ion kinetics in healthy and pathological conditions. In many cases, cardiac modeling can be used to investigate phenomena such as drug effects on the electromechanical response and arrhythmogenesis [76, 138].

Although cardiac geometry can be extracted from existing image modalities, many other important features to the modeling process (i.e. myofiber orientation, tissue conductivity) cannot be non-invasively obtained; thus, population based data is used instead. Such is the case for the Purkinje fibers, the fast conducting cardiac tissue responsible for synchronous activation of the ventricles during the cardiac cycle. Despite its relevance, its structure and effects are commonly not considered in cardiac simulations [134]. Previous studies have attempted to model the Purkinje system following anatomical landmarks based on maps of the activation sequence. These maps helped determine roughly the Purkinje myocardial junctions (PMJ) which are contact points for electric impulse transmission between the PS and bulk myocardium [173]. In some electrical modeling studies researchers have estimated a time delay function for stimulating a number of nodes on the endocardium to reproduce the depolarizing pattern of the PK system [67, 180]. Others have used high subendocardial conduction velocities to represent the PK system influence [88]. These approaches to incorporating PK system functionality through bypassing its specific modeling is problematic because it disables an intrinsic property of the PK system: retrograde conduction. Bidirectional electric flow along the PK system might not be necessary for normal sinus activation of a healthy heart, but its contribution is important during analysis of CRT, where the electrodes are positioned close to the distal portion of the PK system.

Another factor to bear in mind during evaluation of CRT candidates with heart modeling is the geometry of the ventricles. Heart failure patients can suffer from pathological conditions that lead to ventricular remodeling. Such are the cases of dilated cardiomyopathy (DCM), characterized by an increase in ventricular diameter [39], and hypertrophic

cardiomyopathy (HCM), a thickening of the ventricular wall [135].

Previous model studies on paced hearts include work focused on the electromechanical effects of pacing each ventricle [87], or optimizing CRT pacemaker settings based on electrical information [134]. The study presented in this paper aims to elucidate changes in the activation pattern due to the interaction of CRT pacing and PK system in normal and pathological human geometries. For this purpose a specific CRT model was built which included a novel and more accurate modeling of the cardiac conduction system than previous approaches. The main advantage of this approach is the possibility to simulate the retrograde activation of the PK system resulting from the pacing. Understanding the activation sequence for a particular patient, given the geometrical characteristics and knowing the effect of the underlying structures, could facilitate selection of appropriate treatments and tailor the CRT devices to optimize therapeutic outcome on an individual basis.

The influence of ventricular geometry and PK system interaction on the paced heart was studied using three models: i) a normal patient biventricular (BV) mesh, to which geometrical changes were introduced to emulate ii) DCM and iii) HCM. The geometrical models were used to simulate electrical activation under normal sinus rhythm and paced conditions in the context of a third degree atrioventricular (AV) block. Complete blockage of AV conduction leaves the task of ventricular activation to the pacemaker alone.

Electrical propagation in cardiac tissue was modeled using the monodomain formulation. For the PK system an embedded structure was built which allowed to model both Purkinje-Purkinje and Purkinje-myocardium properties independently. For BV pacing, the pacemaker leads were model as current injection points at certain sites of the geometries. A pacing protocol was defined using different sequential pacing strategies (inter-ventricular delays), to understand how histological structure and geometry affects cardiac activation for different pacemaker configurations. For each geometry, each pacing protocol was performed with and without the PK system. Furthermore, models with increased conductivity at the endocardium were used to represent a dense PK system as in [88].

Section 2.2 details the construction of the normal BV mesh and the process for applying transformations to arrive at pathologic geometries representing DCM and HCM. Section 2.3 outlines the mathematical models used to simulate cardiac activity and describes pacing protocols. Section 2.4 presents the simulation results with a discussion of the most prominent findings and describes the limitations of the modeling approach. Section 2.5 presents the conclusions from this study.

2.2 Anatomical model construction

2.2.1 Healthy anatomy

A human anatomical model of the right and left ventricles with landmarked endocardial and epicardial surfaces was used in this study. The BV surface mesh was obtained from

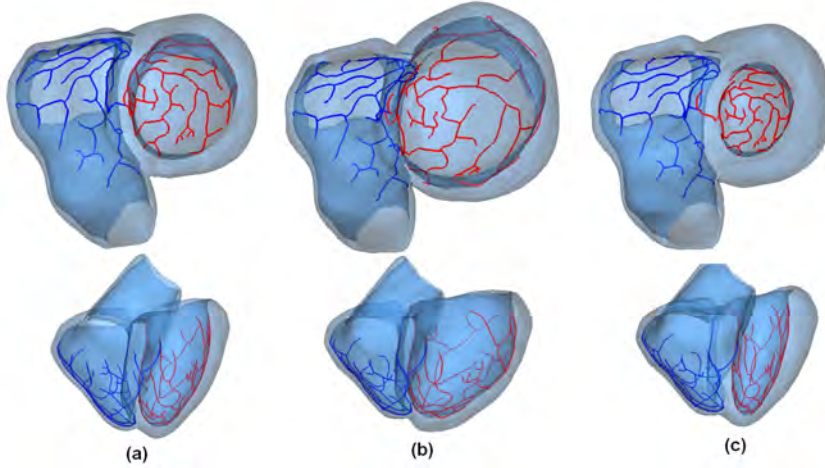


Figure 2.1: Ventricular models. Basal and anterior views of the biventricular surface models: (a) original healthy subject, (b) dilated (DCM), and (c) hypertrophic (HCM) cardiomyopathies. Solid lines represent the RV (blue) and LV (red) branches of the PK system.

the segmentation at the end diastolic phase of a cardiac multislice computed tomography (MSCT) scan of a 53 year old male. A normal anatomy was determined as the subject underwent a diagnostic CT scan. For the patient-specific segmentation, a heart statistical atlas trained and built with 100 MSCT patient scans was used [115]. An active shape model replaced manual delineations by a model based method, and enhanced the transfer of a number of functional substructures incorporated in the atlas (i.e. the PK system) and anatomical labels [66]. The models used for the simulations were all BV since general CRT procedures require implanting a pacemaker lead in each ventricle.

2.2.2 Generation of pathological anatomies

The original surface mesh (see Figure 2.1(a)) was mathematically transformed into two new meshes to represent DCM and HCM. In clinical practice, DCM is diagnosed when the ventricular diameter exceeds 117% of the expected normal, age-adjusted value and HCM is diagnosed when wall thickness exceeds 125% of the expected maximal thickness [35]. Based on these criteria and comparing to typical patients, the HCM mesh was constructed by scaling the LV endocardium to achieve a 50% increase in wall thickness measured radially (see Figure 2.1(c)). For the DCM mesh, the LV endocardial surface was radially displaced to obtain a 50% increase in diameter. Subsequently, the epicardial surface was further dilated to achieve a 30% thinning of the average wall thickness. The latter step was done to assure the property of conservation of mass in the myocardium of dilated (non volume overloaded) hearts (see Figure 2.1(b)).

2.2.3 Volumetric meshing

The three surface meshes were used to create high-resolution volumetric tetrahedral meshes needed for numerical simulations. Volumetric mesh quality was ensured by controlling both the maximum distance between neighboring nodes and the radius-to-edge ratio to assure regularly-shaped elements. The average inter-node distance was smaller than $500\ \mu\text{m}$, with between 2.5 and 3.5 million nodes and between 15 and 21 million linear elements. The conduction velocity at this mesh resolution was tested on a slab of tissue with conductivity values recommended by Clerc [48]. From this we obtained a maximum velocity of 0.67m/s which is in the range of reported values [108].

2.2.4 Myocardial fiber orientation

The fiber orientation was calculated for every element of the mesh, using a mathematical formulation based on the work of Streeter [162] validated by Jouk *et al.* [83]. The Helical fiber structure in the Healthy model was computed with fibers rotating from $+50^\circ$ at the endocardium to -60° at the epicardium. This helical pattern was also used to calculate the fiber orientation for elements in the DCM and HCM meshes. MacGowan *et al.* demonstrated that anatomic fiber angles were not different between normal subjects and idiopathic DCM patients [98].

2.2.5 Purkinje system

The PK system was manually delineated as an independent structure in the atlas, and fitted to the healthy subject surface mesh during segmentation. Terminals were positioned to reproduce the activation sequence reported experimentally by Durrer [58] and more recently by Ramanathan *et al.* [128]. Paths between terminals were built using splines to form a branching network. The resulting PK system model consisted of the bundle branches and 100 segments distributed over the endocardial surface mesh, with no loops in the network. In Figure 2.1, the RV (blue) and LV (red) PK system are superimposed on the ventricles.

The PK system for the pathological meshes was obtained using the previously-described transformation algorithms. It was assumed that in the pathologies modeled, the number of branches in the PK system was unaffected and no terminals were generated or destroyed. This is reasonable, considering that in HCM and DCM myocytes and Purkinje cells do not undergo hyperplasia during ventricular remodeling [35].

2.3 Mathematical modeling of electrophysiology

Modeling cardiac electrophysiology involves two main steps: first, calculating the underlying variations in ionic concentrations across the cellular membrane at each node; second, determining the dynamics of electrical activity at the tissue level.

The electrophysiological cell models used in this study were the Ten Tusscher-Panfilov model [172] for the bulk myocardial cells and the DiFrancesco-Noble model [54] for the PK system. The maximum sodium conductance was increased by a factor of 3 in the DiFrancesco-Noble model to augment the conduction velocity.

For the propagation of the electrical impulse in the cardiac tissue, the monodomain formulation was used [121]. Compared to the bidomain formulation, the monodomain ignores the extracellular field contribution, but it has been demonstrated that for simulations such as those undertaken in this study the difference in results can be neglected [125]. Thus, choosing the monodomain over the bidomain is a matter of computational efficiency since it only requires solving a parabolic equation as opposed to the parabolic plus an elliptic equation. The semi-implicit Crank-Nicholson method was used to update transmembrane potential as in [181, 184], solving a linear system and preserving stability for large time steps.

The modeling of the PK system was performed as described in [179]. The network was constructed from 1D cubic Hermite elements to ensure continuity of current at junctions and bifurcations. Fibers were described as 1D cables that branched at certain positions forming a network structure. The PK system was isolated electrically from the myocardium, with the two tissues connected at PMJs, which were modeled as fixed resistances. Each PMJ was coupled to a group of myocardial nodes within a specified radius. For further information see [30, 179]. Table 2.2 gives the specific parameters used in the cable model, where Ω_{PMJ} is the PMJ resistance and Ω_{PPJ} is the resistance between PK system segments, σ is the intracellular conductivity, and I_{His} is the current injected into the His bundle to trigger the Purkinje activation.

Table 2.1: Constant values used for the Purkinje cable model

| Parameter | Value |
|-----------------------|-------------------------------|
| Ω_{PMJ} | 27 M Ω |
| Ω_{PPJ} | 100 k Ω |
| σ | 0.024 S/m |
| I_{His} | 220 $\mu\text{A}/\text{cm}^3$ |

All the numerical calculations were performed using the Cardiac Arrhythmia Research Package (CARP) [120, 181]. The simulations were run for 230 ms of the cardiac cycle since only the onset of depolarization was of interest.

2.3.1 Application to study electrical activation in CRT

To assess the influence of cardiac geometry and the PK system, a set of standard sequential pacing protocols were conducted on the three cardiac models. Seven pacing scenarios determined by different time delays between the RV and LV pacing leads (inter-ventricular delay, or VVD) were tested. The time delays ranged from 30 ms RV lead pre-activation

(VVD -30) to 30 ms LV lead pre-activation (VVD 30) with intervals of 10 ms between pacing strategies. A third degree AV block was assumed for all the pacing scenarios. Pacing leads were positioned on the apical endocardium (RV lead) and on the lateral free wall epicardium (LV lead) as commonly done in CRT. A physiological activation (starting from the His bundle) was also simulated for each geometry for control purposes. We follow clinical guidelines regarding the positioning of the LV and RV lead. Therefore, we do not consider positioning the leads in other areas such as the the His bundle that could be considered a better position in order to produce physiological activations. The reason is that the insulation that surrounds the Purkinje network plus the lack of Purkinje terminals in that area would prevent the electrical impulse to get inside the system [107] and the re-synchronization will not succeed. The pacemaker lead stimulus was modeled as a 1 mm^3 cube where transmembrane current of $0.05 \mu\text{A}/\text{cm}^3$ was injected for 1 ms.

To further study the contribution of the PK system to the activation sequence, all pacing simulations were repeated in absence of the PK system. Two types of models were used: i) models with physiological conductivity values in all myocardial tissue, and ii) models with increased conductivity values on the endocardium (10% of the wall thickness on the whole ventricles). The increments in the conductivities at endocardium were adjusted to reach a conduction velocity of 2 m/s. With this velocity the LV endocardial depolarization takes place in approximately 60 ms, which is in the range of normal values.

2.3.2 Data analysis

Isochrone maps of local activation times (LATs) in the 3D models were used to study activation patterns during each simulation (Figures 2.2 and 2.3). LAT was calculated as the time with respect to a reference (i.e. initial lead stimulus) at which the potential of a cell reached a threshold (depolarized). Isochrone maps depict the spatial distribution of LATs in 10 ms intervals.

Patterns observed for each pacing scenario and cardiac anatomy were analyzed with cumulative frequency histograms of the amount of activated LV myocardium. Each histogram shows the percentage of LV myocardial tissue activated in time intervals over the depolarization sequence.

In each case, the LV was further analyzed by calculating the mean activation time for each region of the American Heart Association standard 17 segment division. Apart from the overall activation pattern that the histograms convey, it is important to consider the spatial order of activation and study whether the LV segments are properly synchronized. These data are important to search for the scenario that shows a better synchrony between the different walls from the point of view of the electrical activation.

2.4 Results and discussion

In the physiological simulations, the activation sequence was triggered from the AV node, which activates the His bundle. The right and left bundle branches propagate the activation

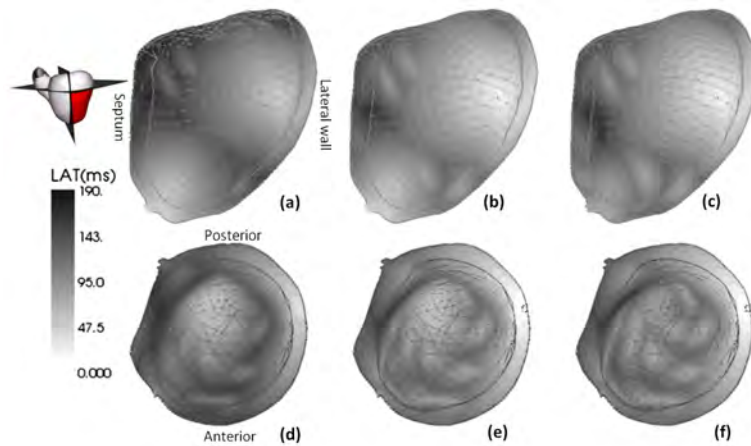


Figure 2.2: Local activation times in DCM with PK system for different pacing strategies. Anterior view of the LV's posterior wall showing the 3D isochronal maps of the local activation times for three pacing scenarios, (a) VVD -30 ms, (b) VVD 0 ms, (c) VVD 30 ms and their corresponding basal views (d)-(f).

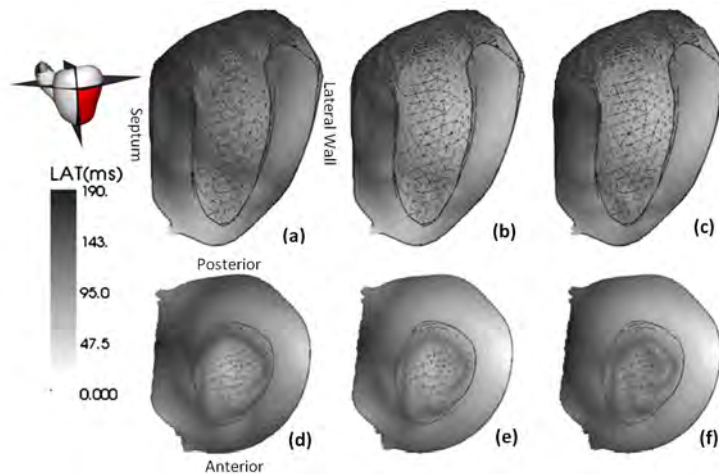


Figure 2.3: Local activation times in HCM with PK system for different pacing strategies. Anterior view of the LV's posterior wall showing the 3D isochronal maps of the local activation times for three pacing scenarios, (a) VVD -30 ms, (b) VVD 0 ms, (c) VVD 30 ms and their corresponding basal views (d)-(f).

to the PK system. Since Purkinje fibers are isolated from the myocardium, they only stimulate the tissue through PMJs. The PK system initiates as many activation wavefronts on the endocardial surface as there are PMJs on the network, giving rise to a rapid sequence of activation that propagates from apex to base and from endocardium to epicardium, in accordance with previously reported values [58, 106]. The time for all ventricular tissue to depolarize (total activation time; TAT) was computed using the first endocardial breakthrough as a starting point. The values were 90 ms for the healthy heart, 105 ms for HCM, and 119 ms for DCM.

In the case of stimulations triggered by a pacemaker the activation sequence presented significant differences as compared to sinus activations. Figures 2.2 and 2.3 show the LATs in a cut plane displaying the LV's posterior wall for the DCM and HCM models in three different pacing scenarios, (a) VVD -30 ms, (b) VVD 0 ms, (c) VVD 30 ms and their corresponding basal views (d)-(f). During ventricular pacing in models with PK system, the propagation of excitation is slower and less uniform than during His stimulation. The stimulus given by the LV lead of the pacemaker gives rise to a wavefront that propagates through the myocardial tissue near the pacing site. After crossing the LV lateral wall, the wavefront retrogradely activates the closest PMJ on the endocardial surface. Once in the PK system, the depolarization spreads rapidly, entering the bulk myocardium through other PMJs and rapidly activating remote areas. For the RV lead, which is placed on the thin-walled right endocardial apex near the PK system, the onset of retrograde activation occurs quickly after the initial stimulus generating a wavefront that travels across the septum at different heights. It contributes to the septal activation, and it also heavily influences the LV's anterior and posterior wall in pacing strategies with VVD -30 ms and VVD 0 ms. Moreover, due to the proximity of the RV lead to the septal wall, the wavefront crosses the septum and contributes to the activation of the LV apex (see Figures 2.2 and 2.3) and initiates retrograde activation of the PMJs on the LV endocardium. For the models with PK system considered, this last effect was only observed for VVD -30 ms. In the other cases the LV PMJ closest to the RV lead generated breakthrough had already been activated by the LV lead. However, RV pacing in models with increased endocardial conductivity always caused retrograde activation of the LV apical endocardium as seen clinically [89]. Consequently, the activation sequence highly depends on the wall thickness and PK system distribution on the endocardial surface. Due to our assumption for the PK system, for which we fitted a unique structure onto the three geometries, the number of PMJs per endocardial unit area varied between geometries. The HCM, with its smaller endocardial surface, had the highest PMJ density, while the DCM had the lowest. Figures 2.2 and 2.3 show the wavefront on the lateral wall crossing from epicardium to endocardium faster in the DCM than in the HCM model; however, once on the endocardium, both impulses have to propagate towards a PMJ and, given the density of these, the HCM's wavefront has a higher chance of finding one.

Figure 2.4 shows histograms of the percentage of activated LV tissue for three pacing scenarios. Simulations with VVD -30 ms ((a),(d) and (g)) show a period of inactivity on the LV myocardium while the wavefront from the RV lead reaches the septal wall.

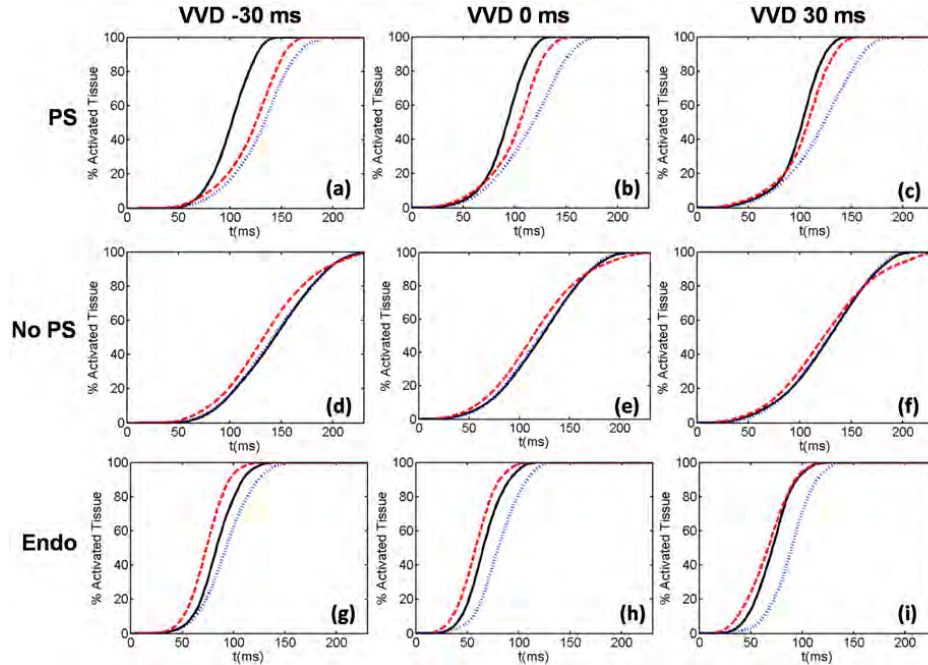


Figure 2.4: Cumulative frequency histograms of the normalized percentage of activated tissue. The lines correspond to: healthy (solid); DCM (dashed); and HCM (dotted) models. The first row corresponds to simulations with PK system while the second and third rows correspond to simulations without the PK system and with normal and increased endocardial conductivities, respectively.

On the remaining plots, activation always starts at 0 ms, although this initial excitation is almost imperceptible on the plots because of the very slow rate of initial rise. As activation spreads, the associated curves start to drift apart. For simulations with an underlying PK system, Figure 2.4 (a)-(c), a high slope represents the contribution of retrograde PK system activation. Thus, the wall thickness and the distance to the closest PMJ determine the instant and rate of the major increase in slope on each curve. The LV PK system is reached first in the healthy model (solid line), whereas in HCM (dotted) due to the thicker wall and in DCM (dashed line), due to the lower density of PMJs, there is a higher delay. Simultaneous activation (VVD 0 ms) produced the most uniform results.

Simulations using myocardial models with normal conductivity values but lacking the PK system take longer to activate (see Figures 2.4 (d)-(f)). The main reason is that the wavefront has to reach remote areas traveling only through bulk myocardium. In Figure 2.4(f), the slowest in completing the activation of the LV was the DCM geometry (230 ms) the one with the largest circumferential distance to cover, while the Healthy and HCM geometries had finished by about 200 ms. The shapes of the Healthy and HCM curves do not differ significantly.

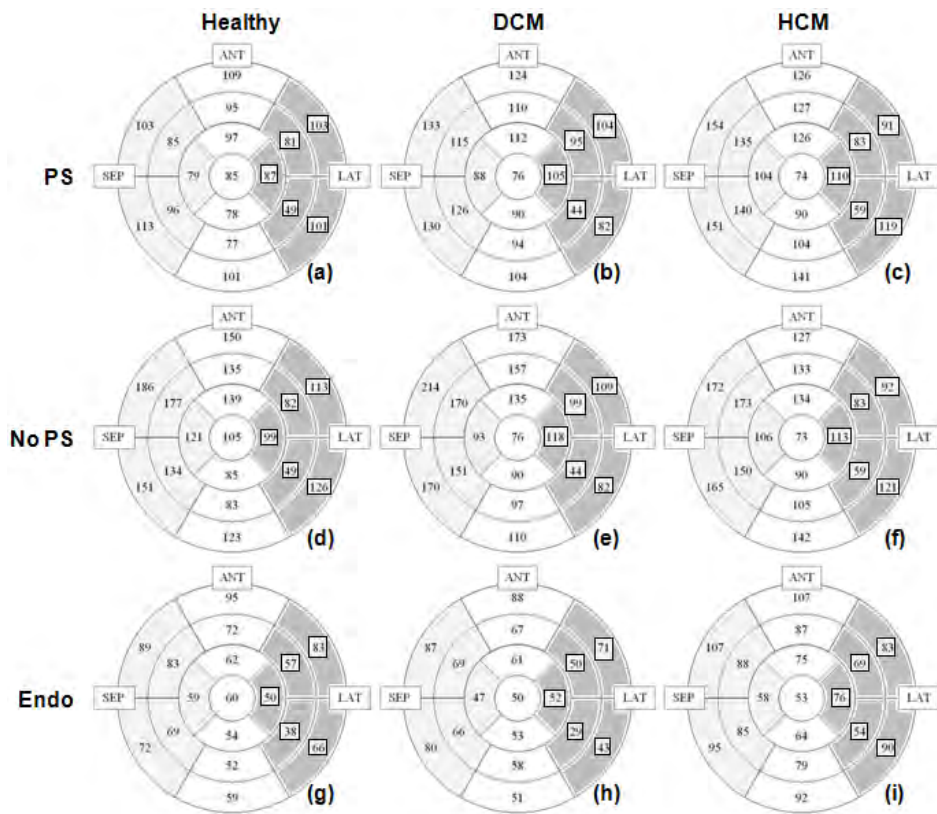


Figure 2.5: Bullseye plots of the AHA 17 segment division, showing LV activation times for simultaneous pacing (VVD 0 ms). The first row corresponds to simulations with PK system while the second and third rows correspond to simulations without the PK system and with normal and increased endocardial conductivities, respectively.

Another example of the dependence of the activation sequence with the PK system distribution is illustrated in Figure 2.4(c) (VVD 30 ms). In this figure the curve representing the HCM model (blue; dotted) achieves its maximum slope later than the other geometries. This can be attributed to the fact that retrograde excitation in the HCM occurs later than in the healthy or DCM hearts. While the excitation wavefront is still propagating through the thick ventricular wall in the HCM model, it has already reached a PMJ on the endocardial side in the other two cases. Notably, the trajectory of this curve is nearly indistinguishable from the activation histogram for the HCM heart with no PK system (Figure 2.4(f)).

In Figures 2.4(g)-(i) the curves correspond to models without PK system but with increased endocardial conductivity. This implies the assumption that every node on this layer behaves as a PMJ, explaining the very steep slopes of the curves. Moreover, it also implies that the retrograde activation for these models was only dependent on wall thickness. As a consequence, the DCM model, which has the thinnest ventricular wall, was always the fastest to depolarize (shortest TAT), followed by the Healthy and HCM models. Another aspect to note on these simulations is that the depolarization caused by the RV lead reached the LV apex at the endocardium and initiated rapid activation wavefronts that contributed greatly to LV depolarization. This effect is highlighted in the DCM curves, which tend to move closer to the Healthy curve as the pacing shifts from RV pre-activation to LV pre-activation (see the distance between the dashed and the solid line, which diminishes from Figures 2.4 (g) to (i)). Nevertheless, this modeling approach is fundamentally inaccurate, since PMJs are not homogeneously distributed with extremely high density on the endocardium [58, 88]. Therefore the time required to retrogradely activate the PK system is neglected.

The bullseye plots (see Figure 2.5) correspond to VVD 0 ms with the possible combinations: the three geometries with PK system, no PK system with normal conductivity values, and no PK system with increased endocardial conductivities. Results from models with PK system when compared to results from models with an absence of the PK system and normal conductivity values indicate that corresponding geometries have very similar mean activation values for the lateral wall (pairs (a)-(d), (b)-(e), (c)-(f)). This highlights the role of the LV lead alone on this task. In contrast with lateral wall, the septal activation on these plots indicates a significant delay between corresponding models.

Intra-ventricular dyssynchrony is referred to as a marked delay of the onset of contraction between the septal and LV lateral wall. One potential treatment is a CRT device with the LV lead positioned at the site of longest delay. Therefore, the electrical activation as displayed on the bullseye plot conveys information that can be associated to intra-ventricular dyssynchrony. The analysis of activation sequences across geometries with PK system (Figures 2.5 (a), (b) and (c)), shows the propagation wavefront on the septal wall always following an apex to base pattern. However, this pattern is lost for the lateral wall activation due to the action of the LV lead in the mid postero-lateral wall. Moreover, in this region, the order of activation depends on the geometry. Within models lacking the PK system but with normal conductivity values (Figures 2.5 (d), (e), (f)) the apex to base

activation pattern of the septal wall is preserved, although with a significant prolongation in activation compared to with-PK system counterparts. This same pattern is observed in models with increased conductivity values (Figures 2.5 (g)-(i)) which have the earliest onset and fastest depolarization of the LV's septal and lateral wall.

Our simulations show that the mean activation times of the septum and the lateral wall are more synchronous and physiological in models with PK system (see Figure 2.5) as compared to models without PK system, which highlights the role of the PK system in maintaining synchronicity between the walls of the ventricles by minimizing their activation delay. The models with normal conductivity values and no PK system showed a prolonged activation on their histograms and an activation widely spread in time when compared to simulations with PK system. TAT is associated to the QRS interval, an index that is used to assess the CRT optimization [84]. Thus activated tissue histograms can be interpreted as a global index of intra-ventricular synchronicity. Simulations with lower intra-ventricular delays, as displayed on bullseye plots, showed a higher maximum slope and a reduction of TAT.

2.4.1 Limitations of this study

The use of computer models to study and predict the response to specific therapies is still in an early stage. The uncertainty of basic physiological constants, coupled with the spatial heterogeneity, is a clear source of concern.

The ionic models used come from two different species. Since only the onset of depolarization was of interest, propagation velocity was of primary importance. To this end, sodium conductance in the PK system was adjusted, and junctional parameters were tuned to properly model propagation across the PMJs. Differences in action potential duration between the two ionic models did not affect the results. For future studies involving repolarization, a more realistic human ionic model of Purkinje fibers should be implemented.

Even though we were able to show the importance of the PK system in the electrical activation and its effect in CRT, the PK system model needs to be improved. The density of terminals in the system is lower than it has been reported in histological studies [100], and therefore delays in the initial activation could be observed. The time to reach the PK system from a lead can be affected by the density of terminals. A specific study to find out a more accurate density and ramification model of the PK system remains to be done.

Invasive techniques, such as electrical mapping are among the few in-vivo studies that can be used to validate the functioning of the heart electrical system. Although the data is sparse and difficult to interpret, a validation based on these recording remains to be done. This is a very challenging step that requires specific techniques in order to bring together electrical and geometrical properties of the heart.

2.5 Conclusions

We have presented a cardiac electrical simulation study to assess the importance of anatomical and histological substructures on the paced heart. The computer model includes important substructures, such as the PK system and myocardial fiber orientation based on a mathematical formulation. The branching Purkinje structure was approached by manual delineation following anatomical landmarks and its electrical behavior was modeled as a 1D cable network [179]. The model is able to simulate the electrical activation produced by a BV pacemaker and reproduces the effect of retrograde activation at PMJs.

The results showed that the use of a detailed and sophisticated PK system is vital to account in simulations with CRT. Its retrograde conduction property is important to determine the synchronous activation between the LV walls. The usage of models without a PK system can over estimate the degree of intra-ventricular dyssynchrony.

Although while pacing from the epicardium it is not possible to reproduce a physiological pattern, it can however maintain the most electrophysiological resemblance (apex to base) depending on the pathological structure. Applying the same pacing strategy to different models elucidates important local variations, made manifest by differences in activation pattern. Between geometries for a given VVD, the most notable effect on the activation pattern is seen on the lateral wall, where the apical and basal segments changed their order of activation. This should be considered in clinical practice at the moment of the LV lateral wall lead positioning to improve the outcome of the procedure. Further work on simulations should test different lead positions to achieve this goal.

Table 2.2: Constant values used for the Purkinje cable model

| Parameter | Value |
|-----------------------|-------------------------------|
| Ω_{PMJ} | 27 M Ω |
| Ω_{PPJ} | 100 k Ω |
| σ | 0.024 S/m |
| I_{His} | 220 $\mu\text{A}/\text{cm}^3$ |

Construction of an anatomical model of the cardiac conduction system

Abstract - This chapter presents a methodology for the automatic construction of a ventricular model of the cardiac conduction system (CCS), which is currently a missing block in many multi-scale cardiac electro-mechanic models. It includes the His bundle, left bundle branches, and the peripheral CCS. The algorithm is fundamentally an enhancement of a rule-based method known as the Lindenmayer systems (L-systems). The generative procedure has been divided into three consecutive independent stages, which subsequently build the CCS from proximal to distal sections. Each stage is governed by a set of user parameters together with anatomical and physiological constraints to direct the generation process and adhere to the structural observations derived from histology studies. Several parameters are defined using statistical distributions to introduce stochastic variability in the models. The CCS built with this approach can generate electrical activation sequences with physiological characteristics.

3.1 Introduction

The cardiac electrical conduction system is formed by a network of fibers, which rapidly propagates the electrical impulse from the sino-atrial node to the peripheral cardiac conduction system (CCS) or Purkinje network [107]. Purkinje-myocardial junctions (PMJ)

Adapted from: Sebastian R., Zimmerman V., **Romero D.**, Frangi A.F. Construction of a Computational Anatomical Model of the Peripheral Cardiac Conduction System. *IEEE Transactions on Biomedical Engineering*, 58(12): 3479-82, 2011.

scattered over the ventricular endocardial surface are the only points of connection between the CCS and the bulk myocardium, in species like humans and rabbits [107]. The structure of the CCS determines the order and timing of activation of the ventricles. Therefore, it is key to reproduce normal and pathological cardiac activation through multi-scale biophysical modeling. Combining patient-specific anatomical models of the heart with detailed computational models of cardiac electrophysiology has the potential to help in decision making in cardiac rhythm management therapies such as cardiac resynchronization therapy. However, the CCS is a complex structure, which can not be imaged in-vivo. Only data available is obtained from histological studies, by specific inks that highlight the structure (Indian Ink [8]) and markers used for confocal microscopy. Most computational models of the CCS have only accounted for the PMJ location and activation times indirectly and based on electrical mapping studies. More recent approaches included the structure of the His bundle (HB) and a few main large branches using a manual delineation on the endocardium [173] or free-running Purkinje strands from segmentation of high-resolution MR of ex vivo animal models [175]. Innovation on the modeling of the CCS was only introduced in recent years by [80], where they presented a method for generation of a tree-like structure on a 3D endocardial surface based on a rule-based method known as the Lindenmayer systems (L-systems). The lack of anatomical constraints on this algorithm results in regular unrealistic anatomical structures.

In this paper, we present a methodology to automatically build a ventricular model of the CCS, including His Bundle, main branches and peripheral CCS. The core algorithm is fundamentally based on L-systems and corresponds to an evolution of our previous CCS models [139, 188]. Our improvements over the previous approaches are better realism and improved model flexibility by a set of user-defined parameters and rules that control the outcome of the generative process and adhere to the available knowledge on the CCS.

3.2 Materials and methods

3.2.1 Ventricular modeling

A left ventricular model (LV) was segmented from a MSCT scan to generate the Purkinje networks [187]. Anatomical landmarks were added automatically to locally guide the generation of the Purkinje tree. The LV was meshed with tetrahedra. The micro-structural arrangement of the cardiac tissue was approximated at each tetrahedral element by calculating the fiber orientation according to Streeter measurements as in [141].

3.2.2 Purkinje network modeling

The CCS generative algorithm deploys the network from proximal to distal regions in three consecutive stages. At each stage, specific parameters are used to build the network and generate a characteristic portion of the Purkinje tree. The first stage is guided using fixed landmarks in the LV model to add the His bundle and left bundle branch. The latter

is formed by three subbranches that extend to the apex, the anterior and posterior walls, where the insertion of the papillary are located. Several subbranches might be generated to interconnect those branches. Figure 3.2 (a) shows the results after the first stage. After reaching the apex and papillary muscle insertion, points all the branches are forced to turn up to the basal region. The length of those branches is bounded by a parameter, which is function of the LV longitudinal-axis length to avoid PMJs close to the base. The second stage generates the core or backbone branches (PKBB) of the peripheral CCS, which span over most of the endocardium but the basal areas. These branches will cover the endocardium as a 'fishing-net' [8], forming polygonal irregular shapes. The expansion process of each strand is controlled by an L-system, which encodes geometrical rules that will give rise to the final pattern. The third and last stage forms the terminal branches (PKTB), which eventually connect to the bulk myocardium by PMJs at specific points. These branches are shorter than PKBB and fill the space let by the larger polygonal structures. The procedure used to grow PKBB and PKTB is the same, based on stochastic L-systems, but with different parameters. Two rules are defined for the growing procedure, a L-rule and a Y-rule [188], which determine the angles between parent-child branches and therefore the overall pattern. L-rule produces a longitudinal growth, whereas Y-rule produces a wider expansion over the endocardial surface. There are two additional types of branching parameters, distribution of angles and distribution of lengths as depicted in Figure 3.1. In addition, over the expansion branches take into account the areas surrounding them to avoid collisions, if possible, by gradients that keep them away from each other. Under certain conditions each branch might intersect with one another and will form a closed loop. The total number of desired branches in each stage needs to be established, giving rise to different densities of branches and PMJs. They are not allowed on basal regions or at upper section of the septum. The selection of input parameters for each stage is the most critical part, since it will determine global and local i) patterns, ii) PMJ density, iii) inhomogeneities, iv) sequence of electrical activation and v) total activation time (related to QRS width).

3.2.3 Electrophysiology modeling

The electrical propagation in the myocardium was modeled using the monodomain equation, and the Luo-Rudy 1991 [97] ventricular cell model of ion kinetics. Purkinje strands were modeled as an uniform signal propagating at a constant speed of 3 m/s. PMJs were the only connection points to the tissue and generated an intra-cellular current that triggered the activation of its surrounding ventricular nodes within an area of 1 mm³. All the electrophysiological simulations were performed with CHASTE [22]. We simulated 120 ms of cardiac activation.

3.3 Results and discussion

The presented methodology was used to build CCS models with different terminal density and structure. Input parameters show a great dependence among them and therefore a top-down procedure, from HB to PKBB and PKTB helped to understand the resulting trees. Under visual inspection the backbone of the model shows a branching pattern similar to anatomical studies [8, 107]. First of all, the PKBB define the initial expansion and overall polygonal structure. The ratio between branch lengths PKBB/PKTB is important since PKTB end up growing in the spaces left by the PKBB. The distribution of new PKTB branches (buds) that come out from the PKBB can be considered to follow a Poisson distribution along the branches. Therefore, PMJs are expected to be distributed over the entire endocardium if generated with enough density. Locally, PKTB length will determine the distance between PMJs and hence how clustered they are. By restricting the minimum distance between PMJs, the local density can be controlled to go from a clustered model to a homogeneously distributed one. The algorithm is competitive and colonizes the different regions by growing new branches and considering the proximity of surrounding branches (calculated as a gradient) over its expansion. When intersection between branches cannot be avoided for a given set of rules, the algorithm either stops growing a branch or merges it generating a loop. A combination of rules and parameters allowed to control how straight or curly are the branches being laid on the endocardium.

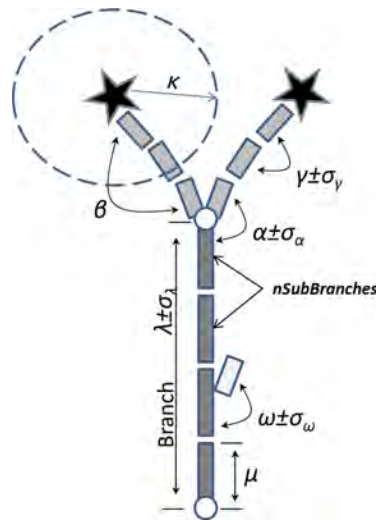


Figure 3.1: Parameters for the CCS generative process. Distributions of branch angles and lengths used during the network growing. Each branch is divided into small segments to allow curved branches. Angles between branches (α), between consecutive segments (γ), between first-last segment (β), and for new branches grown from inserted buds (ω) are defined. The branch length (λ) and segment length (μ) must be also defined. A parameter κ can be used to locally control the maximum density of terminals in an area.

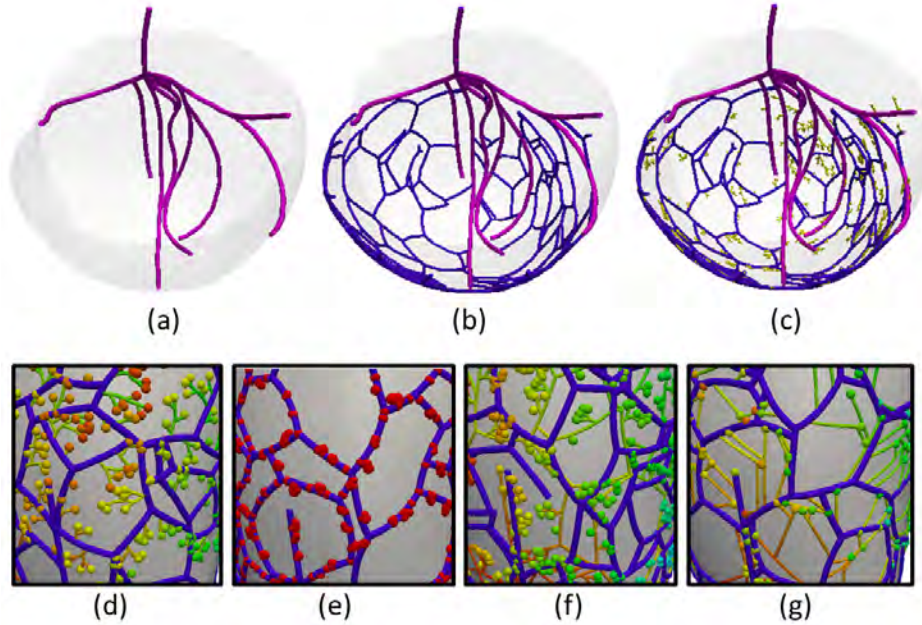


Figure 3.2: Purkinje network model. Purkinje model automatically generated on a human LV endocardial geometry. (a)-(c) show the basal view of the Purkinje network overlaid as a set of branching structures at stages I to III of the expansion algorithm, respectively. Thick blue branches represent the PKBB and thin yellow branches are the PKTB that grow from backbone. PMJs are represented by small spheres for which color indicates the order of activation. (d)-(g) show four different Purkinje network configurations taken from the lateral wall. Differences in branching curvature, density, length, number or homogeneity of PMJs can be observed.

This is mainly controlled by the rule (Y-rule, broad expansion and L-rule, longitudinal expansion) and three normal distributions that define branch angles for a given scale, between consecutive scales (backbone and terminal) and within a branch, i.e. between consecutive subsegments of a branch (see Figure 3.1). In addition, the total curvature of a branch is bounded to avoid non-physiological patterns, such as fully-circular or spiral shapes. PMJ density is globally controlled by the number of PKTB, which is of great importance since it has a direct effect in the total activation time (TAT). Therefore, the number and density of PKBB will affect the overall order of activation and PKTB number and PMJ density the local timing and speed. Table 4.2 summarizes the values used for the most important used-defined input parameters.

Since there is no histological information to set the algorithm parameters, we study their effect on the pattern by using the model. The main effect of each parameters is summarized in Table 4.2 and observed in Figure 3.2 (d)-(g). The most common problem was observed when PKBB did not reach distal regions, preventing the deployment of

Table 3.1: Effect of parameters in Purkinje model

| Parameter | Description | PKBB/PKTB | Affect |
|---------------|----------------|----------------------|--------|
| Rule | Growing rule | Y / L | |
| α | Branch angle | $60 \pm 0.1^\circ$ | (1,4) |
| γ | Segment angle | 5° | (2,4) |
| λ | Branch length | $6.0/2.0 \pm 0.3$ mm | (1,2) |
| ω | Bud angle | $6.0/2.0 \pm 0.3$ mm | (1,2) |
| λ/μ | Segment number | 20 | (2,4) |
| Br_{max} | # branches | 200/300 | (2,3) |
| Bd_{max} | # Buds | 30/150 | (2,3) |

BB: backbone branches; TB: terminal branches

1: curvature; 2: density; 3: overall morphology; 4: loop density.

PMJs, or when the number of backbone buds was small decreasing the density of terminal branches. In both cases, highly inhomogeneous trees were obtained. Low resolution trees, i.e trees built with few number of elements per branch produced straight branches mainly forming loops.

One of the models was used to simulate and study the electrical activation sequence (see Figure 3.2 (a) and (b)). The resulting model had 9K segments for the backbone, 16K segments for the terminal section, and a total of 853 PMJs. The activation sequence was simulated as a sinus activation and resembled remarkably to studies in human LV [58]. TAT of the endocardium alone was of 40ms, while the TAT for whole LV, from the initial breakthrough to the latest activated node of the LV was 70 ms. Both values are within physiological range for normality (see Figure 3.3).

3.4 Conclusions

A method to automatically build a realistic CCS has been presented. Networks are grown by using a set of user-defined parameters and mandatory hard-coded rules that control the main characteristics of the structure and ensure a more realistic result. We show that CCS structures built with this approach generate electrical activation sequences within physiological range without further user interaction than selection of the input parameters. Given the importance of the CCS network to simulate realistic cardiac activation sequence and the impossibility of obtaining the patient-specific CCS structure, an stochastic CCS model might help to achieve more accurate simulation results.

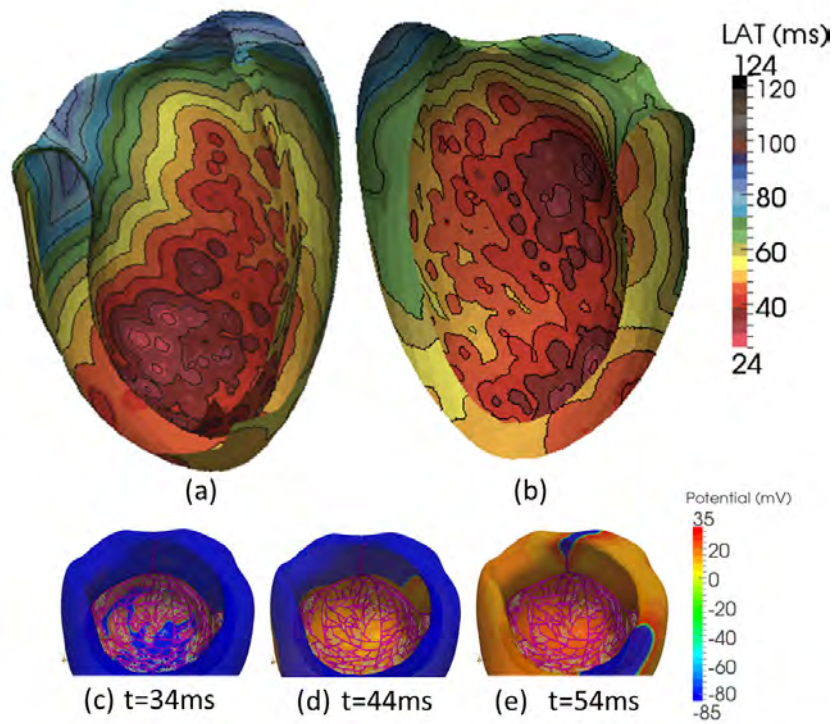


Figure 3.3: Local activation times. An electrical activation sequence obtained for a model that included the embedded Purkinje network shown in Figure 3.2 (a). Left side corresponds to the septal wall that is first activated in its lower third. Right side corresponds to the lateral wall. Latest activated areas belong to the postero-lateral wall in the basal area. Isochrones of local activation times (LATs) are binned in blocks of 5 ms. LATs are given in milliseconds.

Characterization and modeling of the cardiac conduction system

Abstract - This chapter presents a methodology to extract morphological macroscopic information about the cardiac conduction system and an extended algorithm to use that information to build computational models for cardiac simulation of electrophysiology. The development of biophysical models of the heart has the potential to get insights in the patho-physiology of the heart, which requires to accurately modeling anatomy and function. The electrical activation sequence of the ventricles depends strongly on the cardiac conduction system (CCS). Its morphology and function cannot be observed in vivo, and therefore data available come from histological studies. A review on data available of the peripheral CCS including new experiments is presented. In order to build a realistic model of the CCS a procedure to extract morphological characteristics of the CCS from stained calf tissue samples has been developed. A CCS model personalized with our measurements has been built using L-systems. The effect of key unknown parameters of the model in the electrical activation of the left ventricle has been analyzed. The CCS models generated share the main characteristics of observed stained Purkinje networks. The timing of the simulated electrical activation sequences were in the physiological range for CCS models that included enough density of PMJs. These results show that this approach is a potential methodology for collecting knowledge-domain data and build improved CCS models of the heart automatically.

4.1 Introduction

The cardiac conduction system (CCS) is a heterogeneous network of cells responsible for the fast and coordinated distribution of the electrical impulses that triggers the contraction of the heart. It was first characterized by Tawara in 1906 [167], who described the atrio-ventricular (AV) conduction axis. In the ventricles, it is composed of the His bundle (HB) and bundle branches (BB) that are connected to the most distal section, often called peripheral cardiac conduction system or Purkinje system. In species such as rabbit, dog or pig it has been observed that the Purkinje system is electrically connected to the myocardium muscle through transitional cells or Purkinje-myocardium junctions (PMJ) distributed throughout the ventricular sub-endocardial layer [114, 169]. The morphology of the distal section of the CCS plays a key role in the synchronous activation of the ventricles, since it dictates the starting points of activation and therefore the electrical activation sequence [58, 100, 107].

Over the last decade, multi-scale computer models of the heart have helped understanding complex electrical interactions, disorders and pathologies at different levels [47, 78, 82, 110, 170, 178]. The accuracy and usability of those models depends mostly on their capacity to represent heart anatomy, microstructure and function. However, integrating such a variety of biological data for a given patient is often not possible mainly due to technical limitations, e.g. acquisition of microscopic structural information. Therefore, the natural solution to obtain patient-specific models is to combine patient-specific data, and knowledge-domain data. This can be obtained from ex-vivo studies or invasive imaging techniques on a certain population. The CCS cannot be personalized from in-vivo images because the size of its structures is in the order of cellular resolution, and current clinical imaging systems cannot differentiate them from the rest of the myocardium. Recognizing its importance, modelers have attempted to incorporate the CCS function in ventricular models using different approaches. Techniques to include the CCS are often based on i) functional approximations that emulate the fast endocardial activation [43]; ii) simplified tree-like representations based on mathematical models such as fractals or manual delineations [1, 71, 80, 141]; iii) detection of PMJ locations from electrical recordings [19, 123]; and iv) invasive data collected from animal studies such as rat, rabbit or dog, where the main features of the structure are captured [27, 28, 119, 175]. Moreover, a number of computational studies have already integrated CCS models to analyze its role in non-physiological scenarios such as defibrillation shocks [31, 52], drug-modeling interaction [59] or rare polymorphic arrhythmias [15]. Recently, Cherry et al. [42] segmented a Purkinje network from photograph of a stained dog heart, and deployed it in a 2D mesh to study the role of the CCS during ventricular tachy-arrhythmias. All these studies reproduce Purkinje cell electrophysiology by means of tailored action potential models [12, 161] that capture their main behavior.

In this study, we first review anatomical quantitative descriptions available in the literature about the morphology of the peripheral CCS as observed at macroscopic resolu-

tion [5, 8, 49, 107, 147, 167]. Then, we analyze photographs from ex-vivo calf and lamb hearts stained with Indian ink, and present a procedure to extract quantitative macroscopic information about the branching pattern of the stained CCS. These measurements parameterize an automatic algorithm that constructs a computational 3D model of the CCS, given a ventricular anatomy [150]. Following, we run a sensitivity analysis on fundamental parameters of the growing algorithm and study how they affect the final density and distribution of PMJs, as well as the electrical activation sequence. Finally, we compare our approach with current modeling techniques and discuss limitations.

4.2 Materials and methods

4.2.1 Data acquisition

Ex-vivo calf and lamb hearts were stained in order to differentiate the CCS, and to extract quantitative parameters about their macroscopic structure. The procedures were according to those described by previous researchers (see Table 4.1. Five calf (weights ranging 600 to 670 kg) and five lamb hearts (weights ranging 65 to 75 Kg) were obtained from the slaughterhouse after the animal died, and were instantly immersed in a solution of Krebs-Henseleit at 4°C (118 mM NaCl, 4.75 mM KCl, 25 mM NaHCO₃, 1.2 mM MgSO₄, 1.25 mM CaCl₂, 1.2 mM KH₂PO₄, 11 mM glucose). Subsequently, two incisions were made, one at the right ventricle, on the right side anterior inter-ventricular sulcus and another at the obtuse edge of the left ventricle (LV), thereby exposing (as a book) the endocardial surface of both ventricles. An insulin syringe and needle were used to inject black Indian ink, between the endocardium and the sub-endocardial connective tissue sheath, at the origin of the left and right branches of the HB. Indian ink diffused first through the sub-endocardial Purkinje network and then in the intra-myocardial direction to the epicardium. Later, the injected hearts were fixed and stored in buffered formalin at 7%. Additionally, 6 high-resolution histological samples from right or left ventricle containing the peripheral CCS were acquired and serially sectioned at 7-10 μ m. One of every 10 histological sections was stained by Masson's trichrome or Goldner trichrome. Photographs were taken using a stereo microscope equipped with a digital camera (Nikon SM 1500). The resolution of the histological images was 300 pixels/inch, width: 2560 pixels, height 1920 pixels. The software of the microscope was used to perform different measurements. The tissue handling for the paper was in accordance to the European Directive for the Protection of Vertebrate Animals used for experimental and other purposes (86/609/EU).

4.2.2 Image segmentation

An automatic segmentation pipeline was designed to extract the His-Purkinje system structure from photographs where CCS had been stained with Indian ink. Color-based

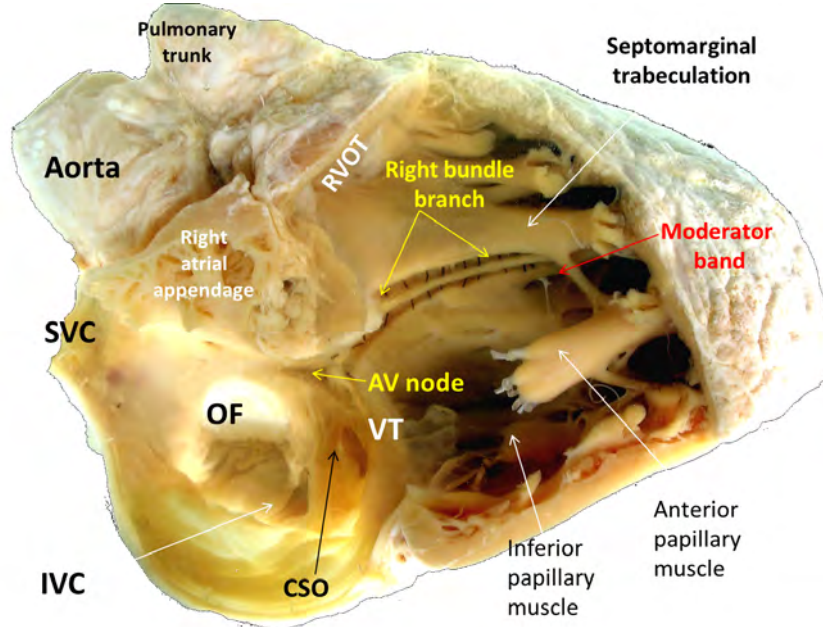


Figure 4.1: Photograph of calf heart showing the Purkinje network. Open calf heart with stained Purkinje network using Indian ink. Overlapped red color highlights the proximal HB and BB, whereas blue color highlights the distal Purkinje network. Sub-figure in the upper-left corner shows a histological sample of the LBB acquired with higher magnification and marked with Goldner trichrome. Fibers are arranged longitudinally under the endocardium in the septum. Sub-figure in the lower-right corner shows a zoom to the network system where the Purkinje pattern can be observed.

segmentation was the technique chosen to segment the black stained fibers from the myocardium (see Figure 4.2b). First, images were converted to the CIELAB (CIE 1976 L^*a^*b) color space [144]. CIELAB creates a more perceptually uniform color space, which helps in the pixel color-based classification. Then, reference tissue colors of Purkinje and myocardium were manually chosen for each histology sample. All pixels of each image were classified using a nearest neighbor color rule algorithm to the previously selected reference samples. Following, images were binarized with the threshold (see Figure 4.2c) that better split classified pixels. In some cases there was small noise in the images due to lack of diffusion of the ink. These were corrected by using mathematical morphology operators, in particular an *opening* with a circle of 2 pixel radius. In some complex cases, binary images were manually edited to remove persistent noise. Finally, a standard skeletonization function was applied to the binary images to obtain the branch centers.

In order to extract quantitative measurements, branching points were determined, and each branch was separated and labeled. The length of each branch was extracted by counting the number of pixels. In addition, all branches meeting at a particular branching point

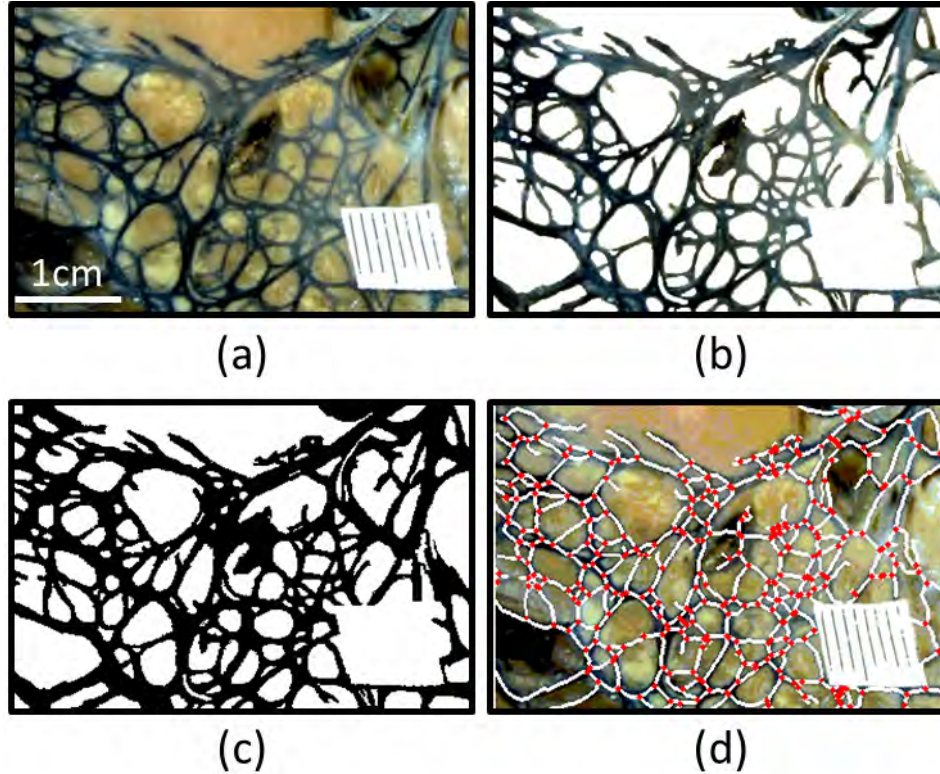


Figure 4.2: Purkinje segmentation steps. (a) Sample of original stained image of a calf LV. (b) PK fibers segmented using CIELAB (CIE 1976 $L^*a^*b^*$) color-based segmentation. (c) Threshold binary image. (d) PK fibers skeleton and branching points on top of original stained image.

were classified to measure the angles formed by every pair of branches. Finally, the curvature of each individual branch was calculated measuring and averaging the angles between consecutive blocks of three pixels belonging to the same branch. We required at least three consecutive angle measurements to characterize curvature for a given branch. Therefore, only branches of at least 8 pixels were considered. The circular statistics toolbox from Matlab CircStat [21] was employed to compute histograms, average and standard deviation of angles.

4.2.3 The cardiac conduction system model: ventricular anatomy

A segmented human ventricular model at the end diastolic phase was used as a layout for the generation of the CCS. This model had been previously segmented [150] from a multi-slice computed tomography (MSCT). Several anatomical landmarks including the endocardial apex, the approximate position of papillary muscles, the septal region, and the

starting point of the HB, were added. The Purkinje generation algorithm needs to identify anatomical regions to apply proper constrictions in several rules.

4.2.4 The cardiac conduction system model: description of the method

The methodology used to generate the CCS models is an extension of the one recently presented in [150]. The method is designed to produce the models in three consecutive stages that correspond to His and bundle branches, backbone branches (PKBB), and terminal branches (PKTB). Figures 4.3b-4.3d show the three consecutive stages for a Purkinje tree generation. The extended method can be personalized independently at each stage with the information extracted from ex-vivo images. In the first stage (Figure 4.3b), three main long branches are generated. They represent the HB and BBs. The first of them starts at the AV node and expands towards the LV apex and back to the base, bounded by a maximum length parameter. The other two branches start out of the first one in the upper third of the septal wall. They are initially directed towards landmarks included in the LV model that are placed close to the area of the papillary muscle insertions. After approaching the landmarks, they turn in the direction of the basal region. Setting a number of additional sub-branches that interconnect the first three branches completes the first stage. All branches in this stage are generated sequentially, with their length constrained by the length of the LV long-axis. Branches are composed of several small segments that allow adjusting them to the ventricular model surface, obtaining a more realistic branch curvature. The main parameters that define the first stage are branch length, angles between consecutive segments (to define the curvatures), length of the segments, starting angle of new branches (angle between the first segment of a 'child' branch and the 'parent' branch), starting position of new branches, approaching distance to the landmarks and to previous branches, and number of branches. Most of the parameters are mean values for statistical distributions that allow the generation of different and independent CCS models. For the present paper, parameters were chosen according to the morphological properties of the CCS proximal regions (BB and PKBB) learned from our observations in photographs of calf hearts. They are basically the number, the length, the angle and the end-points of the BB.

The second and third stages are based on concepts of Lindenmayer systems (L-system) [80, 94]. They use a set of rules or productions, similar to those used in formal grammars, which are applied to build the branches. The closest L-system form to our method is the stochastic bracketed context-sensitive L-system [127]. Both stages are generated using basically the same algorithm, but personalized with different parameters. The selection of different parameters for each stage leads to an improved branch space-filling, and to a point a better self-avoiding control. The algorithm starts selecting the initial points for new branches from the tree generated in previous stage. Following, new branches are iteratively generated, starting from the endpoints of the previous iteration. The order in which the endpoints are selected to grow the new branches is randomly chosen at each iteration. In each iteration two new branches grow at every endpoint. They can follow an

‘L’ growing rule that leads to tree-like monopodial configurations (child branch that keeps the direction of the parent branch), or a ‘Y’ growing rule that leads to tree like sympodial configurations [188]. In the models generated for the present work, branches in the PKBB stage grow following a ‘Y’ rule, while branches in the PKTB stage follow a more directional ‘L’ rule. The basic parameters are the branch length $\lambda \pm \sigma_\lambda$ and the angle between branches $\alpha \pm \sigma_\alpha$ (see Figure 4.3a for a visual description of other relevant parameters $\{\alpha, \lambda, \beta, \gamma, \omega, \kappa\}$). The small segments that form the branches permit the generation of curved structures controlled by the parameters μ , γ and β . This gives rise to more realistic morphologies and allows a better expansion of branches over the ventricular walls. In addition, a distance gradient similar to the one considered in [80], affects the branch angles to avoid collisions between branches. However, when it is not possible to avoid a collision, the branch can either end in a PMJ, or it can form a loop. This is defined by a probability that depends on the distance to the closest branch, and an additional parameter that can be personalized. In general, for the PKTB stage the parameter is set to avoid loops, but in any case PMJs are not allowed in proximal regions.

For the second stage (PKBB), parameters were set based on knowledge-domain data extracted from histological images together with our own data when it was available (see Figures 4.3c, and Figure 4.5). In the case of the third stage (PKTB) there is little information on the Purkinje network topology at high resolution, since it is at least one order of magnitude smaller than PKBB. Details about PMJ density and location could not be obtained from our images. However, images taken with a micro-tomograph and Goldner trichrome stain [114, 147], show that branches seem to form more elongated structures instead of polygonal ones. These images were only visually inspected.

The code to build the CCS was written in C++ using the VTK 5.2.1 (The Visualization Toolkit) library, and integrated in the Purkinje plug-in for GIMIAS [92], which is available under request along with one of our CCS models and its corresponding LV geometry in VTK format. As supplementary material we provide the parameters used to build the model, and the resulting PMJ density.

4.2.5 Electrophysiology simulations

Biophysical simulations of cardiac electrophysiology were carried out to test different CCS configurations. For these simulations, the segmented ventricular surface mesh was remeshed with tetrahedron to generate a volumetric model. The distance between mesh nodes was bounded to $350\mu\text{m}$, giving rise to a mesh of 8 million linear elements. Tetgen software [156] was used for remeshing.

Fiber orientation of the tissue was calculated at every element by applying a rule-based method based on the histological studies of Streeter [163] and validated by Jouk *et al.* [83].

All the electrophysiology simulations were performed with the CHASTE solver [118], which uses a finite element method to solve the electrical equations at cell and tissue resolutions. The ten Tusscher *et al.* [174] model was chosen to solve the ion kinetics.

Table 4.1: *Relevant data on the CCS*

| Section | Ink/Stain | Branch Length | Species | Ref |
|---------|-------------------|---------------------------------|-------------|-----------|
| AV-node | Dissection | 5-7 mm | Human | [85, 185] |
| BB | Lugol | - | Canine | [107] |
| | Gieson | 18 mm | Canine | [167] |
| | Goldner trichrome | 30-40 mm | Human | [100] |
| PKBB | Anti-connexin43 | 12 mm (intramurally) | Bovine | [114] |
| | Goldner trichrome | | Sheep/Human | [147] |
| | MRI | Free-running 13 – 79mm | Rat | [28] |
| PKTB | ATCHI | 100 μ m | Rat | [74] |
| | | 180 μ m | Human | [80] |
| | Goldner trichrome | 25 – 200 μ m | Sheep/Human | [147] |
| | Lugol | PMJ | Rabbit | [40] |
| | SEM | | Sheep | [155] |
| | - | Transitional 100 – 1000 μ m | Rabbit | [169] |
| | MRI | 448 \pm 92 μ m | Rat | [28] |

SEM: Scanning electron microscopy

For the propagation of the electrical impulse in the cardiac tissue, the monodomain formulation was used [121, 125]. The values for the conductivities were set according to those measured by Clerc [48]. Since a monodomain approach was used, intracellular and extracellular conductivities were combined as described in [24]. The ODEs from ionic models were solved with the backward Euler method with a time step of 10 μ s. In the Purkinje strands, propagation was modeled as a wave traveling at a constant speed of 3 m/s. The Dijkstra algorithm was used to measure the distances from the AV-node to each PMJ through the CCS network. This approach is limited to test activation sequences under physiological healthy conditions. The CCS network was considered isolated from the rest of the ventricular tissue except at the PMJs. Each PMJ was connected to its surrounding tissue and generated an intra-cellular current that triggered the activation of its surrounding ventricular nodes within an area of 1 mm³. Simulations were run for 150 ms to reach the full depolarization of the LV in all cases.

4.3 Results

4.3.1 Anatomical measurements on the cardiac conduction system

To analyze the peripheral CCS we virtually divided the network in three parts from proximal to distal sections, according to the three stages of the CCS construction method. First, the His and bundle branches (HB and BB); second, the major backbone branches

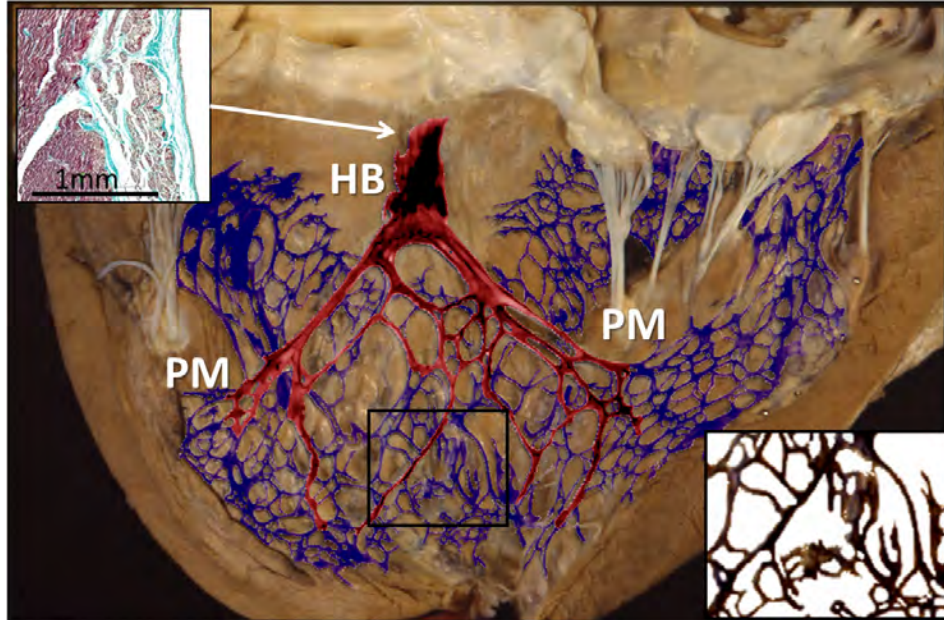


Figure 4.3: Branch growing. (a) Shows the most important parameters used to control the morphology of the CCS branches. The consecutive stages followed by the algorithm to generate the CCS are: (b) the Bundle branches, (c) the PKBB, and (d) the PKTB.

(PKBB, often called free-running PK); and third, the terminal branches (PKTB). The last section is constructed by structures that require microscopy techniques to visualize them, although the resolution limit with previous sections was not strictly defined. Big strands of the CCS can be clearly differentiated in extensive sections of LV and RV endocardium without any magnification, revealing the macroscopic morphology of the system (see Figure 4.1). The distribution of Purkinje system in calf and lamb is structurally very similar because both have a sheet of connective tissue that individualizes the Purkinje system from the endocardium or the working myocardium.

In Figure 4.4a, only thick LV branches were considered in the segmentation to obtain the main branching pattern, whereas Figure 4.4b took into account the detailed branching pattern. At both resolutions a polygonal pattern is clearly present as an extensive sub-endocardial network [8], also described previously as a fishing-net using electron microscopy [155].

The PK network extends throughout the ventricles covering most of the walls. Using mathematical morphology operators we obtained the center line of the branches of the CCS and the joint points, displayed as white lines for branches and red dots at joints (see Figure 4.4). This segmentation allowed us to measure branch length more accurately. The branch lengths segmented were fit to an exponential distribution for each ventricle. Data was consistent in both ventricles, with average lengths of 3.6 mm for main branches in both cases. When small branches were included average lengths of 1.0 mm for LV and

1.4 mm for RV were obtained. These values are also consistent with measurements reported in [80], with an average branch length of 1.8 mm (10 times the measured at high resolution, 0.18 mm).

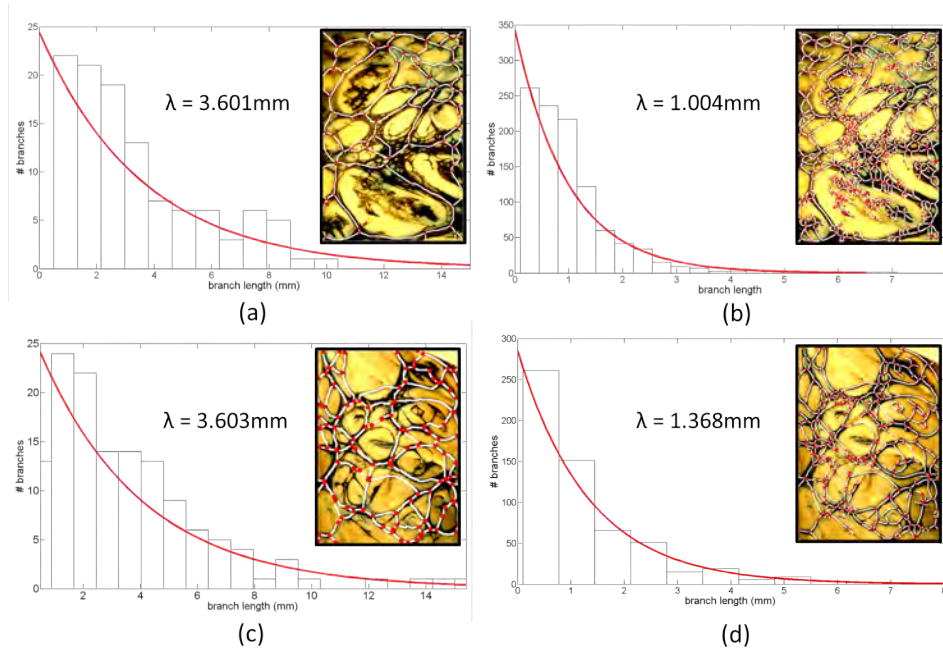


Figure 4.4: Histograms of branch length for LV and RV. Segmentation of Purkinje branches from LV and RV patches and histograms of branch length distribution. (a) and (c) show the branch segmentation and distribution considering only major PK strands for LV and RV, respectively. (b) and (d) include all the small branches and furcations. An exponential function was fit to each distribution. Average length for major LV branches was $\lambda = 3.601 \pm 2.2\text{mm}$, whereas for all LV branches was $\lambda = 1.004 \pm 0.8\text{mm}$. Average length for RV major branches was $\lambda = 3.603 \pm 2.8\text{mm}$ and for all RV branches $\lambda = 1.368 \pm 1.0\text{mm}$.

For the inspection of the branch angles, we used the segmented PK skeletons. For each junction point (red dots in Figure 4.5 and Figure 4.5a), we calculated the small angle between each pair of branches. The resulting average for the four best stained tissue samples was $60.0 \pm 40^\circ$, which shows a large dispersion probably due to the existence of two angle populations (90° and 45°), as it can be inferred from Figure 4.5b). No significant differences were obtained between samples. Angles between parent and child branches (α_1 angle in Figure 4.5b) show a large variance. There was a maximum in the density function around 90° , which means that child branches deviate approximately $45^\circ - 60^\circ$ in opposite angles with respect to the parent direction. Angles larger than 90° correspond in general to α_2 and α_3 in Figure 4.5b. We also find large angles between parent-child branches for those cases in which the branch direction is kept, therefore forming angles

of around $140^\circ - 180^\circ$. Branch curvature was small, with angles around $15^\circ - 20^\circ$ in average (Figure 4.5d). Only branches larger than 8 pixels were used to measure the curvature. The main reason was that at least two groups of 3 pixels were required to measure the angles along a branch, and at least two angles per branch were considered for the curvature. The mean maximum deviation angle (Figure 4.5c) was $33 \pm 40^\circ$. Note that the pixel discretization of the space affects the angles measured.

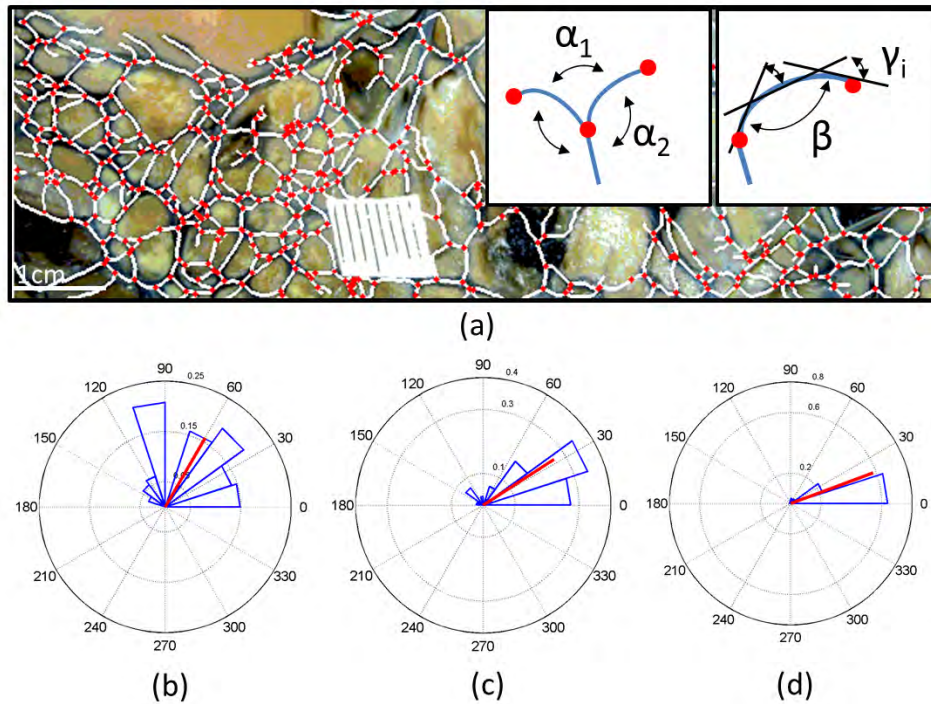


Figure 4.5: Histograms of branch angles and curvature for LV tissue patch. (a) Skeleton obtained from the segmentation of an endocardial LV patch. The small subplots show the meaning of angles α , β and γ . (b), (c) and (d) histograms of angles between consecutive branches (α), maximum deviation angle (β) and branch curvature (γ), respectively.

Visual inspection of high-resolution images revealed a fine structure that showed a clearly directional pattern (data not shown). Those images showed a high complexity in their patterns and were not segmented. No quantitative information was obtained for branches below a millimeter resolution.

4.3.2 Analysis of model structure

A series of simulation experiments were performed to study the properties of the automatically generated CCS networks. The aim was first, to obtain a structure that resembled qualitatively CCS networks observed in anatomical studies. Second, to obtain a consistent

Table 4.2: Relevant parameters measured for PKBB and used to build the CCS models

| Parameter | PKBB | PKTB |
|---|--------------------------|------------------------|
| Rule | Y | L |
| Branch length ($l_b \pm \sigma_l$) | $[3.0, 10.0] \pm 0.3$ mm | $[0.3, 8]$ mm |
| Branch angle ($\alpha \pm \sigma_\alpha$) | $60 \pm 40^\circ$ | $[15^\circ, 90^\circ]$ |
| Curvature ($\gamma \pm \sigma_\gamma$) | $17 \pm 40^\circ$ | 5° |
| Max. curvature ($\beta \pm \sigma_\beta$) | $33 \pm 40^\circ$ | 10° |
| Segment number | 10 | 10 |
| Max. branches | 300 | $[8, 2048]$ |
| Buds | 30 | $[4, 1024]$ |

activation sequence and timing for the electrical activation of the ventricle. Since it was not possible to personalize the most distal section of the CCS (PKTB) due to the lack of quantitative data, a sensitivity analysis was carried out.

The CCS construction algorithm was personalized with the parameters extracted from histology for the PKBB, as displayed in table 4.2. The main branches of the trees generated fairly reproduce the intricate architecture observed in histological and morphological studies [8, 147] (see Figure 4.4 and Figure 4.6a-4.6b). As it can be observed, the HB is directed to the apex, and branches out towards both papillary muscles (see black arrows) around the upper third of the septal wall. The upper areas of the septum and the base do not show any branch or terminal. Similar to CCS visualized in animals using dyes, our networks form polygonal patterns that extend over most of the endocardial surface. The PKTB depend on the previously generated PKBB, as it can be observed in Figure 4.6c-4.6e. However, if PKBB is not dense enough, as displayed in Figure 4.6e, PKTB have to cover large areas, which produce more PMJs locally, unbalancing the tree. Figures 4.6c and 4.6d show a zoom to the lateral wall of a balanced PKBB model in which Y-rule and L-rule were used for the generation of terminal branches, respectively. L-rule shows better results in covering the empty regions left by the backbone branches along the main backbone branch directions, which resembles to images showed by Ryu *et al.* [147] where elongated directional branches are displayed.

The densities and distribution of PKTB and PMJs are important unknown parameters. They depend on the local branch number, branch length and branch angle (since this might influence the number of loops). Therefore, we generated CCS models with an increasing number of branches to compare the distribution of PMJs as a function of the branch density. The proportion and mean distance between PMJs were studied regionally (see Figure 4.7a) and no differences were observed. The PMJ distribution pattern (see Figure 4.7) was very stable as the branch density was increased, and was independent of the rule used for growing the PKTB. Trees always showed few terminals in basal areas, and the upper third of the septum, as a result of the hard-coded rules (non user-defined) included. Lateral and

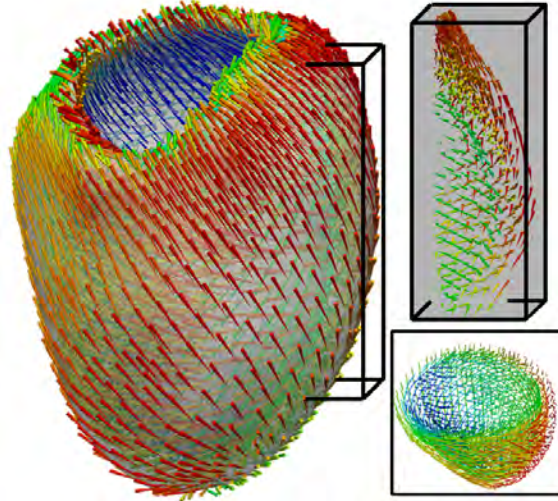


Figure 4.6: Branch distribution. (a) and (b) show the CCS branch structure generated for the apical and lateral walls, respectively. (c)- (e) show trees generated with different rules and number of parent-child buds for the PKBB-PKTB (200-Y, 200-L, 20-L), respectively. (f) shows the locations of PMJs for trees generated using L-rule (green spheres) and Y-rule (blue spheres) for PKTB with the same remaining parameters.

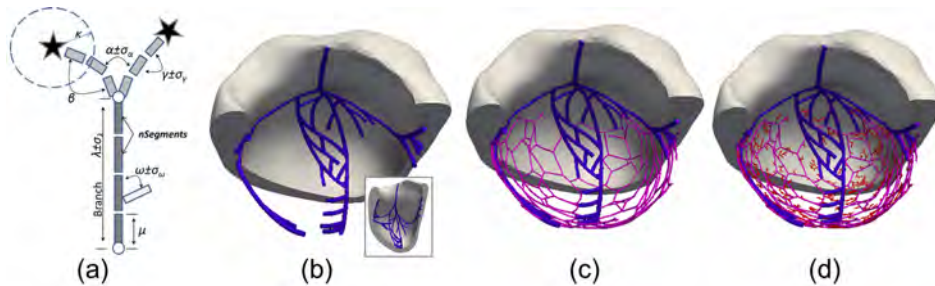


Figure 4.7: Distribution of PMJs per AHA segment. (a) shows a division of the ventricles in 17 regions. In our model segment 17 did not include endocardial tissue. (b) shows the average percentage of PMJ and (c) the average distance between PMJs, per region. Data was averaged for the 9 CCS configurations with increasing branch density using for the terminal branches the Y-rule (solid line) and the L-rule (dashed line).

apical walls were the areas that exhibit a higher number of PMJs in all the CCS trees.

Finally, to study in detail how the number of PMJs was affected by the branch length (λ) and branch angle (α) in the PKTB, we used a fix CCS model for the PKBB with several configurations for the PKTB. In particular, we increased the number of PKTB branches from 8 to 2048, the branch length from 0.3 mm to 8 mm, and the angle from 15° to 90° . Figure 4.8 shows that for large branches, longer than 4 mm, the algorithm cannot build enough branches and the number of PMJs decreases. The reason is that PKTB grow

in the spaces left by the PKBB and therefore affects directly the number of new branches that can be fit. A recommended configuration for PKTB branch is to use a length ten times shorter than PKBB. For the angles there were no significant differences, which was unexpected. The algorithm managed to find the right areas to grow and avoid surrounding branches. For each PKTB configuration, ten CCS models were built with exactly the same parameters in order to analyze whether the use of statistical distributions affected significantly the resulting trees. All the standard deviations obtained were small, in the order of 5% (not included in the figure because they were not appreciable).

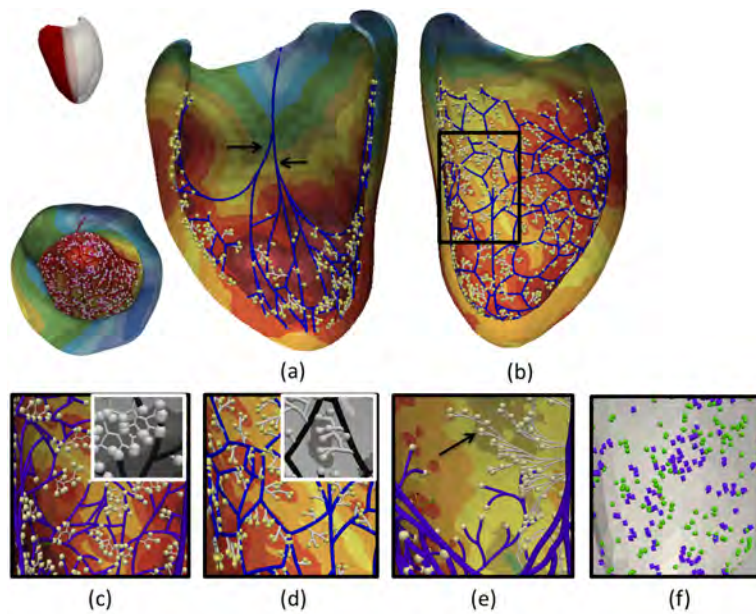


Figure 4.8: Sensitivity analysis of PMJ density. Number of terminals obtained as a function of the branch number for different (a) branch lengths [0.3, 8]mm and a fix branch angle of 60° and (b) branch angles [15, 90] degrees and a fix branch length of 1mm.

4.3.3 Activation sequences

We performed a sensitivity analysis to study how increasing the number of PKTB, which has a direct impact on the number of PMJs, affected the activation time and the branch density per region (see Table 4.3). For each of the CCS configurations, we ran an electrophysiology simulation and measured the total activation times (TAT) for both the endocardium (with 90% and 100% of tissue activated) and the whole LV. TAT was obtained as the difference between the first endocardial node activated and the last one of the model.

Table 4.3 displays the obtained TAT for each number of PMJs on the endocardium and whole LV. When compared to measurements obtained by Durrer (70.1 ± 7.2 ms) [58], TATs show good agreement for models with a minimum of 50 PMJs. An increase in PMJ

density decreased the TAT for the endocardium but keeping the TAT of the full ventricular mass constant.

The analysis of local activation times (LAT) shows that the activation sequence started in apical, anterior and posterior regions, and in some configurations close to basal area (see Figure 4.9). When the model included enough terminals, more than 200, the sequence followed an endocardium to epicardium pattern, with the base of the lateral wall as the last region being activated. These observations are coherent with measurements in real hearts [58]. The missing contribution of the RV in the septum was appreciable and increased the activation time of the septum. For each configuration, we also analyzed the percentage of tissue activated over time, which is a much more reliable index than the TAT. It takes into account the evolution of the activation over time instead of considering only the endpoint (see Figure 4.10).

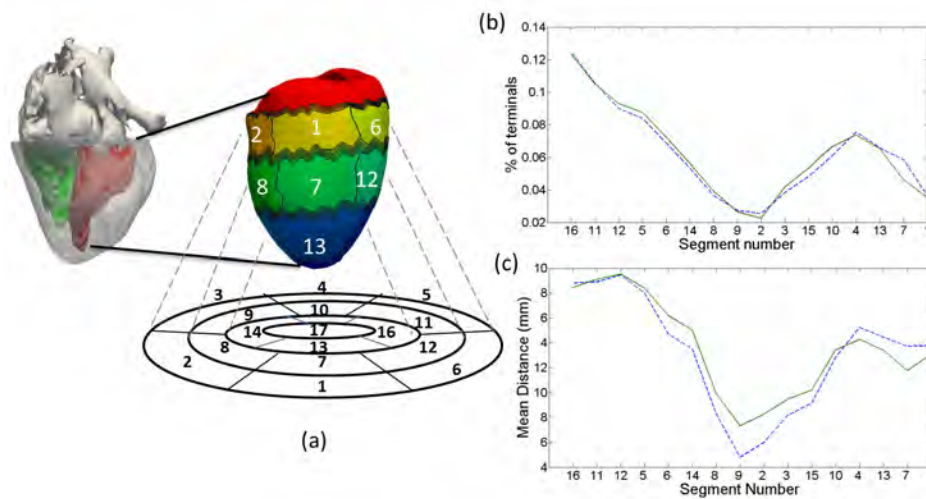


Figure 4.9: *Simulated sequence of activation. Local activation times for a LV model that includes a CCS system with 162 PMJs.*

Table 4.3: *Total activation times (ms).*

| Region | 8 | 25 | 35 | 49 | 94 | 162 | 246 | 312 | 429 |
|--------|-----|----|----|----|----|-----|-----|-----|-----|
| E90 | 64 | 61 | 60 | 64 | 60 | 54 | 54 | 48 | 48 |
| E100 | 130 | 80 | 68 | 71 | 71 | 74 | 68 | 63 | 64 |
| A | 130 | 80 | 73 | 74 | 74 | 76 | 76 | 73 | 74 |

Exx: xx Percentage of endocardium; A: Complete LV

Although TATs for the whole ventricle are very similar, the local activation pattern over time shows a large dependence on the number of PMJs. As expected, the larger the number of PMJs the faster the tissue is activated over the first 40 ms after the initial

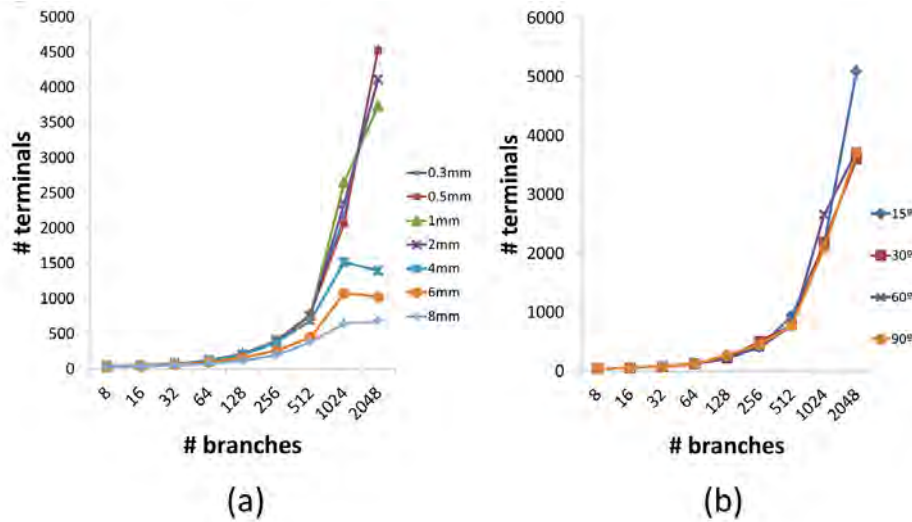


Figure 4.10: Percentage of tissue activated over time as a function of PMJ number.

endocardial breakthrough. This difference smooths out after most of the tissue has been activated, since all the initial wavefront initiated in the endocardium meet together into a single depolarization wavefront. Figure 4.10 shows the percentage of tissue activated over time for different number of PMJs, where configurations with a larger number of PMJs show a faster depolarization between 15 ms and 45 ms.

4.4 Discussion

Early CCS models have traditionally tried to reproduce the sequence of electrical activation of the ventricles neglecting the real morphology of the peripheral CCS, i.e. its branching pattern. Those models were built mostly manually and only for a given ventricular geometry. In general, the main bundles were located in the models following anatomical descriptions from stained tissues from animal hearts [8, 107, 167, 169]. In the human heart three major thick branches with several functional interconnections are usually observed in the LBB [167], although morphological variations are known to exist between subjects [51]. In most species, the LBB divides into anterior and posterior branches, that reach both papillary muscles, and extend towards the apex forming a superficial sub-endocardial network [148]. These findings are in agreement with our observations in the CCS of calf hearts (and Figure 4.1). The length of the BB varies among species, and it is in the order of 30-40 mm for the human [100] (see table 4.1). However, it is not fully clear what the difference is between species in proximal sections [100]. In a previous study [59] it was found that simpler His bundle branching morphologies produced more realistic pseudo-ECGs signals in precordial V1-V6 leads.

In most studies, the distal section of CCS models do not mimic the intricate branching pattern exhibit in histological samples due to its complexity. A common simplification in CCS modeling is to set a number of early activated sites scattered over the endocardial surface [88], often based on data from electrophysiology maps [58]. Others modify the physiological diffusion properties in the endocardium to obtain faster propagation velocities and compensate for the lack of CCS [44, 133]. Those approaches are effective in reproducing activation sequences with realistic activation times, and recently showed their potential to personalize Eikonal-based conductivity parameters to predict cardiac resynchronization therapy on LBBB patients [133] or the induction of ventricular tachycardia on ischemic patients [132]. On the other hand, an explicit CCS structure is still required to model retrograde activation [89, 126] and Purkinje-tissue macro-reentries. More sophisticated models made use of fractals to build a CCS [1, 71] as a structure of repeatedly bifurcating branches. These models did not show the CCS looping structure or more complex branching patterns observed in histological studies. Pollard and Barr [123] presented a model of the human conduction system based on electrophysiological data. The model did not show a high correlation with experiments, probably due to the little coupling and the scattered and low number of PMJ used. Berenfeld and Jalife [19] proposed a His-Purkinje model that included PMJs, based on the procedure of [123], to study Purkinje-muscle reentries.

More recently, CCS models are trying to build the system using so-called knowledge-domain data, i.e., *ex-vivo* histological and electrophysiology data from human cadavers or animal studies. Simelius *et al.* [157] delineated a Purkinje model for human ventricle by minimizing the difference between simulated isochrones and measurements by Durrer [58]. Similarly, Ten Tusscher and Panfilov [173] delineated a peripheral conduction system using a similar structure, and followed descriptions available in the literature to place the main bundles. Using stains a typical branch length can be extracted by visual inspection from the larger branches to improve the realism of the models. Atkinson *et al.* [13] built a 3D anatomical computer model of the His-Purkinje network of the rabbit heart after staining the network by immunoenzyme labeling of a marker protein, and fitting it to a 3D ellipsoid model. Vigmond *et al.* have also presented several studies on a delineated rabbit Purkinje system to study the effect of defibrillation shocks [31, 52, 53, 179]. They use this model to perform electrophysiology simulations, which could reproduce the main expected activation pattern. Vadakkumpadan *et al.* [175] built a 3D anatomical model of the rabbit ventricles in which only segmented free-running Purkinje strands were included, with a total of 71 PMJ in the RV and 99 PMJs in the LV. An extension including more distal Purkinje sections modeled by a parameterized L-system was recently presented and validated by Bordas *et al.* [27]. Their approach is similar to ours [188] since they also use L-systems, although the model we present in this work can be further personalized and adapted if anatomical data is available. They choose to use branches of 4 mm that were fit to the nodes of the underlying endocardial mesh, which is very similar to our measurements of PKBB, 3.6mm in calf. Our methodology is fully automatic and independent of the underlying mesh resolution, since CCS model and ventricle do not share

their nodes, but only at PMJs. Automatic methods help in reproducibility and enable the modeler to study a large number of CCS systems in a faster way, avoiding long time in delineation.

It is important to point out that it has been reported that the branching pattern of the CCS in the RV shows some morphological differences with respect to the LV one[8], which would require different methods to build LV and RV models. We did not observe differences in the branching angle, although branch length was 30% larger in the RV than the LV when all the small furcation were considered. Still, CCS ramifies throughout the RV from the base of the papillary muscles as in the LV. It is not yet clear if more complex Purkinje networks are required or which applications will benefit from more realistic Purkinje systems.

There is very little information on the density and distribution of PMJ in each region of the endocardium. Some studies suggest that the distribution of sub-endocardial PMJs and their electrical coupling is spatially inhomogeneous, and that the junction regions themselves have variable degrees of electrical coupling [106, 107]. Some detailed electrophysiology studies have shown the continuous coupling between the CCS and the myocardium, suggesting a more dense and complex network with thousands of PMJs [40]. In addition, from histological observations, there are large endocardial areas where PMJs would not be expected due to the lack of PK branches, such as the base of the ventricles and portions of the septum [107, 126]. To our knowledge, there are no 3D maps that describe exhaustively how PMJs are arranged in the ventricles and therefore the only source of information are the electrical activation sequences and depolarization velocities in the endocardium. Our simulations show the direct relationship between the total activation time of the endocardium and the density of PMJs as expected. However, It was remarkable that increasing almost ten times the number of PMJ the TAT decreased only few milliseconds. The reasons were due to i) the variability in the morphology of the CCS tree (sometimes not all the PMJ activated before its surrounding myocardium); and ii) PMJ inhomogeneities, i.e. the basal regions and upper septum did not have any PMJ and were always the last areas to activate. Therefore, some of the PMJs were redundant or can be considered as backup PMJs, which role might be important in retrograde activation. If PKBB had been changed between simulations greater differences would have been obtained.

4.4.1 Limitations

The images taken to analyze the statistical pattern of the Purkinje network were flattened and slightly stretched to show a large endocardial area. Although, medium size patches of each region have been analyzed independently an error in the angle branches could have been introduced. In addition, our data only describes information from calf and lamb, which are presumably different from that in human hearts. However, the methodology can be applied to images of the Purkinje system of any species in which Purkinje strands are visible. Electrical simulations with our CCS networks did not consider a specific ionic

model for the Purkinje cells, but a depolarization with a constant velocity. The lack of a Purkinje ionic model implied that a specific model for the PMJs was not needed in our approach to connect Purkinje and myocardium as the ones developed in [179]. This approach is valid to reproduce ventricular depolarizations with realistic activation times, in which retrograde conduction is not required, or a more complex pathological model. Our ventricular model has an average resolution of $350\mu\text{m}$, although a resolution of $250\mu\text{m}$ is recommended by the authors of the cellular model chosen [174]. This fact can impact in the conduction velocity of the depolarization wavefront in some areas. Finally, our CCS models need to be further validated by means of ECG calculated using the Forward Problem in electrophysiology and endo-cavitary electro-anatomical recordings.

4.5 Conclusions

We have collected and segmented data about Purkinje networks of calf and lamb hearts. A methodology to extract data on branch length and branch angles has been designed which can be applied to similar images. Using measured data we produced CCS models with a branching pattern that resembled those acquired in histological studies at macroscopic level. Although microscopic data on CCS is not observable directly in living organisms, the possibility of generating many CCS configurations at microscopic level may assist in the analysis and better understanding of their physiology. CCS trees built with this automatic approach generated normal electrical activation sequences, by just specifying the main input parameters. Given the importance of the CCS network to simulate realistic cardiac activation sequences and the impossibility of obtaining a patient-specific CCS structure, our stochastic CCS model, which takes into account histological knowledge-domain data, might help to achieve more accurate simulation results. This is especially important to model more complex electrical pathologies. The sensitivity analysis carried out on the density of terminal branches and PMJs showed that there are not significant differences in TAT after increasing their density from 100 PMJs, which is related to the QRS width. Differences in angles between branches in the PKTB did not show significant overall differences in the branch patterns or activation maps. Nonetheless, the local activation pattern shows clear differences locally, which could be reflected on the QRS morphology. Due to the small amount of quantitative data available on the morphology of the CCS system, it is very difficult to quantify properly the accuracy of the model. If more data would be available, the input parameters could be defined regionally, so that local inhomogeneities could be better incorporated.

Analysis of the microstructure of the cardiac conduction system with confocal microscopy imaging

Abstract - This chapter presents a characterization of the cardiac conduction system at microscopic scale. The goal is to characterize the architecture of the distal section of the Purkinje network by differentiating Purkinje cells from surrounding tissue, performing a segmentation of Purkinje fibers at cellular scale, and mathematically describing its morphology and interconnections. Purkinje cells from rabbit hearts were visualized by confocal microscopy using wheat germ agglutinin labelling. A total of 16 3D stacks including labeled Purkinje cells were collected, and semi-automatically segmented. State-of-the-art graph metrics were applied to estimate regional and global features of the Purkinje network complexity. Two types of cell types, tubular and star-like, were characterized from 3D segmentations. The analysis of 3D imaging data confirms the previously suggested presence of two types of Purkinje-myocardium connections, a 2D interconnection sheet and a funnel one, in which the narrow side of a Purkinje fiber connect progressively to muscle fibers. The complex network analysis of interconnected Purkinje cells showed no small-world connectivity or assortativity properties. These results might help building more realistic computational PK systems at high resolution levels including different cell configurations and shapes.

5.1 Introduction

Efficient pump function of the heart requires synchronized activation and contraction of cardiac tissues. Specialized tissues known as the cardiac conduction system (CCS) are responsible for synchronization of mechanical activation by fast distribution of the electrical signals that trigger contraction [73]. In the ventricles, the CCS comprises Purkinje (PK) fibers, which are able to conduct electrical signals up to almost an order of magnitude faster than the working myocardium, thus facilitating the synchronous electrical activation of the whole heart [40, 42]. The CCS includes the heart's primary pacemaker, the sinus node in the right atria, which initiates each beat. Electrical signals are transmitted to the ventricle through the atrio-ventricular (AV) node. A bundle located high in the inter-ventricular septum and beneath the AV node, known as the His bundle, branches into the left and right bundle branches descending sub-endocardially into their corresponding ventricles [6]. These branches spread out forming a complex network referred as to the PK network, which is the distal portion of the CCS, which runs both through the ventricular cavity as free-running Purkinje strands (FRPS) and along the endocardium [107]. Depending on species the PK network is electrically insulated from other surrounding tissue by a sheath of collagen, creating an electrical insulation [114]. Electrical signals are therefore only passed to the working myocardium at terminal points known as Purkinje-myocardial junctions (PMJs) [40, 107, 130]. The coupling between PK cells and working myocytes presents two types of configurations: (i) a funnel connection, with a direct coupling to myocytes and (ii) a sheet interface or resistive barrier, composed of transitional cells (T cells) that serve as an intermediate layer between the PK cells and myocytes [169]. Transitional cells are present at the boundaries of the sinus and atrio-ventricular nodes as they connect to their surrounding tissues [55].

Previous studies about the CCS described qualitatively its structure using 2D imaging techniques based on ink markers [8, 49, 50, 107, 147, 167], light microscopy [169], projection microscopy [114], EGFP imaging [102], and optical Imaging [60]. It has only been in recent years that researchers have extracted 3D information about the macro-structure of the PK network. In some studies only the free-running Purkinje strands (FRPS) were analysed using high-resolution ex-vivo MR system [28, 175], while in others the whole proximal 3D structure was reconstructed or simply visualised [13, 42, 50, 160]. In [151] it was attempted a quantitative macroscopic description of the PK network structure performed on 2D photographs of bovine hearts stained with Chinese ink, where branch lengths and furcation angles were measured.

Ono et al. [113] described two types of PK cells, tubular and polygonal, but did not provide information about their different morphological characteristics. Different techniques have been used to provide quantitative measurements on single cell morphology, e.g. lengths, widths, heights, areas, volumes. Single cell isolation of PK cells has been performed in mouse [176] and dog [154], where 2D measurements were provided. Microscopy studies of PK cell morphology have taken direct measurements of cell dimensions but have used simple ellipsoid models to approximate the 3D characteristics such as

surface areas and volumes [113, 159]. With regards to working myocytes, single cell 3D reconstructions have been obtained with confocal microscopy data [93], therefore being able to compute more accurate measures of cell features. In [93] single working myocytes were segmented in 3D and subsequently, volume, length, width and height were estimated. Volumes were calculated as the sum of voxels contained inside the cell and length/width/height estimates were obtained by fitting a bounding box oriented after applying singular value decomposition on second-order central image moments. In [25] stained cells were projected onto a digitized surface and the length and width measured with a sonic digitizer. Volumes were also obtained from rotation of 2D planes along the long axis and assuming that cells have the shape of irregular cylinders. In [70] and [36] the volume of myocytes was calculated using a Coulter Channelyzer system as well as by multiplying the length by the cross-sectional area (obtained from electron micrographs) of isolated cells, obtaining comparable results. To our knowledge these PK cell measurements had not previously been taken from 3D reconstructions.

An important aspect of the PK network involves the electrical coupling between neighboring cells, which is achieved through gap junction channels. These are channels connecting the cytosol of two cells to allow ion flow. Gap junction channels are made of proteins known as connexins: channels with Cx40 have the largest conductance, Cx43 provides an intermediate conductance, and Cx45 has the lowest conductance in cardiac cells [29]. Although a combination of these proteins and channels is present across different tissues they differ in abundance [55]. The Cx40 is predominantly found in PK fibers, while Cx43 is mainly present in the working myocardium [72, 153, 183]. Commonly, gap junctions are preferentially located at cells' ends (end-to-end connection) to facilitate longitudinal signal propagation among cells while smaller expression is found allowing lateral communication between cells [91, 153].

An improved understanding of the 3D structure of the PK network, and in particular their connection to working myocardial cells, has implications for our knowledge of cardiac diseases [90]. The PK system plays an important role in arrhythmogenesis, for example in macro- and micro-reentries due to unidirectional blockage giving rise to ventricular tachycardia [165]. In radio-frequency ablation therapy for ventricular arrhythmias the targeting of Purkinje-like-potentials (PLPs) at the boundaries of a scar border zone has proven to be an effective method for eliminating the recurrence of ventricular fibrillation [158]. Therefore an increasing number of computational models have incorporated and (in silico) analyzed the CCS in order to understand the underlying pathologies and optimize treatment [27, 79, 142, 173]. Experimental work [186] and modelling studies [18, 129] on the influence of the PK micro-structure on arrhythmogenesis has focused on the coupling and electrical disturbances of the PMJs.

An accurate 3D structural analysis of the distal portion of the CCS can enhance the possibility of developing realistic generational algorithms of the PK system, as it has been already done at macroscopic scale [38, 80, 151]. The goal of this paper is to obtain a set of quantitative measurements of the 3D microstructure of the PK system at its distal portion in order to better characterize its morphology. Firstly, we provide 3D information on cell

dimensions from segmentations of PK fibers obtained from confocal microscopy imaging. Furthermore, we analyze the PK system by modeling it as a 3D graph and then estimating measures of network complexity as well as other measures such as branch lengths and angles at furcations.

5.2 Materials and methods

5.2.1 Tissue preparation

For the microscopic characterization of the PK system, we designed a pipeline to acquire and process tissue samples from rabbit hearts. All animal usage was approved by the Institutional Animal Care and Use Committee (IACUC) at the University of Utah. Adult rabbits were anesthetized with pentobarbital and anti-coagulated with heparin. Following thoracotomy hearts were quickly excised and placed in a modified oxygenated Tyrod's solution at room temperature. The hearts were retrogradely perfused. Tyrode's solution including wheat germ agglutinin (WGA) conjugated to Alexa Fluor 555 (Invitrogen, Carlsbad, CA). Through the hearts, WGA binds to glycocalix of carbohydrates in the cell membrane and extracellular proteins. This method allowed for a homogeneous distribution of the dye throughout the heart. The hearts were subsequently fixed through the same line of the Langendorff perfusion with paraformaldehyde. Biopsies were made from left and right ventricle lateral walls (mid and apical), papillary muscles, and septal wall. Afterwards, the biopsies were stored in paraformaldehyde.

5.2.2 Confocal microscopy imaging

Images were obtained within 2 months after tissue preparation. 3D image stacks were acquired using a confocal microscope equipped with a 40x oil immersion lens (Zeiss 5 Live, Jena, Germany). Image stacks had a spatial resolution of $0.31 \times 0.31 \times 0.31 \mu\text{m}$ and were obtained with a field-of-view (X and Y directions) of $318 \times 318 \mu\text{m}$ extending up to $60 \mu\text{m}$ into the myocardium (Z direction). The Z-axis was parallel to the laser beam direction. An example of a 3D-stack with processed images is illustrated in Figure 5.1 (right panel).

The WGA labelling marked the interstitial space and cell membranes in the samples. For the process of identifying PK cells and working myocytes the tubular system (T-system) was examined. A sparse T-system is present in PK fibers while a dense T-system is a feature of ventricular working myocytes [14].

5.2.3 Geometric reconstruction and structural analysis

Each of the 2D images from the 3D stacks was pre-processed to improve the segmentation step using previously developed methods [93, 140]. Firstly, the iterative Richardson-Lucy deconvolution algorithm was applied to all images using a measured point spread

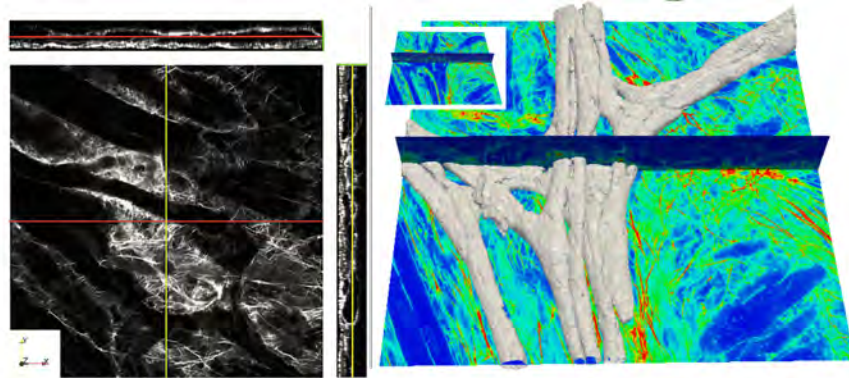


Figure 5.1: *Processed images from 3-D stack of WGA labeled endocardial ventricular tissue from rabbit. Left panel illustrates a sample stack in XY (plane parallel to endocardium) XZ, and YZ views where PK cells show a sparse T-system. Right panel shows the corresponding 3D reconstruction of the cells on a slice of the corresponding stack. The image stack was deconvolved and corrected for depth-dependent attenuation. Field of view: $318 \times 318 \mu\text{m}$.*

function. Secondly, background signals were removed and depth-dependent attenuation corrected. Signal-to-noise ratio (SNR) of each image stack was measured as described previously [91] and the ones with a SNR below 3 were rejected. The PK fibers, i.e. paths of connected PK cells, were manually segmented from the different 3D image stacks. Automatic segmentation techniques were not suitable for the accurate extraction of the PK network trajectories due to the varying levels of diffusion of the WGA in the tissue in different images. Therefore, we manually located landmarks along the PK pathways in all 3D image stacks at furcation points. The 3D Slicer software [117] (www.slicer.org) was used to identify the bifurcation points. Spatial coordinates of the landmarks were stored and were subsequently connected with straight lines, forming the fiber centerlines. Figure 5.1 (right panel) illustrates the 3D reconstruction of several PK strands together. From this 3D segmentation centrelines were obtained and used to quantitatively analyze the PK network morphology (angles of furcations and complexity of network). In-house software developed using Matlab (MathWorks, Natick, MA) was subsequently used to reconstruct the PK pathways. A set of 10 stacks was selected to perform a full 3D segmentation and characterize the different cell shapes. A painting tool available in the software 3D Slicer allowed segmenting in 3D each cell across the stacks. Each cell was represented by a triangular closed surface mesh. The morphology of the reconstructed PK cells was quantitatively characterized (3D lengths, surface, volume) to explore possible different geometrical configurations. For the measurements of length and the diameters in tubular cells, multiple measurements were taken for each single cell and for each of its dimensions, which were subsequently averaged. Following the longitudinal axis of the cells, two perpendicular lengths were obtained, the height and the width of the cell relative to the endocardial plane. In star-like cells, the length was measured using as longitudinal length

the longest trajectory between borders connected to neighbor cells. The area of the cells was calculated summing up the surface of each of the triangles that defined the boundary of the cell mesh. From the 3D surface representation, the volume was obtained using the divergence theorem.

5.2.4 Analysis of complexity of the Purkinje network

PK network characteristics were quantitatively analyzed from the set of previously defined landmarks and centerlines along PK pathways. The parameters used to characterize the PK network were the following; i) branch lengths, considered as the set of connected PK cells without any furcation; ii) angles at furcation points, differentiating between acute (α) and obtuse angles (β). In general, at furcation points, cells are connected to two or more neighboring cells forming branches with a 'Y' shape, which can be characterized by one acute and two obtuse angles. If all branches are arranged in a preferred direction, acute angles will be 0° whereas obtuse angles will be 180° . However, in networks that span widely, acute angles will be larger than 45° and obtuse angles 90° . These parameters were quantified in 3D by extraction from the 3D confocal microscopy imaging stacks, thus preserving the 3D nature of the PK network.

Quantitative measures based on graph theory were applied for characterizing the complex PK networks extracted from each image stack. We considered state-of-the-art graph metrics [17] to estimate regional and global features of the PK network complexity, following the work of Rubinov and Sporns [145]. PK networks were then characterized by a set of connected nodes (i.e. furcation points) and links between these nodes (PK pathways) allowing the analysis of important features such as the shortest path length between two nodes of the network (their average often referred as to characteristic path length). The chosen metrics were then the following: i) the global efficiency (GE), defined as the averaged inverse shortest path length between all nodes of the network; ii) the local efficiency (LE) of a node, computed as the averaged inverse shortest path of all neighbors of the node; iii) and the degree, which refers to the number of neighbors a node has and estimates network infrastructure. Local efficiency, which is a measure of segregation, and global efficiency, which measures integration of the network, are combined to test for 'small-world connectivity', which is normally used to refer to networks with highly segregated modules and high number of inter-modular links (integration), such as in the case of the brain [17]. A small-world connectivity network will then be robust to the malfunctioning/removal of certain nodes connecting modules since it will be possible to find alternative small-distance paths between two given modules of the network. As in Achard and Bullmore [3], we used the following criteria for estimating small-world connectivity: $GE_{latt} < GE < GE_{rand}$ and $LE_{rand} < LE < LE_{latt}$, where *latt* is a lattice (regular) equivalent network and *rand* is a random equivalent network with the same nodal degree distribution and size as the original graph. These relations state that a small-world connectivity network will have a higher integration (links between different modules) than a lattice equivalent network but lower than a random one (based on GE). Furthermore,

it will have more segregated modules than a random equivalent network but less than a lattice one (based on LE).

Additional graph metrics were used to characterize the PK network complexity, including: node betweenness (or node centrality), which is an indicator of a node's centrality in a network, being equal to the number of shortest paths from all vertices to all others that pass through that node; and the assortativity coefficient, which estimates the correlation between the degrees of nodes on two opposite ends of a link and shows the preference for network's nodes to attach to similar degree ones (indirectly measuring the vulnerability of a network to insult, i.e. broken links). For comparison purposes, the node betweenness is represented as a histogram for each network, with the number of shortest paths normalized by the maximum number of possible paths crossing each node of the network.

We refer to Boccaletti et al. [26] for more details about these measures. The Brain Connectivity Toolbox [145] was used to compute graph measures. Weighted global and local efficiencies were estimated by using the inverse distance of the edges of the network.

5.2.5 Statistical analysis

Data were expressed as mean standard deviation (SD) for all the measured lengths and angles. The circular statistics toolbox from Matlab CircStat [21] was employed to compute histograms, average and standard deviation of angles. Wherever appropriate, data were subjected to statistical analysis by one-way analysis of variance (ANOVA). A value of $p < 0.05$ was considered significant. Matlab software (MathWorks, Natick, MA) was used for the statistical analysis.

5.3 Results

5.3.1 Cell identification and morphological analysis

Our results confirm a high T-system density in ventricular myocytes (labeled with V in Figure 5.2 (b)) and almost absence of T-system in PK cells (labeled with P in Figures 5.2 (a)-(c)). This visual identification of the T-system was only possible due to the very high resolution of the acquired WGA-labelled images. Figure 5.2 (a) shows the sparse T-system of the PK cells and their nuclei, in contrast to the regular dotted pattern of T-system in the working myocytes in Figure 5.2 (b). The shape of PK cells varied significantly at furcation points, as compared to the regular tubular shape found in bundles and FRPS (Figures 5.2 (d)-(i)). The PK fibers at the junctions in general were more flattened and irregular, taking two of them to make a junction. We have referred to this type of cell as 'star-like' in this paper. These star-like PK cells, as seen in Figure 5.2 (c), showed a lack of T-system. They are commonly connected to tubular PK cells and share with them a lateral connection. Five tubular and five star-like PK cells were segmented from the available data. Manual segmentation of individual PK cells was followed by its 3D surface reconstruction, in

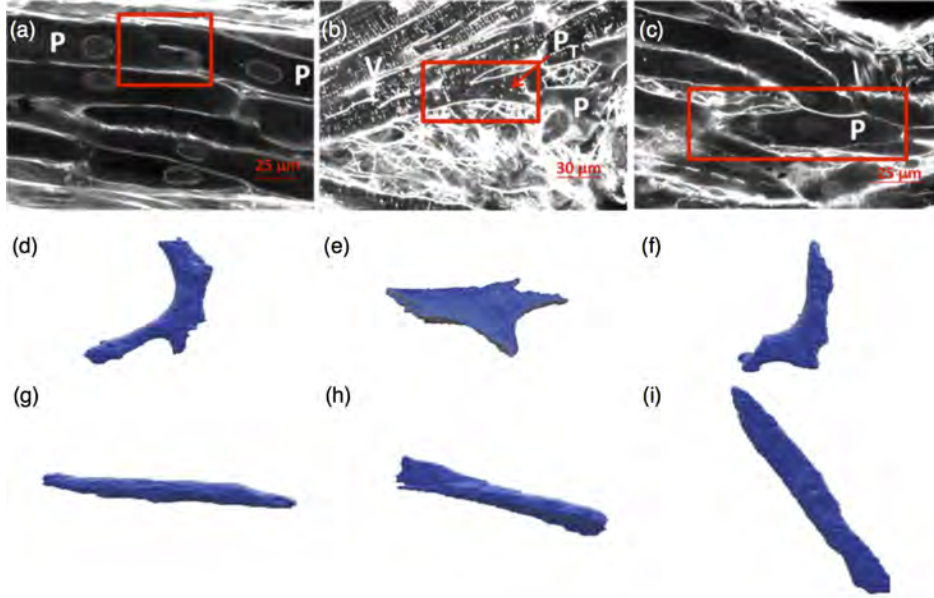


Figure 5.2: Cell identification and shape configurations. Confocal images from Purkinje fibers and myocytes (a)-(c). Tubular (d)-(f) and star-like Purkinje cells (g)-(i). Purkinje labeled as (P), myocytes as (V), transitional cell (P_T).

which we measured length, diameter, volume, surface area, and surface to volume ratio. Figures 5.2 (d)-(i) show three examples of each type of 3D reconstructed cell. Quantitative shape differences between the two types of PK cells are presented in Table 5.1. Although the sample was small, the similarity in volume and surface area between cell groups was remarkable.

Table 5.1: Geometrical measurements on individual PK cells as a function of shape.

| Parameter | Tubular shape | Star-like shape |
|---------------------------------|------------------------|------------------------|
| Length (μm) | 119.76 ± 28.57 | 63.27 ± 6.27 |
| Diameter sagittal (μm) | 13.76 ± 3.60 | 19.70 ± 5.20 |
| Diameter coronal (μm) | N/A | 6.79 ± 1.51 |
| Volume (μm^3) | 15756.32 ± 1573.40 | 15843.62 ± 6979.15 |
| Surface area (μm^2) | 5604.27 ± 107.83 | 5648.84 ± 1892.67 |
| Surface/volume (μm^{-1}) | 0.356 | 0.357 |

N/A: Not available

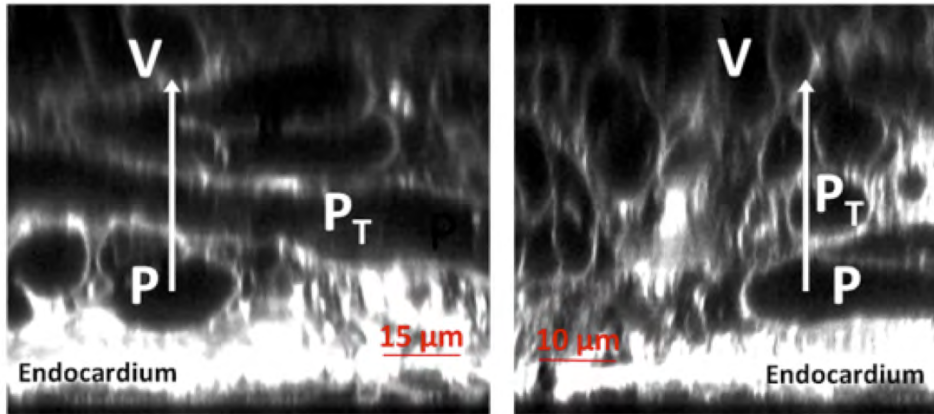


Figure 5.3: Purkinje-ventricle connection. Purkinje labeled as (P), myocytes as (V), transitional cell (P_T).

5.3.2 Cellular connections

Extracellular space was clearly labeled by WGA in the acquired images. Figure 5.2 (a) shows a PK end-to-end connection with a step profile, as highlighted in the figure (red square). The collagen shielding of the PK fibers was only visible in the periphery, therefore we suggest that these cells are longitudinally connected. A PK-myocyte connection is shown inside the red square in Figure 5.2 (b), where a single PK cell end-to-end connects with a ventricular myocyte. Nevertheless, the PK cell shown in this figure had a higher T-system density than regular PK cells (see arrow in Figure 5.2 (b)). The backtrace of the PK strand in the proximal direction placed it at the endocardial insertion of a FRPS.

Visual inspection of longitudinal and cross sectional projections shown in Figure 5.3 suggests the existence of interconnections between PK cells and ventricular myocytes through lateral connections. This assumption is based on the close proximity between cell membranes and the absence of a clear separation in the extracellular labelling. The large white arrows in Figure 5.3 indicate the potential lateral connection of PK to ventricular myocytes. However, this observations cannot confirm whether the connections can transmit electrical impulses. Previous works [114] described a layer of transitional cells (P_T) in between PK fibers and ventricular myocytes. In our imaging data we found cells with different T-system configurations in between PK fibers and ventricular myocytes (Figure 5.2 (b)).

5.3.3 Free-running strands and their connections (network connections)

The study of the FRPS led us to differentiate two types of fiber configurations. In type I all PK fibers inside the strand were in contact in the transversal section and shared the

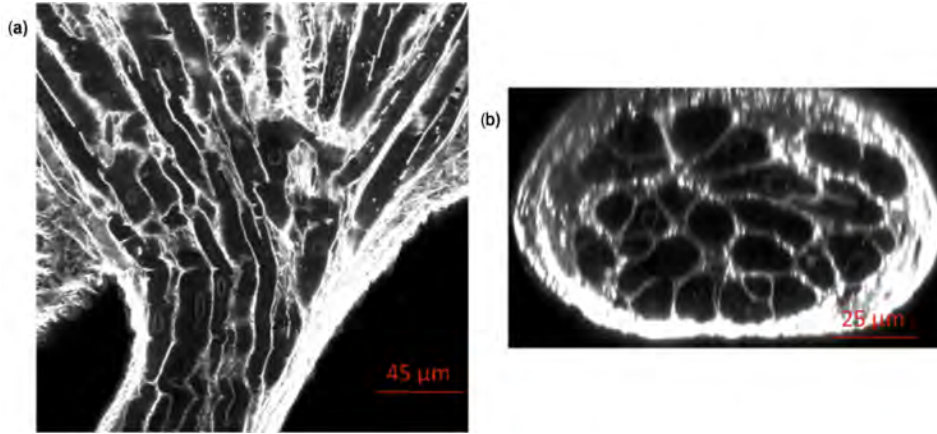


Figure 5.4: Purkinje free running strand type I. (a) Longitudinal and (b) cross-section views.

electrical information through end-to-end connections in the longitudinal direction. As the strand reached the endocardium it spread out as a fan (Figure 5.4). In the second type of FRPS fibers were divided into separate bundles inside the strand, using collagen for insulation. Figure 5.5 (a) and (c) show how bundles inside a strand diverge going on their own separate paths as they approximate to the endocardium. Figure 5.5 (b) and (d) show a case with a smaller strand type II penetrating through the endocardium where its internal bundles create an exchange of information by making a communication network.

5.3.4 Angles and branch length of the network

We extracted conduction pathways from 16 stacks of imaged tissue samples (see example in Figure 5.6 (a)). Figure 5.7 illustrates the results of this segmentation for three representative cases. Branch lengths of the networks were computed as the length between two furcation points and plotted as a histogram in Figure 5.6 (b). The mode in branch length distribution was at around 50 μm, with maximum lengths of about 300 μm. Its average length was of 84.6 μm and median of 65.6 μm. A concentration of short paths, due to several connected star-like cells, highlights the intricate communication among fibers at its microstructure. As expressed above, two angle populations were established based on their acute (α) or obtuse (β) nature at the furcations, as illustrated in Figure 5.6 (a) (detail). Figures 5.6 (c) and (d) show the angle distribution at each tissue sample for the α and β populations, respectively. We conducted a one-direction Anova test for each population of PK network branch angles, which determined that the values of the α population are not drawn from the same sample ($p=0.0013$), and therefore they belong to two different populations. These acute angles presented a mean of $55.2^\circ \pm 20.6^\circ$, with values within the range $[20^\circ, 90^\circ]$, as illustrated in Figure 5.6 (c). In the case of obtuse angles (β) the Anova test showed these angles as to belong to the same population. The average of β

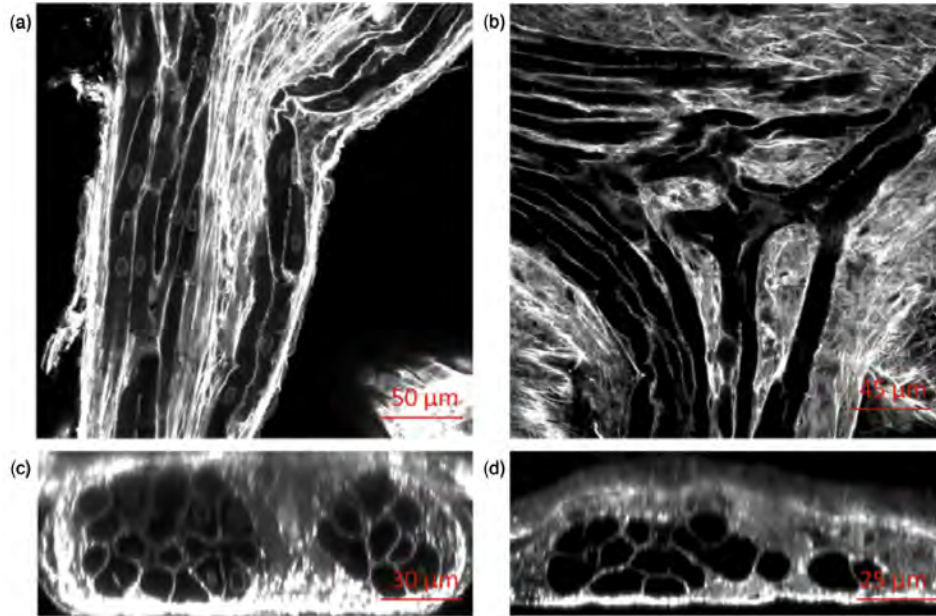


Figure 5.5: Purkinje free running strand type II. (a)-(b) are longitudinal sections, and (c)-(d) their corresponding cross-sections.

angles was $140.19^\circ \pm 25.8^\circ$. From these values the selection of β angles seems to range the entire interval $[90^\circ, 180^\circ]$. The blue boxes in Figures 5.6 (c) and (d) indicate the 25th and 75th percentiles, while the red and dashed lines represent the median and extreme values, respectively. On the other hand, the mean values for β angles are drawn from the same population ($p=0.1116$).

5.3.5 Complex network analysis

The complexity graph measurements performed on the extracted conduction pathways is shown in Figure 5.7. The numerical order of the tissue samples (rows) corresponds to the order in which the data is presented in Figures 5.6 (c) and (d). GE and LE were computed for a 100 random and 100 lattice equivalent networks of the same size and degree distribution (means presented in Figure 5.7). The criteria for small-world connectivity were only satisfied in one case (first sample, #1 in Figure 5.7). Eleven networks presented a negative assortativity coefficient, being the simplest non-redundant network the one showing the smallest assortativity with a value of -0.667 , whereas the largest assortativity value was 0.066 . With respect to the node betweenness, the shift to the right of its histograms in Figure 5.7 indicates the presence of highly travelled nodes, which means that a breakdown of one of them would likely change the path of many signals. On the other hand a histogram with the curve shifted to the left represents networks with more balanced distribution of paths. In our analysis, 12 out of 16 samples showed histograms shifted to the

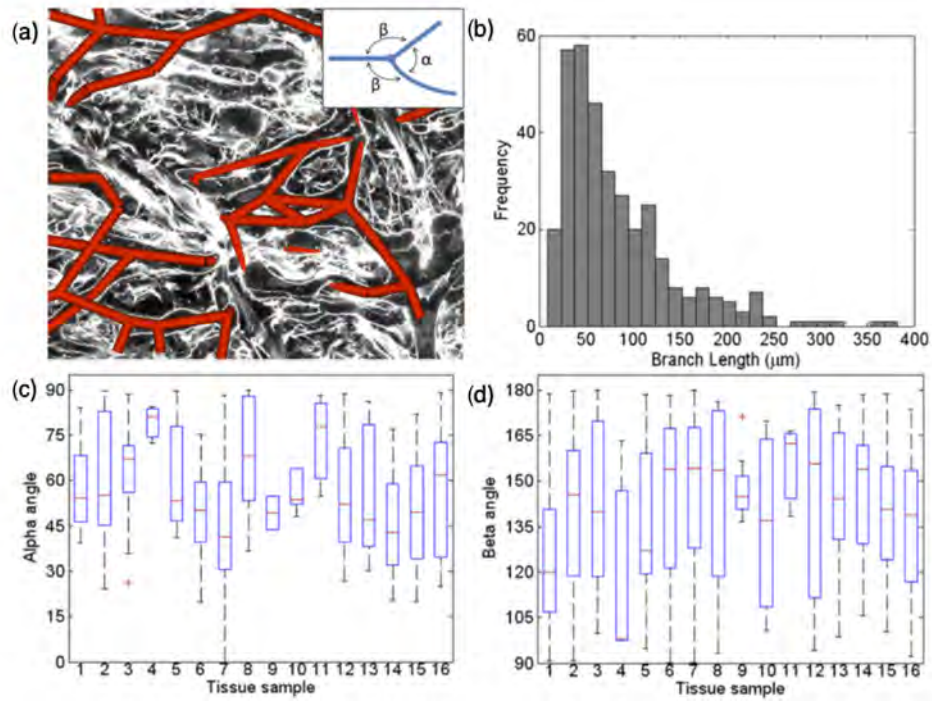


Figure 5.6: Angles and branch length analysis. (a) Overlap of confocal microscopy plane with the corresponding Purkinje centerlines. (b) Branch length histogram; boxplots of the (c) alpha and (d) beta angle distribution according to the corresponding tissue sample.

left, implying networks with redundant paths as observed in the path reconstructions.

5.4 Discussion and conclusions

The main goal of our work was to characterize the 3D nature of the PK system. Previously, morphology of the conduction system and the PK cells was described based on only 2D images instead of 3D stacks, which makes it difficult to draw conclusions on the arrangement of the cells and the network. Confocal microscopy images of the substructure of the PK network confirmed two types of cell morphology, as reported in [113], star-like and tubular PK cells. In the current work shape measurements were taken to characterize the two different cell populations. To our knowledge these PK cell measurements had not previously been taken from 3D reconstructions. Significant differences in cell lengths and diameters were established, although cells preserved a low variance in their surface to volume ratio (Table 1). These volume measurements are in good agreement to the values reported in [159], even though those were estimated on pig data: $5900 \mu\text{m}^2$ vs $5600 \mu\text{m}^2$ of surface area for [159] and for this work, respectively. On the other hand volume, surface/volume ratio indices and cell dimensions were substantially different ([159] vs this study): volume, $47\text{k} \mu\text{m}^3$ vs $16\text{k} \mu\text{m}^3$; surface/volume ratio, $0.15 \mu\text{m}^{-1}$ vs $0.35 \mu\text{m}^{-1}$; shorter in length but larger width in our study. Other researchers reported average dimensions of $164 \times 35 \mu\text{m}$ in canine isolated PK cells [154] and $129 \times 8 \mu\text{m}$ in rat isolated PK cells [176], which are comparable to our value of $120 \times 29 \mu\text{m}$ in rabbit PK cells. A possible explanation for some of these differences might be that measurements were mainly made on tubular cells. The morphological heterogeneity of PK cells raises the question of whether physiological differences are also present, being an interesting subject of further research. Differences in surface/volume ratios of cardiac working myocytes among mammalian species [149], and regional differences in myocyte dimensions have also been reported. A limited number of studies have been carried out to characterize the morphological and electrical behaviour of P_T s at the PMJs. Ryu et al. [147] described P_T from histological stained samples, as rectangular shaped with a centrally located nuclei, as compared to round or oval shaped PK cells. In our current work P_T were positively identified in several data stacks by inspecting the integrity of the T-system on their membrane: PK cells lacked the T-system structure therefore showing smooth continuous membranes; on the contrary myocardium cells usually had a dense regular pattern of dots on the membrane representing the invaginations of the T-system; finally P_T cells showed a more sparse membrane dotted pattern (Figure 5.3). Doubts have been cast as to the existence of these cells at PMJs across all species, although the presence of transitional cells has been confirmed at many other parts of the cardiac conduction system, specifically in areas of transition/connection to the working myocytes, as in the case of the sinus node, the AV node or the His bundle [153, 155]. It has been reported in the literature [169] that the connection between PK fibers and working myocytes occurs in either of the two following ways: i) through a 2D interface made of P_T that separates the PK

5. Analysis of the microstructure of the cardiac conduction system with confocal microscopy imaging












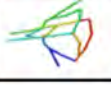

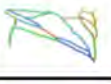







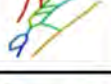


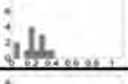
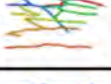



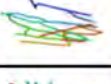

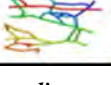
| Case | GE Latt | GE | GE Rand | LE Rand | LE | LE Latt | CP length | Assortativity | Betweenness | 3D model |
|------|---------|------|---------|---------|------|---------|-----------|---------------|--|---|
| 4 | 8,45 | 8,33 | 8,5 | 0 | 0 | 0 | 227,76 | -0,667 |  |  |
| 9 | 3,07 | 3,07 | 3,07 | 0 | 0 | 0 | 115,6 | -0,667 |  |  |
| 11 | 7,61 | 7,63 | 7,61 | 0 | 0 | 0 | 169,31 | -0,667 |  |  |
| 10 | 5,63 | 5,67 | 5,68 | 0 | 0 | 0 | 250,73 | -0,493 |  |  |
| 1 | 7,51 | 7,57 | 7,66 | 1 | 1,31 | 2,13 | 193,46 | -0,369 |  |  |
| 14 | 5,65 | 5,89 | 5,71 | 0,61 | 0 | 1,05 | 239,09 | -0,281 |  |  |
| 7 | 4,36 | 4,32 | 4,46 | 0,47 | 0,67 | 1,1 | 396,52 | -0,272 |  |  |
| 5 | 7,38 | 7,38 | 7,59 | 1,76 | 2,01 | 3,87 | 175,57 | -0,185 |  |  |
| 6 | 5,77 | 5,48 | 6,04 | 0,67 | 1,12 | 1,47 | 322,4 | -0,158 |  |  |
| 8 | 3,27 | 3,29 | 3,29 | 0,42 | 0 | 0,74 | 479,5 | -0,105 |  |  |
| 13 | 6,71 | 6,65 | 6,82 | 0,81 | 2,97 | 1,7 | 218,67 | -0,054 |  |  |
| 3 | 6,67 | 6,79 | 6,75 | 0,8 | 1,21 | 1,64 | 222,02 | 0,014 |  |  |
| 15 | 5,28 | 5,59 | 5,18 | 0,21 | 0 | 0,47 | 202,69 | 0,037 |  |  |
| 2 | 7,97 | 7,83 | 8,32 | 0,99 | 0 | 2,03 | 191,27 | 0,054 |  |  |
| 12 | 4,4 | 4,09 | 4,45 | 0,46 | 0,39 | 0,75 | 123,74 | 0,058 |  |  |
| 16 | 5,58 | 4,96 | 5,78 | 0,65 | 1,03 | 1,12 | 230,5 | 0,066 |  |  |

Figure 5.7: 3D model of reconstructed Purkinje networks and their corresponding graph theory measurements. *G.E.*: global efficiency, *G.E. Rand.*: global efficiency random, *G.E. Latt.*: global efficiency lattice, *L.E.*: local efficiency, *L.E. Rand.*: local efficiency random, *L.E.*: local efficiency lattice, *C.P. Length*: characteristic path length, *Assort.*: Assortativity.

fiber from the myocardium, and ii) through a funnel connection in which the narrow side is a PK fiber to which muscle fibers connect progressively. In canine hearts Rawling et al. [130] described the electrical properties of transitional cells, and their coupling to PK and myocardial cells, which supported the idea of punctual or funnel PMJ connections. In an electrical analysis of the PMJs they indicated that at some locations multiple PK activation signals contribute to the junction process while others appear to be substantially uncoupled from neighboring PK cell groups and the underlying transitional cells. This is contrary to the hypothesis of a 2D interconnection sheet (i.e. 2D interface) that connects PK and myocardium at many locations. The analysis of 3D confocal microscopy imaging data acquired on rabbits in this work suggests the presence of these two types of Purkinje-myocardium connections (i.e., 2D interface and funnel ones). The employed criteria were solely based on the proximity between cells and lack of collagen fibers in between them. We hypothesized that the connection among PMJs with 2D interfaces (Figure 5.3) is done through lateral connections of gap junctions. In different species connexins Cx43 and Cx40 have been found expressed on the sides of ventricular myocytes and PK fibers, respectively, although in much less density than at the cell ends. In [153] it was observed in mouse that Cx40 and Cx45 are co-expressed both in PK myocytes and in the underlying transitional cells, suggesting that Cx45 plays an important role in connecting up the Cx40/Cx43 PK myocyte compartment to the Cx43-expressing working ventricle via the transitional cells. Other structures of the cardiac conduction system such as FRPS were more easily identified. These structures are defined as cords made of a PK fiber bundle encased in connective tissue (i.e., collagen). They electrically link different parts of the endocardium [13]. False tendons have also been proven to carry PK fibers on the inside [107, 114]. Our study shows for the first time two different configurations of the PK fibers within the strand: i) type I strands, where all cells are in contact, therefore sharing electrical information (as can be observed in Figure 5.4); and ii) type II strands where two separated bundles run in parallel, with limited information exchange (Figure 5.5). Given the field of view of the available stacks of images we were not able to trace the strands to their origin. An intuitive approach at understanding the role of furcations points observed in these networks is to hypothesize that its main function is to combine electrical information by connecting PK fibers coming from different ends. We also hypothesize that type II strands might be the result of multiple strands coming together but without sharing conductive material. A possible explanation for maintaining electrical information segregated could be for safety issues; for instance if strand function is compromised at one end of the network (e.g. due to ischemia) the other ends can still receive electrical stimuli. The branch length pattern was found to follow an exponential distribution, in agreement with results previously reported for sheep [80], calf and lamb hearts [151] at the macroscopic level. The average lengths measured in these previous works cannot be strictly used for comparison given that the resolution of their images was substantially lower and studied species were also different. Nevertheless it is worthy to note that the branch length distribution provided by Ijiri et al. [80] has a range from 0 to 300 μm and an average length of 130 μm , whilst we have measured 84.6 μm in the present study on rabbits. With regard

to the angles between branches, in [151] angles of $60.0^\circ \pm 40^\circ$ were reported from macroscopic observations for acute angles (α), which are comparable to $55.2^\circ \pm 20.6^\circ$ obtained at microscopic level. For obtuse angles (β), macroscopic observations show a range of $160^\circ \pm 20^\circ$, whereas microscopic measurements show a wider range of $140.19^\circ \pm 25.8^\circ$. In the complex network analysis based on graph theory measurements, we made several observations. The majority of the extracted PK networks did not fulfill the small-world connectivity criterion (just one out of 16). This means that the PK networks studied at this resolution did not show high modularity (clusters of nodes highly interconnected between them), being quite sensitive to any possible insult to the network. This is in contrast to the behaviour of other networks in the human body such as the brain, where the small-world connectivity criterion is fulfilled [17]. Further research is still needed to study if small-world connectivity is fulfilled in PK networks at more macroscopic resolutions and with larger fields of view. Eleven out of 16 of the analyzed networks (69%) showed negative values of the assortativity coefficient, thus being vulnerable to insult (malfunctioning of a node or link), which correlates with the absence of small-world connectivity. Negative assortativity is a property that share biological networks in general, since high degree nodes such as star-like cells tend to join low degree nodes, such as tubular cells. When visually inspecting the reconstructed PK networks, one could easily identify four very simple networks, corresponding to non-plexus regions, which have the largest negative assortativity values. When ignoring simple networks in the study, there were a lower percentage of negative assortativity cases (58%). The low robustness to malfunctioning of some nodes in these networks could cause local microscopic conduction blocks due to alterations of network properties due to ischemia or pharmacological treatment among other factors. However, the PK network redundant structure observed at macroscopic level [8, 151] might compensate microscopic malfunctions. The betweenness measurement in the network analysis complemented the assortativity coefficient by providing local information about the relevance of a given node within the network. In our analysis, 12 out of 16 samples showed histograms shifted to the left, which involves a balanced distribution of PK network without critical hubs. This increases the safety factor of the network as a transmitter of the electrical impulse in case of a local damage of the structure. In addition, it is important to point out that in a PK network the electrical impulse does not travel only through the shortest paths, and that a damage or block in a section of the system, will only delay the impulse, but will not block it completely. The differentiation between PK and other myocardial cells was based on the high density of the T-system in working myocardial cells and its absence in PK ones. The use of WGA to identify the outer cell membrane, T-system and extracellular space has been established in a number of studies [23, 56]. Other authors have used a variety of techniques for similar purposes, such as light microscopy [169], scanning and transmission electron microscopy [37, 113, 155], and confocal microscopy with lipophilic fluorescent dye di-8-ANNEPS [159]. The segmentation of PK cells from 3D stacks was mainly manual given the complexity of the 3D structures and the imperfections in the WGA labelling. Semi-automatic methods such as region growing techniques were not effective due to the number of discontinuities on

the cell membrane, causing them to leak through into the extracellular space. Although several recent semi-automatic and automatic segmentation techniques in cell images have been proposed [152] manual techniques still remain the gold standard.

5.4.1 Limitations of the study

Analysis of imaging PK cells is a complex task, which involves labor-intensive experiments and tedious manual image processing where many tissue samples need to be acquired in order to have some of them fully analyzed. The results presented in this paper correspond to sparse tissue samples from different endocardial regions, instead of a single region, which prevented us to draw conclusions on local differences of the network. Another limitation was the lack of data to relate microscopic and macroscopic features in the same specimen. The hypothesis based on the existence of lateral connections on PMJs still needs further validation with Cx40-Cx43 labelling studies to confirm their presence in these areas of close proximity and lack of collagen. Finally, 10 datasets were processed to extract cell segmentations and then derive morphological indices due to the complexity of the task that was performed manually. The limited field of view of the acquired microscopic data resulted in simple networks with a small number of nodes and links, unlike dense networks (e.g. brain connectome) where graph metrics are usually applied, making some of the complexity network estimates difficult to interpret.

5.5 Conclusions

This study inspects the morphology of PK cells in 3D, revealing the different types of cell shapes, that conform the large network infrastructure of the cardiac conduction system at distal sections. The configurations and pathways formed by the PK system show a high (but heterogeneous) degree of robustness at the microscopic level as obtained after performing a network analysis. These results might help building more realistic computational PK systems at high resolution levels including different cell configurations (e.g. star- and tubular-shaped cells). In addition, better knowledge on the organization of the network might help in understanding the effects that several treatments such as radio-frequency ablation might have when the PK system is disrupted locally.

General Conclusions

6.1 Overview

The work developed in this thesis was motivated by the necessity to improve the accuracy of computational electrophysiology models of the heart that aimed predicting cardiac activation under different conditions. This goal very soon revealed the importance of modeling the CCS in detail from the anatomical and electrical points of view.

The first chapter of this manuscript reviews the anatomy and function of the CCS, and presents several computational models developed during the last years. Existing models had different drawbacks and were very simple, not being able to accurately reproduce the electrical activation sequences observed in-vivo. The CCS is a key component in a heart model aimed to simulate cardiac electrophysiology. Not only to reproduce the normal activation patterns, but also to study its complex interactions with the myocardium in common pathologies such as dilated cardiomyopathy (DCM) or hypertrophic cardiomyopathy (HCM).

The second chapter describes the methodology to develop the branching structure of a generic CCS manually, which was integrated into a patient specific heart geometry to study the interaction of the PK system with a pacing device (i.e. Cardiac Resynchronization Therapy) under normal and two pathological conditions (HCM and DCM). The model that was drawn on the endocardium of the patient, was only connected to the myocardium at the terminal PMJ points by connectors. A finite-element model was built to perform multi-scale biophysical simulations that took into account the ion dynamics of each type of cell present in the heart, including the anisotropic electrical propagation between adjacent cells. The simulation study revealed that models that do not consider the PK system will produce a large error in their estimates of important indices such as the degree of inter-ventricular dyssynchrony, which is used to optimise the pacing devices. This study demonstrated the importance of the retrograde activation at PMJs, when the

activation of the heart does not follow the normal pathways. In addition, substantial regional differences were observed depending on the pathology, i.e., the heart geometry, for the same activation protocol of the CRT leads. The most notable effect on the activation pattern was seen on the lateral wall, where the apical and basal segments changed their order of activation. This should be considered in clinical practice at the moment of the LV lateral wall lead positioning to improve the outcome of the procedure. However, the morphology of the PK model was not a faithful representation of a complex PK network, and did not reproduce accurately the patterns of activation, both anterogradely and retrogradely. Nevertheless, the developed model still produced simulation results remarkable similar to a normal pattern of electrical activation, following the typical apical to basal pattern.

Given the limitations of the first manually developed PK model, an automatic methodology to build a realistic CCS was developed, which is fully described in Chapter 3. In the proposed model PK networks are grown by using a set of user-defined parameters and mandatory hard-coded rules that control the main characteristics of the structure and ensure a more realistic result. The method is stochastic and produces different morphologies from a set of parameters following the principles derived from L-systems approaches. Given the relevance of the CCS network to simulate realistic cardiac activation sequences and the impossibility of obtaining patient-specific CCS structural data, a stochastic CCS model might help to achieve more accurate simulation results. The CCS structures built with this approach generate electrical activation sequences within physiological range without further user interaction than the selection of the input parameters. Nevertheless, the selection of these parameters was still a critical step in the methodology, having a large influence on the simulation results and requiring considerable fine tuning. An analysis of the CCS anatomy at macroscopic and microscopic level was carried out to find the (range of) most appropriate values for these parameters and thus improve the CCS networks automatically generated.

The fourth chapter is devoted to the developed methodology to extract Purkinje data from macroscopic images of calf and lamb hearts. Purkinje networks were marked with ink and subsequently segmented from the acquired images. Information on branch lengths and angles was obtained from several samples, and used to feed the algorithm to build the Purkinje network. After visual inspection of the results, the constructed CCS qualitatively resembled better the complex anatomy of real Purkinje systems than the previous models. In addition to the measured parameters a set of additional constraints were added to the model to control the growing with the aim of having a network incorporating the most relevant knowledge and observations described in the literature. This is especially important to model complex electrical pathologies. The sensitivity analysis carried out on the density of terminal branches and PMJs showed that there are not significant differences in TAT after increasing their density from 100 PMJs, which is related to the QRS width. Differences in angles between branches in the PK terminal branches did not induce significant overall differences in the branch patterns or activation maps. Nonetheless, the local activation pattern showed clear differences locally, which could be reflected on the QRS

morphology. The new stochastic CCS models that take into account these new histological knowledge-domain data, might help to achieve more accurate simulation results. The developed PK networks produced good properties from the macroscopic point of view but did not consider realistic characteristics at microscopic scale, neither for the morphology nor the density of PMJs.

Chapter 5 presents a study that was carried out to analyze the Purkinje network at microscopic level, and in particular its morphological structure and PMJs configuration, where Purkinje cells contact the working myocardium. We find out two different types of PK cell shapes that conform the large network infrastructure of the cardiac conduction system at distal sections. The configurations and pathways formed by the PK system showed a high (but heterogeneous) degree of robustness at the microscopic level as obtained after performing a network analysis using graph metrics. These results might help building more realistic computational PK systems at high resolution levels including different cell configurations (e.g. star- and tubular-shaped cells). In addition, better knowledge on the organization of the network might help in understanding the effects that several treatments such as radio-frequency ablation might have when the PK system is disrupted locally.

6.2 Outlook

The methods presented in this thesis are not a definite procedure to build the CCS in a computational model and present a number of limitations which should be addressed in the future.

6.2.1 Modeling of pathologies in cardiac electrophysiology

Electrophysiological experiments in cells, tissues and whole specimens have led to a rapid increase in the body of knowledge regarding the mechanisms underlying arrhythmias. Modeling and simulation of cardiac electrophysiology in normal and pathological conditions have played an important role not only in hypothesis-driven research at various levels of integration, but also in providing the framework for the unification of diverse experimental findings. With the increase in computer power during the past decades and the progress in imaging technologies, multi-scale, biophysically detailed models of the heart are finally (even if still slowly) being translated into clinical environments, as part of the emerging discipline of computational medicine by evaluating therapeutic approaches and contributing to the patient-specific optimization of cardiac care.

As this trend will continue in the future, cardiac modeling as a tool will necessitate continuous adaptation and integration of new elements, including model redesign and evaluation, improvements in the execution time of biophysically detailed cardiac models, implementation of consistent strategies for comparison with experimental measurements, and investing in efforts to ensure the repeatability and consistency of modeling results that are required to work in a medical context.

The evolution of cardiac modeling will continue to be strongly dependent on developments in experimental methodologies, which provide data to constrain, improve, and validate the models. Of particular importance will be the capability to better resolve the patho-physiological structure and interactions of the four different chambers of the heart (probably also including the overall cardiovascular system) and to fully characterize the complex electrophysiological and fibrotic remodeling in disease.

6.2.2 Evolution of models of the Purkinje system

Information of the cardiac conduction system has been continuously gathered over the last decades, but it has only been during the last years when it has become more relevant for the modeling of cardiac electrophysiology. Several models of the CCS exist already that include a tree-like structure, and a specific modeling of the PMJs, which shows the importance of having a complete description of the system instead of a simplified models with only PMJs. However, there is still a long way before a patient-specific model of the CCS can be incorporated to a model, due to the complexity of the system and the lack of data in patients. Nevertheless, Cardenes et al. [38] recently proposed a new methodology to constrain or estimate the location of the PMJs and a potential structure of the CCS using minimal cost geodesics techniques and the available sparse electrophysiological data from electro-anatomical maps. This combination of modeling and sparse data has shown promising preliminary results but still needs proper validation. In any case, the resulting reconstructed patient-specific PK networks can already provide the clinician information about the PK system that can be crucial in some interventions where the CCS plays a relevant role such as the ablation of fascicular (Purkinje-related) ventricular tachycardias or Cardiac Resynchronization Therapy.

Bibliography

- [1] Abboud S, Berenfeld O, and Sadeh D. Simulation of high-resolution QRS complex using a ventricular model with a fractal conduction system. Effects of ischemia on high-frequency QRS potentials. *Circ Res*, 68(6):1751–1760, June 1991. Cited on pages 14, 44 and 59.
- [2] Abraham WT. Rationale and design of a randomized clinical trial to assess the safety and efficacy of cardiac resynchronization therapy in patients with advanced heart failure: the Multicenter InSync Randomized Clinical Evaluation (MIRACLE). *J Card Fail*, 6(4):369–380, December 2000. Cited on page 22.
- [3] Achard S and Bullmore E. Efficiency and cost of economical brain functional networks. *PLoS Computational Biology*, 3:0174–0183, 2007. Cited on page 68.
- [4] Aliev RR and Panfilov AV. Modeling of heart excitation patterns caused by a local inhomogeneity. *Journal of Theoretical Biology*, 181:33–40, 1996. Cited on page 18.
- [5] Anderson RH. The disposition and innervation of atrioventricular ring specialized tissue in rats and rabbits. *J Anat*, 113(Pt 2):197–211, November 1972. Cited on page 45.
- [6] Anderson RH, Boyett MR, Dobrzynski H, and Moorman AFM. The anatomy of the conduction system: Implications for the clinical cardiologist. *Journal of Cardiovascular Translational Research*, 6:187–196, 2013. Cited on page 64.
- [7] Anderson RH and Ho SY. The morphology of the cardiac conduction system. *Novartis Found Symp*, 250:6–24, 276–279, 2003. Cited on pages 4, 5 and 7.
- [8] Ansari A, Ho SY, and Anderson RH. Distribution of the Purkinje fibres in the sheep heart. *Anat Rec*, 254(1):92–97, January 1999. Cited on pages 4, 36, 37, 38, 45, 51, 54, 58, 60, 64 and 78.
- [9] Aoki M, Okamoto Y, Musha T, and Harumi K. 3-dimensional computer simulation of depolarization and repolarization processes in the myocardium. *Japanese heart journal*, 27 Suppl 1:225–234, November 1986. Cited on page 14.
- [10] Aschoff L. Referat uber die Herzstoruenger in ihren Beziehungen zu den Spezifischen Muskelsystem des Herzens. *Verh Dtsch Pathol Ges*, 14:3–35, 1910. Cited on page 4.
- [11] Aslanidi OV, Stewart P, Boyett MR, and Zhang H. Optimal velocity and safety of discontinuous conduction through the heterogeneous Purkinje-ventricular junction. *Biophysical journal*, 97(1):20–39, July 2009. Cited on page 7.
- [12] Aslanidi OV, Stewart P, Boyett MR, and Zhang H. Optimal velocity and safety of discontinuous conduction through the heterogeneous Purkinje-ventricular junction. *Biophys J*, 97(1):20–39, July 2009. Cited on page 44.

- [13] Atkinson A, Inada S, Li J, Tellez JO, Yanni J, Sleiman R, Allah EA, Anderson RH, Zhang H, Boyett MR, and Dobrzynski H. Anatomical and molecular mapping of the left and right ventricular His-Purkinje conduction networks. *J Mol Cell Cardiol*, 51(5):689–701, June 2011. Cited on pages 59, 64 and 77.
- [14] Ayettey AS and Navaratnam V. The T-tubule system in the specialized and general myocardium of the rat. *Journal of anatomy*, 127:125–140, 1978. Cited on page 66.
- [15] Baher AA, Uy M, Xie F, Garfinkel A, Qu Z, and Weiss JN. Bidirectional ventricular tachycardia: ping pong in the His-Purkinje system. *Heart Rhythm*, 8(4):599–605, April 2011. Cited on page 44.
- [16] Baláti B, Varró A, and Papp JG. Comparison of the cellular electrophysiological characteristics of canine left ventricular epicardium, m cells, endocardium and purkinje fibres. *Acta Physiol Scand*, 164(2):181–90, Oct 1998. Cited on page 10.
- [17] Batale D, Eixarch E, Figueras F, Muñoz Moreno E, Bargallo N, Illa M, Acosta-Rojas R, Amat-Roldan I, and Gratacos E. Altered small-world topology of structural brain networks in infants with intrauterine growth restriction and its association with later neurodevelopmental outcome. *NeuroImage*, 60(2):1352–66, April 2012. Cited on pages 68 and 78.
- [18] Behradfar E, Nygren A, and Vigmond EJ. The role of purkinje-myocardial coupling during ventricular arrhythmia: A modeling study. *PLoS ONE*, 9(2):e88000, 02 2014. Cited on page 65.
- [19] Berenfeld O and Jalife J. Purkinje-muscle reentry as a mechanism of polymorphic ventricular arrhythmias in a 3-dimensional model of the ventricles. *Circ Res*, 82(10):1063–1077, June 1998. Cited on pages 14, 15, 16, 44 and 59.
- [20] Berenfeld O, Sadeh D, and Abboud S. Modeling of the heart’s ventricular conduction system using fractal geometry: spectral analysis of the QRS complex. *Ann Biomed Eng*, 21(2):125–134, 1993. Cited on page 14.
- [21] Berens P. CircStat: A MATLAB Toolbox for Circular Statistics. *Journal of Statistical Software*, 31, 2009. Cited on pages 47 and 69.
- [22] Bernabeu MO, Bordas R, Pathmanathan P, Pitt-Francis J, Cooper J, Garny A, Gavaghan DJ, Rodriguez B, Southern JA, and Whiteley JP. CHASTE: incorporating a novel multi-scale spatial and temporal algorithm into a large-scale open source library. *Philos Transact A Math Phys Eng Sci*, 367(1895):1907–1930, May 2009. Cited on page 37.
- [23] Bhavanandan VP and Katlic AW. The interaction of wheat germ agglutinin with sialoglycoproteins. The role of sialic acid. *The Journal of biological chemistry*, 254(10):4000–8, May 1979. Cited on page 78.
- [24] Bishop MJ and Plank G. Representing cardiac bidomain bath-loading effects by an augmented monodomain approach: application to complex ventricular models. *IEEE Trans Biomed Eng*, 58(4):1066–1075, April 2011. Cited on page 50.
- [25] Bishop SP, Oparil S, Reynolds RH, and Drummond JL. Regional myocyte size in normotensive and spontaneously hypertensive rats. *Hypertension*, 1(4):378–383, July 1979. Cited on page 65.
- [26] Boccaletti S, Latora V, Moreno Y, Chavez M, and Hwang D. Complex networks: Structure and dynamics, 2006. Cited on page 69.
- [27] Bordas R, Gillow K, Lou Q, Efimov IR, Gavaghan D, Kohl P, Grau V, and Rodriguez B. Rabbit-specific ventricular model of cardiac electrophysiological function including specialized conduction system. *Prog Biophys Mol Biol*, 107(1):90–100, October 2011. Cited on pages 44, 59 and 65.

- [28] Bordas R, Grau V, Burton RB, Hales P, Schneider JE, Gavaghan D, Kohl P, and Rodriguez B. Integrated approach for the study of anatomical variability in the cardiac Purkinje system: from high resolution MRI to electrophysiology simulation. *Conf Proc IEEE Eng Med Biol Soc*, 2010:6793–6796, 2010. Cited on pages 44, 50 and 64.
- [29] Boyett MR, Inada S, Yoo S, Li J, Liu J, Tellez J, Greener ID, Honjo H, Billeter R, Lei M, Zhang H, Efimov IR, and Dobrzynski H. Connexins in the sinoatrial and atrioventricular nodes. *Advances in cardiology*, 42:175–97, January 2006. Cited on page 65.
- [30] Boyle PM, Deo M, and Vigmond EJ. Behaviour of the Purkinje System During Defibrillation-Strength Shocks. In *Proc. 29th Annual International Conference of the IEEE Engineering in Medicine and Biology Society EMBS 2007*, pages 419–422, 2007. Cited on page 26.
- [31] Boyle PM, Deo M, Plank G, and Vigmond EJ. Purkinje-mediated effects in the response of quiescent ventricles to defibrillation shocks. *Ann Biomed Eng*, 38(2):456–468, February 2010. Cited on pages 44 and 59.
- [32] Bueno-Orovio A, Cherry EM, and Fenton FH. Minimal model for human ventricular action potentials in tissue. *J Theor Biol*, 253(3):544–560, August 2008. Cited on page 18.
- [33] Burashnikov A and Antzelevitch C. Differences in the electrophysiologic response of four canine ventricular cell types to alpha 1-adrenergic agonists. *Cardiovasc Res*, 43(4):901–8, Sep 1999. Cited on page 10.
- [34] Camara O, Sermesant M, Lamata P, Wang L, Pop M, Relan J, De Craene M, Delingette H, Liu H, Niederer S, Pashaei A, Plank G, Romero D, Sebastian R, Wong KCL, Zhang H, Ayache N, Frangi AF, Shi P, Smith NP, and Wright GA. Inter-model consistency and complementarity: learning from ex-vivo imaging and electrophysiological data towards an integrated understanding of cardiac physiology. *Prog Biophys Mol Biol*, 107(1):122–133, October 2011. Cited on page 18.
- [35] Camm AJ. Ablation for atrial fibrillation. *Nat Clin Pract Cardiovasc Med*, 3(7):345, Jul 2006. Cited on pages 24 and 25.
- [36] Campbell SE and Gerdes AM. Regional differences in cardiac myocyte dimensions and number in Sprague-Dawley rats from different suppliers. *Proceedings of the Society for Experimental Biology and Medicine. Society for Experimental Biology and Medicine (New York, N.Y.)*, 186(2):211–7, November 1987. Cited on page 65.
- [37] Canale E, Campbell G, Uehara Y, Fujiwara T, and Smolich J. Sheep cardiac Purkinje fibers: Configurational changes during the cardiac cycle. *Cell and Tissue Research*, 232(1):97–110, June 1983. Cited on page 78.
- [38] Cárdenes R, Sebastian R, Soto-Iglesias D, Berruezo A, and Camara O. Estimation of Purkinje trees from electro-anatomical mapping of the left ventricle using minimal cost geodesics. *Medical image analysis*, 24(1):52–62, August 2015. Cited on pages 65 and 84.
- [39] Castellant P, Fatemi M, Orhan E, Etienne Y, and Blanc JJ. Patients with non-ischaemic dilated cardiomyopathy and hyper-responders to cardiac resynchronization therapy: characteristics and long-term evolution. *Europace*, 11(3):350–5, Mar 2009. Cited on page 22.
- [40] Cates AW, Smith WM, Ideker RE, and Pollard AE. Purkinje and ventricular contributions to endocardial activation sequence in perfused rabbit right ventricle. *Am J Physiol Heart Circ Physiol*, 281(2):H490—H505, August 2001. Cited on pages 7, 9, 50, 60 and 64.
- [41] Cazeau S, Alonso C, Jauvert G, Lazarus A, and Ritter P. Cardiac resynchronization therapy. *Europace*, 5 Suppl 1:S42–S48, September 2004. Cited on page 22.

- [42] Cherry EM, Fenton FH, and Gilmour Jr RF. Mechanisms of ventricular arrhythmias: a dynamical systems-based perspective. *Am J Physiol Heart Circ Physiol*, 302(12):H2451—H2463, June 2012. Cited on pages 44 and 64.
- [43] Chinchapatnam P, Rhode KS, Ginks M, Mansi T, Peyrat JM, Lambiase P, Rinaldi C, Razavi R, Arridge S, and Sermesant M. Estimation of volumetric myocardial apparent conductivity from endocardial electro-anatomical mapping. *Conf Proc IEEE Eng Med Biol Soc*, 2009:2907–2910, 2009. Cited on page 44.
- [44] Chinchapatnam P, Rhode KS, Ginks M, Rinaldi CA, Lambiase P, Razavi R, Arridge S, and Sermesant M. Model-based imaging of cardiac apparent conductivity and local conduction velocity for diagnosis and planning of therapy. *IEEE Trans Med Imaging*, 27(11):1631–1642, November 2008. Cited on page 59.
- [45] Christoffels VM and Moorman AF. Development of the Cardiac Conduction System: Why Are Some Regions of the Heart More Arrhythmogenic Than Others? *Circ Arrhythmia Electrophysiol*, 2:195–197, 2009. Cited on page 4.
- [46] Chung ES, Leon AR, Tavazzi L, Sun JP, Nihoyannopoulos P, Merlino J, Abraham WT, Ghio S, Leclercq C, Bax JJ, Yu CM, Gorcsan J, Sutton MSJ, Sutter JD, and Murillo J. Results of the Predictors of Response to CRT (PROSPECT) trial. *Circulation*, 117(20):2608–2616, May 2008. Cited on page 22.
- [47] Clayton RH, Bernus O, Cherry EM, Dierckx H, Fenton FH, Mirabella L, Panfilov AV, Sachse FB, Seemann G, and Zhang H. Models of cardiac tissue electrophysiology: progress, challenges and open questions. *Prog Biophys Mol Biol*, 104(1-3):22–48, January 2011. Cited on page 44.
- [48] Clerc L. Directional differences of impulse spread in trabecular muscle from mammalian heart. *J Physiol*, 255(2):335–346, February 1976. Cited on pages 25 and 50.
- [49] Davies F. THE CONDUCTING SYSTEM OF THE VERTEBRATE HEART. *Br Heart J*, 4(3):66–76, July 1942. Cited on pages 45 and 64.
- [50] De Almeida M, Lopes F, Fontes P, Barra F, Guimaraes R, and Vilhena V. Ungulates heart model: a study of the purkinje network using india ink injection, transparent specimens and computer tomography. *Anatomical Science International*, 90(4):240–250, 2015. Cited on page 64.
- [51] Demoulin JC. Étude de la microcirculation normale du tissu de conduction auriculo-ventriculaire humain. *Acta Anat.*, 89:100–108, 1974. Cited on pages 5 and 58.
- [52] Deo M, Boyle P, Plank G, and Vigmond E. Arrhythmogenic mechanisms of the Purkinje system during electric shocks: a modeling study. *Heart Rhythm*, 6(12):1782–1789, December 2009. Cited on pages 44 and 59.
- [53] Deo M, Boyle PM, Kim AM, and Vigmond EJ. Arrhythmogenesis by single ectopic beats originating in the Purkinje system. *Am J Physiol Heart Circ Physiol*, 299(4):H1002—H1011, October 2010. Cited on page 59.
- [54] DiFrancesco D and Noble D. A model of cardiac electrical activity incorporating ionic pumps and concentration changes. *Philos Trans R Soc Lond B Biol Sci*, 307(1133):353–398, January 1985. Cited on page 26.
- [55] Dobrzynski H, Anderson RH, Atkinson A, Borbas Z, D’Souza A, Fraser JF, Inada S, Logantha SJRJ, Monfredi O, Morris GM, Moorman AFM, Nikolaidou T, Schneider H, Szuts V, Temple IP, Yanni J, and Boyett MR. Structure, function and clinical relevance of the cardiac conduction system, including the atrioventricular ring and outflow tract tissues, 2013. Cited on pages 64 and 65.
- [56] Dolber PC, Beyer EC, Junker JL, and Spach MS. Distribution of gap junctions in dog and rat ventricle studied with a double-label technique. *Journal of molecular and cellular cardiology*, 24:1443–1457, 1992. Cited on page 78.

- [57] Dossall DJ, Cheng KA, Huang J, Allison JS, Allred JD, Smith WM, and Ideker RE. Transmural and endocardial Purkinje activation in pigs before local myocardial activation after defibrillation shocks. *Heart Rhythm*, 4(6):758–765, June 2007. Cited on page 9.
- [58] Durrer D, van Dam RT, Freud GE, Janse MJ, Meijler FL, and Arzbaecher RC. Total excitation of the isolated human heart. *Circulation*, 41(6):899–912, June 1970. Cited on pages 3, 4, 10, 11, 12, 16, 25, 29, 32, 40, 44, 56, 57 and 59.
- [59] Dux-Santoy L, Sebastian R, Felix-Rodríguez J, Ferrero JM, and Saiz J. Interaction of specialized cardiac conduction system with antiarrhythmic drugs: a simulation study. *IEEE Trans Biomed Eng*, 58(12):3475–3478, December 2011. Cited on pages 44 and 58.
- [60] Efimov IR, Nikolski VP, and Salama G. Optical imaging of the heart. *Circ Res*, 95(1):21–33, July 2004. Cited on page 64.
- [61] Einthoven W. Weiteres uber das Elektrokardiogram. *Pfluger Archiv Ges Physiol*, 122:517–548, 1908. Cited on page 4.
- [62] Fenton FH, Cherry EM, Karma A, and Rappel WJ. Modeling wave propagation in realistic heart geometries using the phase-field method. *Chaos*, 15(1):13502, March 2005. Cited on page 22.
- [63] Fenton FH and Karma A. Vortex dynamics in three-dimensional continuous myocardium with fiber rotation: Filament instability and fibrillation. *Chaos (Woodbury, N.Y.)*, 8:20–47, 1998. Cited on page 18.
- [64] Fink M, Niederer Sa, Cherry EM, Fenton FH, Koivumäki JT, Seemann G, Thul R, Zhang H, Sachse FB, Beard D, Crampin EJ, and Smith NP. Cardiac cell modelling: Observations from the heart of the cardiac physiome project. *Progress in Biophysics and Molecular Biology*, 104:2–21, 2011. Cited on pages 16 and 17.
- [65] FitzHugh R. Impulses and Physiological States in Theoretical Models of Nerve Membrane. *Biophysical Journal*, 1:445–466, 1961. Cited on page 18.
- [66] Frangi AF, Rueckert D, Schnabel JA, and Niessen WJ. Automatic construction of multiple-object three-dimensional statistical shape models: application to cardiac modeling. *IEEE Trans Med Imaging*, 21(9):1151–1166, September 2002. Cited on page 24.
- [67] Franzone PC, Guerri L, Pennacchio M, and Taccardi B. Spread of excitation in 3-D models of the anisotropic cardiac tissue. III. Effects of ventricular geometry and fiber structure on the potential distribution. *Math Biosci*, 151(1):51–98, July 1998. Cited on page 22.
- [68] Franzone PC, Guerri L, and Rovida S. Wavefront propagation in an activation model of the anisotropic cardiac tissue: asymptotic analysis and numerical simulations. *J Math Biol*, 28(2):121–176, 1990. Cited on page 18.
- [69] Gassis S and León AR. Cardiac resynchronization therapy: strategies for device programming, troubleshooting and follow-up. *J Interv Card Electrophysiol*, 13(3):209–222, September 2005. Cited on page 22.
- [70] Gerdes AM, Moore JA, Hines JM, Kirkland PA, and Bishop SP. Regional differences in myocyte size in normal rat heart. *The Anatomical record*, 215(4):420–6, August 1986. Cited on page 65.
- [71] Goldberger AL and West BJ. Fractals in physiology and medicine. *Yale J Biol Med*, 60(5):421–435, 1987. Cited on pages 44 and 59.
- [72] Gourdie RG, Severs NJ, Green CR, Rothery S, Germroth P, and Thompson RP. The spatial distribution and relative abundance of gap-junctional connexin40 and connexin43 correlate to functional properties of components of the cardiac atrioventricular conduction system. *J Cell Sci*, 105 (Pt 4):985–991, August 1993. Cited on page 65.

- [73] Guyton AC and Hall JE. *Textbook of Medical Physiology*, volume 51. Elsevier, 2006. Cited on page 64.
- [74] Hamamoto T, Tanaka H, Mani H, Tanabe T, Fujiwara K, Nakagami T, Horie M, Oyamada M, and Takamatsu T. In situ Ca^{2+} dynamics of Purkinje fibers and its interconnection with subjacent ventricular myocytes. *J Mol Cell Cardiol*, 38(4):561–569, April 2005. Cited on page 50.
- [75] Heidenreich E, Ferrero JM, Doblare M, and Rodriguez JF. Adaptive macro finite elements for the numerical solution of monodomain equation in cardiac electrophysiology. *Annals of biomedical engineering*, 38:2331–2345, 2010. Cited on page 17.
- [76] Henriquez CS and Papazoglou AA. Using computer models to understand the roles of tissue structure and membrane dynamics in arrhythmogenesis. *Proceedings of the IEEE*, 84(3):334–354, 1996. Cited on page 22.
- [77] Hodgkin AL and Huxley AF. A quantitative Description of Membrane Currents and its Application to Conduction and Excitation in Nerve. *Journal of Physiology*, 177:500–544, 1952. Cited on pages 9 and 16.
- [78] Hunter PJ, Pullan AJ, and Smaill BH. Modeling total heart function. *Annu Rev Biomed Eng*, 5:147–177, 2003. Cited on page 44.
- [79] Hyde ER, Behar JM, Claridge S, Jackson T, Lee AWC, Remme EW, Sohal M, Plank G, Razavi R, Rinaldi CA, and Niederer SA. Beneficial Effect on Cardiac Resynchronization From Left Ventricular Endocardial Pacing Is Mediated by Early Access to High Conduction Velocity Tissue: Electrophysiological Simulation Study. *Circulation: Arrhythmia and Electrophysiology*, 8(5):1164–1172, October 2015. Cited on page 65.
- [80] Ijiri T, Ashihara T, Yamaguchi T, Takayama K, Igarashi T, Shimada T, Namba T, Haraguchi R, and Nakazawa K. A procedural method for modeling the Purkinje fibers of the heart. *J Physiol Sci*, 58(7):481–486, December 2008. Cited on pages 36, 44, 48, 49, 50, 52, 65 and 77.
- [81] JE P. Mikroskopisch-neurologische beoachtungen. *Arch Anat Physiol*, 12:281–295, 1845. Cited on page 4.
- [82] Jie X and Trayanova NA. Mechanisms for initiation of reentry in acute regional ischemia phase 1B. *Heart Rhythm*, 7(3):379–386, March 2010. Cited on page 44.
- [83] Jouk PS, Mourad A, Milisic V, Michalowicz G, Raoult A, Caillerie D, and Usson Y. Analysis of the fiber architecture of the heart by quantitative polarized light microscopy. Accuracy, limitations and contribution to the study of the fiber architecture of the ventricles during fetal and neonatal life. *Eur J Cardiothorac Surg*, 31(5):915–921, May 2007. Cited on pages 25 and 49.
- [84] Kamireddy S, Agarwal SK, Adelstein E, Jain S, and Saba S. Correlation of electrical and mechanical reverse remodeling after cardiac resynchronization therapy. *Ann Noninvasive Electrocardiol*, 14(2):153–7, Apr 2009. Cited on page 33.
- [85] Kawashima T and Sasaki H. Gross anatomy of the human cardiac conduction system with comparative morphological and developmental implications for human application. *Ann Anat*, 193(1):1–12, February 2011. Cited on page 50.
- [86] Keener JP. An eikonal-curvature equation for action potential propagation in myocardium. *J Math Biol*, 29(7):629–651, 1991. Cited on page 18.
- [87] Kerckhoffs RCP, Bovendeerd PHM, Kotte JCS, Prinzen FW, Smits K, and Arts T. Homogeneity of cardiac contraction despite physiological asynchrony of depolarization: a model study. *Ann Biomed Eng*, 31(5):536–547, May 2003. Cited on page 23.

- [88] Kerckhoffs RCP, Faris OP, Bovendeerd PHM, Prinzen FW, Smits K, McVeigh ER, and Arts T. Timing of depolarization and contraction in the paced canine left ventricle: model and experiment. *J Cardiovasc Electrophysiol*, 14(10 Suppl):S188—S195, October 2003. Cited on pages 3, 22, 23, 32 and 59.
- [89] Kimmel MW, Skadsberg ND, Byrd CL, Wright DJ, Laske TG, and Iaizzo PA. Single-site ventricular and biventricular pacing: investigation of latest depolarization strategy. *Europace*, 9(12):1163–1170, December 2007. Cited on pages 29 and 59.
- [90] Krishnamoorthy J, Lakshmanan A, and Mulasari A. Focal purkinje ventricular tachycardia ablation in structurally normal heart. *Asian Cardiovasc Thorac Ann*, 23(7):855–7, Sep 2015. Cited on page 65.
- [91] Lackey DP, Carruth ED, Lasher RA, Boenisch J, Sachse FB, and Hitchcock RW. Three-dimensional modeling and quantitative analysis of gap junction distributions in cardiac tissue. *Annals of biomedical engineering*, 39(11):2683–94, November 2011. Cited on pages 65 and 67.
- [92] Larrabide I, Omedas P, Martelli Y, Planes X, Nieber M, Moya JA, Butakoff C, Sebastian R, Camara O, Craene MD, Bijmens BH, and Frangi AF. *Func Imaging and Modeling of the Heart - Lecture Notes in Computer Science 5528*, chapter Gimias: An open source framework for efficient development of research tools and clinical prototypes, pages 417–426. Springer-Verlag, 2010. Cited on page 49.
- [93] Lasher Ra, Hitchcock RW, and Sachse FB. Towards modeling of cardiac micro-structure with catheter-based confocal microscopy: a novel approach for dye delivery and tissue characterization. *IEEE transactions on medical imaging*, 28(8):1156–64, August 2009. Cited on pages 65 and 66.
- [94] Lindenmayer A. Mathematical models for cellular interactions in development. I. Filaments with one-sided inputs. *J Theor Biol*, 18(3):280–299, March 1968. Cited on page 48.
- [95] Liu DW, Gintant GA, and Antzelevitch C. Ionic bases for electrophysiological distinctions among epicardial, midmyocardial, and endocardial myocytes from the free wall of the canine left ventricle. *Circ Res*, 72(3):671–687, March 1993. Cited on page 17.
- [96] Lopez-Perez A, Sebastian R, and Ferrero JM. Three-dimensional cardiac computational modelling: methods, features and applications. *Biomedical engineering online*, 14:35, 2015. Cited on pages 3, 16 and 17.
- [97] Luo CH and Rudy Y. A model of the ventricular cardiac action potential. Depolarization, repolarization, and their interaction. *Circ Res*, 68(6):1501–1526, June 1991. Cited on page 37.
- [98] MacGowan GA, Shapiro EP, Azhari H, Siu CO, Hees PS, Hutchins GM, Weiss JL, and Rademakers FE. Noninvasive measurement of shortening in the fiber and cross-fiber directions in the normal human left ventricle and in idiopathic dilated cardiomyopathy. *Circulation*, 96(2):535–41, Jul 1997. Cited on page 25.
- [99] Maleckar MM, Greenstein JL, Giles WR, and Trayanova Na. K⁺ current changes account for the rate dependence of the action potential in the human atrial myocyte. *American journal of physiology. Heart and circulatory physiology*, 297:H1398–H1410, 2009. Cited on page 17.
- [100] Massing GK and James TN. Anatomical configuration of the His bundle and bundle branches in the human heart. *Circulation*, 53(4):609–621, April 1976. Cited on pages 4, 33, 44, 50 and 58.
- [101] Miller WT and Geselowitz DB. Simulation studies of the electrocardiogram. I. The normal heart. *Circ. Res.*, 43:301–315, 1978. Cited on pages 16 and 18.
- [102] Miquerol L, Meysen S, Mangoni M, Bois P, van Rijen HVM, Abran P, Jongasma H, Nargeot J, and Gros D. Architectural and functional asymmetry of the His-Purkinje system of the murine heart. *Cardiovasc Res*, 63(1):77–86, July 2004. Cited on page 64.
- [103] Mitchell CC and Schaeffer DG. A two-current model for the dynamics of cardiac membrane. *Bulletin of Mathematical Biology*, 65:767–793, 2003. Cited on page 18.

- [104] Monckeberg JG. Beitrage zur normalen und pathologischen Anatomie des Herzens. *Verh Dtsch Pathol Ges*, 14:64–71, 1910. Cited on page 4.
- [105] Moorman AF, de Jong F, Denyn MM, and Lamers WH. Development of the cardiac conduction system. *Circ Res*, 82(6):629–644, April 1998. Cited on page 9.
- [106] Myerburg RJ, Gelband H, Nilsson K, Castellanos A, Morales AR, and Bassett AL. The role of canine superficial ventricular muscle fibers in endocardial impulse distribution. *Circ Res*, 42(1):27–35, January 1978. Cited on pages 29 and 60.
- [107] Myerburg RJ, Nilsson K, and Gelband H. Physiology of canine intraventricular conduction and endocardial excitation. *Circ Res*, 30(2):217–243, February 1972. Cited on pages 6, 10, 11, 13, 27, 35, 36, 38, 44, 45, 50, 58, 60, 64 and 77.
- [108] Nanthakumar K, Jalife J, Massé S, Downar E, Pop M, Asta J, Ross H, Rao V, Mironov S, Sevaptisidis E, Rogers J, Wright G, and Dhopeswarkar R. Optical mapping of langendorff-perfused human hearts: establishing a model for the study of ventricular fibrillation in humans. *Am J Physiol Heart Circ Physiol*, 293(1):H875–80, Jul 2007. Cited on page 25.
- [109] Noble D. Modeling the heart. *Physiology (Bethesda)*, 19:191–197, August 2004. Cited on page 2.
- [110] Noble D. From the Hodgkin-Huxley axon to the virtual heart. *J Physiol*, 580(Pt 1):15–22, April 2007. Cited on pages 2, 22 and 44.
- [111] Noble D and Rudy Y. Models of Cardiac Ventricular Action Potentials: Iterative Interaction between Experiment and Simulation. *Philosophical Transactions: Mathematical, Physical and Engineering Sciences*, 359(1783):1127–1142, 2001. Cited on page 22.
- [112] O’Hara T, Virág L, Varró A, and Rudy Y. Simulation of the undiseased human cardiac ventricular action potential: model formulation and experimental validation. *PLoS computational biology*, 7:e1002061, 2011. Cited on page 17.
- [113] Ono N, Yamaguchi T, and Ishikawa H. Morphological varieties of the Purkinje fiber network in mammalian hearts, as revealed by light and electron microscopy. *Archives of histology and cytology*, 72(3):139–149, 2009. Cited on pages 64, 65, 75 and 78.
- [114] Oosthoek PW, Viragh S, Lamers WH, and Moorman AF. Immunohistochemical delineation of the conduction system. II: The atrioventricular node and Purkinje fibers. *Circ Res*, 73(3):482–491, September 1993. Cited on pages 44, 49, 50, 64, 71 and 77.
- [115] Ordas S, Oubel E, Sebastian R, and Frangi AF. Computational Atlas of the Heart. In *15th International Symposium on Image and Signal Processing and Analysis*. IEEE Computer Society, 2007. Cited on page 24.
- [116] Persson F, Andersson B, Duker G, Jacobson I, and Carlsson L. Functional effects of the late sodium current inhibition by azd7009 and lidocaine in rabbit isolated atrial and ventricular tissue and purkinje fibre. *Eur J Pharmacol*, 558(1-3):133–43, Mar 2007. Cited on page 10.
- [117] Pieper S, Halle M, and Kikinis R. 3D Slicer. In *2004 2nd IEEE International Symposium on Biomedical Imaging: Nano to Macro (IEEE Cat No. 04EX821)*, pages 632–635, 2004. Cited on page 67.
- [118] Pitt-Francis J, Bernabeu MO, Cooper J, Garry A, Momtahan L, Osborne J, Pathmanathan P, Rodriguez B, Whiteley JP, and Gavaghan DJ. Chaste: using agile programming techniques to develop computational biology software. *Philos Transact A Math Phys Eng Sci*, 366(1878):3111–3136, September 2008. Cited on page 49.

- [119] Plank G, Burton RAB, Hales P, Bishop M, Mansoori T, Bernabeu MO, Garny A, Prassl AJ, Bollensdorff C, Mason F, Mahmood F, Rodriguez B, Grau V, Schneider JE, Gavaghan D, and Kohl P. Generation of histo-anatomically representative models of the individual heart: tools and application. *Philos Transact A Math Phys Eng Sci*, 367(1896):2257–2292, June 2009. Cited on page 44.
- [120] Plank G, Liebmann M, dos Santos RW, Vigmond EJ, and Haase G. Algebraic multigrid preconditioner for the cardiac bidomain model. *IEEE Trans Biomed Eng*, 54(4):585–596, April 2007. Cited on page 26.
- [121] Plonsey R. Bioelectric sources arising in excitable fibers. *Ann Biomed Eng*, 16(6):519–546, 1988. Cited on pages 26 and 50.
- [122] Pollard AE and Barr RC. The construction of an anatomically based model of the human ventricular conduction system. *IEEE Trans Biomed Eng*, 37(12):1173–1185, 1990. Cited on pages 14 and 16.
- [123] Pollard AE and Barr RC. Computer simulations of activation in an anatomically based model of the human ventricular conduction system. *IEEE Trans Biomed Eng*, 38(10):982–996, 1991. Cited on pages 3, 10, 44 and 59.
- [124] Pollard AE, Burgess MJ, and Spitzer KW. Computer simulations of three-dimensional propagation in ventricular myocardium. Effects of intramural fiber rotation and inhomogeneous conductivity on epicardial activation. *Circ Res*, 72(4):744–756, April 1993. Cited on page 22.
- [125] Potse M, Dubé B, Richer J, Vinet A, and Gulrajani RM. A comparison of monodomain and bidomain reaction-diffusion models for action potential propagation in the human heart. *IEEE Trans Biomed Eng*, 53(12 Pt 1):2425–2435, December 2006. Cited on pages 22, 26 and 50.
- [126] Prinzen FW and Peschar M. Relation between the pacing induced sequence of activation and left ventricular pump function in animals. *Pacing Clin Electrophysiol*, 25(4 Pt 1):484–498, April 2002. Cited on pages 59 and 60.
- [127] Prusinkiewicz P and Lindenmayer A. *The Algorithmic Beauty of Plants*. Springer Verlag, 2004. Cited on page 48.
- [128] Ramanathan C, Jia P, Ghanem R, Ryu K, and Rudy Y. Activation and repolarization of the normal human heart under complete physiological conditions. *Proc Natl Acad Sci U S A*, 103(16):6309–6314, April 2006. Cited on pages 12, 13 and 25.
- [129] Ramirez E, Saiz J, Romero L, Ferrero JM, and Trenor B. In silico ischaemia-induced reentry at the Purkinje-ventricle interface. *Europace*, 16:444–451, 2014. Cited on page 65.
- [130] Rawling DA and Joyner RW. Characteristics of junctional regions between Purkinje and ventricular muscle cells of canine ventricular subendocardium. *Circ Res*, 60(4):580–585, April 1987. Cited on pages 7, 64 and 77.
- [131] Relan J, Chinchapatnam P, Sermesant M, Rhode K, Delingette H, Razavi R, and Ayache N. Coupled personalisation of electrophysiology models for simulation of induced ischemic ventricular tachycardia. *Med Image Comput Comput Assist Interv*, 13(Pt 2):420–428, 2010. Cited on page 18.
- [132] Relan J, Chinchapatnam P, Sermesant M, Rhode K, Ginks M, Delingette H, Rinaldi CA, Razavi R, and Ayache N. Coupled personalization of cardiac electrophysiology models for prediction of ischaemic ventricular tachycardia. *Interface Focus*, 1(3):396–407, Jun 2011. Cited on page 59.
- [133] Relan J, Pop M, Delingette H, Wright G, Ayache N, and Sermesant M. Personalisation of a Cardiac Electrophysiology Model using Optical Mapping and MRI for Prediction of Changes with Pacing. *IEEE Trans Biomed Eng*, 58(12):3339–3349, January 2011. Cited on page 59.

- [134] Reumann M, Farina D, Miri R, Lurz S, Osswald B, and Dossel O. Computer model for the optimization of AV and VV delay in cardiac resynchronization therapy. *Med Biol Eng Comput*, 45(9):845–854, September 2007. Cited on pages 22 and 23.
- [135] Rinaldi CA and Gill JS. The implantable cardioverter defibrillator. *Hosp Med*, 63(11):672–5, Nov 2002. Cited on page 23.
- [136] Roberts BN, Yang PC, Behrens SB, Moreno JD, and Clancy CE. Computational approaches to understand cardiac electrophysiology and arrhythmias. *AJP: Heart and Circulatory Physiology*, 303:H766–H783, 2012. Cited on page 17.
- [137] Robinson RB, Boyden PA, Hoffman BF, and Hewett KW. Electrical restitution process in dispersed canine cardiac purkinje and ventricular cells. *Am J Physiol*, 253(5 Pt 2):H1018–25, Nov 1987. Cited on page 10.
- [138] Rodríguez B, Li L, Eason JC, Efimov IR, and Trayanova NA. Differences between left and right ventricular chamber geometry affect cardiac vulnerability to electric shocks. *Circ Res*, 97(2):168–175, July 2005. Cited on page 22.
- [139] Romero D, Zimmerman V, Sebastian R, and Frangi AF. Flexible Modeling for Anatomically-Based Cardiac Conduction System. In *IEEE Annual International Conference on Engineering in Medicine and Biology Conference (EMBS)*, 2010. Cited on page 36.
- [140] Romero D, Sachse FB, Sebastian R, and Frangi AF. Towards High Resolution Computational Models of the Cardiac Conduction System : A Pipeline for Characterization of Purkinje-Ventricular-Junctions. In *Functional Imaging and Modelling of the Heart*, volume 6666 of *Lecture Notes in Computer Science*, pages 28–35. Springer-verlag Berlin Heidelberg, 2011. Cited on page 66.
- [141] Romero D, Sebastian R, Bijnens BH, Zimmerman V, Boyle PM, Vigmond EJ, and Frangi AF. Effects of the purkinje system and cardiac geometry on biventricular pacing: a model study. *Ann Biomed Eng*, 38(4):1388–1398, April 2010. Cited on pages 36 and 44.
- [142] Romero D, Zimmerman V, Sebastian R, and Frangi AF. Flexible modeling for anatomically-based cardiac conduction system construction. *Conf Proc IEEE Eng Med Biol Soc*, 2010:779–782, 2010. Cited on page 65.
- [143] Roth BJ. The electrical potential produced by a strand of cardiac muscle: a bidomain analysis. *Annals of biomedical engineering*, 16:609–637, 1988. Cited on page 18.
- [144] RS H. Photoelectric Color-Difference Meter. *Journal of the Optical Society of America*, 38(6):661, 1948. Cited on page 46.
- [145] Rubinov M and Sporns O. Complex network measures of brain connectivity: Uses and interpretations. *NeuroImage*, 52:1059–1069, 2010. Cited on pages 68 and 69.
- [146] Rudy Y and Silva JR. Computational biology in the study of cardiac ion channels and cell electrophysiology. *Quarterly reviews of biophysics*, 39:57–116, 2006. Cited on page 17.
- [147] Ryu S, Yamamoto S, Andersen CR, Nakazawa K, Miyake F, and James TN. Intramural purkinje cell network of sheep ventricles as the terminal pathway of conduction system. *Anat Rec (Hoboken)*, 292(1):12–22, January 2009. Cited on pages 4, 7, 8, 45, 49, 50, 54, 64 and 75.
- [148] Sanchez-Quintana D and Ho SY. Anatomy of cardiac nodes and atrioventricular specialized conduction system. *Rev Esp Cardiol*, 56(11):1085–1092, November 2003. Cited on pages 4 and 58.

- [149] Satoh H, Delbridge LM, Blatter LA, and Bers DM. Surface:volume relationship in cardiac myocytes studied with confocal microscopy and membrane capacitance measurements: species-dependence and developmental effects. *Biophysical Journal*, 70:1494–1504, 1996. Cited on page 75.
- [150] Sebastian R, Zimmerman V, Romero D, and Frangi AF. Construction of a Computational Anatomical Model of the Peripheral Cardiac Conduction System. *IEEE Trans Biomed Eng*, 58(12):3479–3482, 2011. Cited on pages 45, 47 and 48.
- [151] Sebastian R, Zimmerman V, Romero D, Sanchez-Quintana D, and Frangi AF. Characterization and modeling of the peripheral cardiac conduction system. *IEEE Trans Med Imaging*, 32(1):45–55, January 2013. Cited on pages 64, 65, 77 and 78.
- [152] Seidel T, Edelmann JC, and Sachse FB. Analyzing Remodeling of Cardiac Tissue: A Comprehensive Approach Based on Confocal Microscopy and 3D Reconstructions. *Annals of biomedical engineering*, September 2015. Cited on page 79.
- [153] Severs NJ, Bruce AF, Dupont E, and Rothery S. Remodelling of gap junctions and connexin expression in diseased myocardium. *Cardiovascular research*, 80(1):9–19, October 2008. Cited on pages 65, 75 and 77.
- [154] Sheets MF, January CT, and Fozzard Ha. Isolation and characterization of single canine cardiac purkinje cells. *Circulation Research*, 53:544–548, 1983. Cited on pages 64 and 75.
- [155] Shimada T, Noguchi T, Asami I, and Campbell GR. Functional morphology of the conduction system and the myocardium in the sheep heart as revealed by scanning and transmission electron microscopic analyses. *Arch Histol Jpn*, 49(3):283–295, August 1986. Cited on pages 50, 51, 75 and 78.
- [156] Si H. Tetgen: a quality tetrahedral mesh generator and three-dimensional Delaunay triangulator. Technical report, Weierstrass Institute for Applied Analysis and Stochastics, 2004. Cited on page 49.
- [157] Simelius K, Nenonen J, and Horáček M. Modeling Cardiac Ventricular Activation. *International Journal of Bioelectromagnetism*, 3:51–58, 2001. Cited on pages 16 and 59.
- [158] SINHA A and Schmidt M. Role of Left Ventricular Scar and Purkinje-Like Potentials During Mapping and Ablation of Ventricular Fibrillation in Dilated Cardiomyopathy. *Pacing and clinical electrophysiology*, 32(March):286–290, 2009. Cited on page 65.
- [159] Stankovicova T, Bito V, Heinzl F, and Mubagwa K. Isolation and Morphology of Single Purkinje Cells from the Porcine Heart. *Ge. Physiol. Biophys.*, 22:329–340, 2003. Cited on pages 65, 75 and 78.
- [160] Stephenson RS, Boyett MR, Hart G, Nikolaidou T, Cai X, Corno AF, Alphonso N, Jeffery N, and Jarvis JC. Contrast enhanced micro-computed tomography resolves the 3-dimensional morphology of the cardiac conduction system in mammalian hearts. *PLoS ONE*, 7(4):e35299, 04 2012. Cited on page 64.
- [161] Stewart P, Aslanidi OV, Noble D, Noble PJ, Boyett MR, and Zhang H. Mathematical models of the electrical action potential of Purkinje fibre cells. *Philos Transact A Math Phys Eng Sci*, 367(1896):2225–2255, June 2009. Cited on pages 17 and 44.
- [162] Streeter DD. *Handbook of Physiology: The Cardiovascular System*, volume 1, chapter Gross morphology and fibrous structure of the heart, pages 61–112. Oxford University Press, 1979. Cited on page 25.
- [163] Streeter DD, Spotnitz HM, Patel DP, Ross J, and Sonneblich EH. Fiber Orientation in the Canine Left Ventricle During Diastole and Systole. *Circulation Research*, 24:339–347, 1969. Cited on page 49.
- [164] Szentadrassy N, Banyasz T, Biro T, Szabo G, Toth BI, Magyar J, Lazar J, Varro A, Kovacs L, and Nanasi PP. Apico-basal inhomogeneity in distribution of ion channels in canine and human ventricular myocardium. *Cardiovascular research*, 65:851–60, 2005. Cited on page 17.

- [165] Tabereaux PB, Walcott GP, Rogers JM, Kim J, Dossall DJ, Robertson PG, Killingsworth CR, Smith WM, and Ideker RE. Activation patterns of Purkinje fibers during long-duration ventricular fibrillation in an isolated canine heart model. *Circulation*, 116(10):1113–1119, September 2007. Cited on pages 9 and 65.
- [166] Tanaka H, Hamamoto T, and Takamatsu T. Toward an Integrated Understanding of the Purkinje Fibers in the Heart: The Functional and Morphological Interconnection between the Purkinje Fibers and Ventricular Muscle. *Acta Histochem. Cytochem.*, 38:257–265, 2005. Cited on pages 7 and 8.
- [167] Tawara S. Das Reizleitungssystem des Säugetierherzens. Eine anatomisch- histologische studie über das Atrioventricularbündel und die Purkinjeschen Fäden. *Jena, Verlag v. Gustav Fischer*, 1906. Cited on pages 4, 5, 7, 16, 44, 45, 50, 58 and 64.
- [168] Tobón C, Ruiz-Villa CA, Heidenreich E, Romero L, Hornero F, and Saiz J. A three-dimensional human atrial model with fiber orientation. Electrograms and arrhythmic activation patterns relationship. *PLoS one*, 8:e50883, 2013. Cited on page 17.
- [169] Tranum-Jensen J, Wilde AA, Vermeulen JT, and Janse MJ. Morphology of electrophysiologically identified junctions between Purkinje fibers and ventricular muscle in rabbit and pig hearts. *Circ Res*, 69(2):429–437, August 1991. Cited on pages 7, 44, 50, 58, 64, 75 and 78.
- [170] Trayanova N. Defibrillation of the heart: insights into mechanisms from modelling studies. *Exp Physiol*, 91(2):323–337, March 2006. Cited on page 44.
- [171] Tseng GN, Robinson RB, and Hoffman BF. Passive properties and membrane currents of canine ventricular myocytes. *J Gen Physiol*, 90(5):671–701, November 1987. Cited on page 10.
- [172] Tusscher KHT and Panfilov AV. Cell model for efficient simulation of wave propagation in human ventricular tissue under normal and pathological conditions. *Phys Med Biol*, 51(23):6141–6156, December 2006. Cited on pages 22 and 26.
- [173] Tusscher KHWJT and Panfilov AV. Modelling of the ventricular conduction system. *Prog Biophys Mol Biol*, 96(1-3):152–170, 2008. Cited on pages 3, 10, 16, 22, 36, 59 and 65.
- [174] Tusscher KHWJT, Bernus O, Hren R, and Panfilov AV. Comparison of electrophysiological models for human ventricular cells and tissues. *Prog Biophys Mol Biol*, 90(1-3):326–345, 2006. Cited on pages 49 and 61.
- [175] Vadakkumpadan F, Rantner LJ, Tice B, Boyle P, Prassl AJ, Vigmond E, Plank G, and Trayanova N. Image-based models of cardiac structure with applications in arrhythmia and defibrillation studies. *J Electrocardiol*, 42(2):157.e1—157.10, 2009. Cited on pages 36, 44, 59 and 64.
- [176] Vaidyanathan R, O’Connell RP, Deo M, Milstein ML, Furspan P, Herron TJ, Pandit SV, Musa H, Berenfeld O, Jalife J, and Anumonwo JMB. The ionic bases of the action potential in isolated mouse cardiac Purkinje cell. *Heart rhythm : the official journal of the Heart Rhythm Society*, 10:80–7, 2013. Cited on pages 64 and 75.
- [177] Vigmond EJ, dos Santos RW, Prassl AJ, Deo M, and Plank G. Solvers for the cardiac bidomain equations. *Prog Biophys Mol Biol*, 96(1-3):3–18, 2008. Cited on page 22.
- [178] Vigmond E, Vadakkumpadan F, Gurev V, Arevalo H, Deo M, Plank G, and Trayanova N. Towards predictive modelling of the electrophysiology of the heart. *Exp Physiol*, 94(5):563–577, May 2009. Cited on page 44.
- [179] Vigmond EJ and Clements C. Construction of a Computer Model to Investigate Sawtooth Effects in the Purkinje System. *IEEE Trans Biomed Eng.*, 54(3):389–399, 2007. Cited on pages 16, 26, 34, 59 and 61.

- [180] Vigmond EJ, Clements C, McQueen DM, and Peskin CS. Effect of bundle branch block on cardiac output: A whole heart simulation study. *Prog Biophys Mol Biol*, 97(2-3):520–542, 2008. Cited on page 22.
- [181] Vigmond EJ, Hughes M, Plank G, and Leon LJ. Computational tools for modeling electrical activity in cardiac tissue. *J Electrocardiol*, 36 Suppl:69–74, 2003. Cited on page 26.
- [182] Volders PG, Sipido KR, Carmeliet E, Spätjens RL, Wellens HJ, and Vos MA. Repolarizing K⁺ currents ITO1 and IKs are larger in right than left canine ventricular midmyocardium. *Circulation*, 99:206–210, 1999. Cited on page 17.
- [183] Vozzi C, Dupont E, Coppens SR, Yeh HI, and Severs NJ. Chamber-related differences in connexin expression in the human heart. *Journal of molecular and cellular cardiology*, 31:991–1003, 1999. Cited on page 65.
- [184] Whiteley JP. An efficient numerical technique for the solution of the monodomain and bidomain equations. *IEEE Trans Biomed Eng*, 53(11):2139–2147, November 2006. Cited on page 26.
- [185] Widran J and Lev M. The dissection of the atrioventricular node, bundle and bundle branches in the human heart. *Circulation*, 4(6):863–867, December 1951. Cited on page 50.
- [186] Wiedmann RT, Tan RC, and Joyner RW. Discontinuous conduction at Purkinje-ventricular muscle junction. *The American journal of physiology*, 271:H1507–H1516, 1996. Cited on pages 7 and 65.
- [187] Young AA and Frangi AF. Computational cardiac atlases: from patient to population and back. *Exp Physiol*, 94(5):578–596, May 2009. Cited on page 36.
- [188] Zimmerman V, Sebastian R, Bijnens BH, and Frangi AF. Modeling the Purkinje Conduction System with a Non Deterministic Rule Based Iterative Method. In *Computer in Cardiology*, volume 36, page 461–464, 2009. Cited on pages 36, 37, 49 and 59.

Acronyms

| | |
|-----------|---|
| AD | Anterior Division |
| AP(D) | Action Potential (Duration) |
| AVN | Atrioventricular Node |
| BB | Bundle Branches |
| CCS | Cardiac Conduction System |
| CRT | Cardiac Resynchronization Therapy |
| DAD | Delayed After-depolarization |
| DCM | Dilated Cardiomyopathy |
| EAD | Early After-depolarization |
| ECG | Electrocardiogram |
| FRPS | Free-Running Purkinje System |
| HB | His Bundle |
| HCM | Hypertrophic Cardiomyopathy |
| LAT | Local Activation Time |
| LBB(B) | Left Bundle Branch (Block) |
| LV | Left Ventricle |
| PD | Posterior Division |
| P_T | Transitional cell |
| PK | Purkinje |
| PKBB | Purkinje Backbone Branches |
| PKTB | Purkinje Terminal Branches |
| PMJ | Purkinje-Myocardial Junction |
| RBB(B) | Right Bundle Branch (Block) |
| RV(B) | Right Ventricle (Breakthrough) |
| SAN | Sinoatrial Node |
| TAT | Total Activation Time |
| V_{max} | Maximal rate of rise of the AP upstroke |
| VVD | Ventricle-Ventricle delay |
| WGA | Wheat Germ Agglutinin |

Curriculum Vitae



Daniel Romero García obtained his degree in Biomedical Engineering from the Escuela de Ingeniería de Antioquía, Medellín, Colombia (2006). From June 2005 to February 2007, Daniel worked as a contractor for Boston Scientific (Colombia) providing technical support services and clinical assistance in electrophysiology technologies and intravascular ultrasound. From 2007 to 2012 Daniel was a researcher in training at the CISTIB, group lead by Dr. Alejandro Frangi at the DTIC of the UPF, where in 2009 he earned his MSc in Information, Communication and Audiovisual Media Technologies. He joined in September 2012 the group PhySense. His main research interests include cardiac electrophysiology, modeling and simulations of the cardiac conduction system, the Purkinje network.

Publications

International Journal

1. **Romero D.**, Camara O., Sachse F., Sebastian R. Analysis of microstructure of the cardiac conduction system based on three-dimensional confocal microscopy. *PLOS One*, Submitted
2. Sebastian R., Zimmerman V., **Romero D.**, Sanchez-Quintana D., Frangi A.F. Characterization and Modeling of the Peripheral Cardiac Conduction System. *IEEE Transactions on Medical Imaging*, 32(1):45–55, 2013. IF: 3.643
3. Pashaei A., **Romero D.**, Sebastian R., Camara O., Frangi, AF. Fast Multiscale Modeling of Cardiac Electrophysiology Including Purkinje System. *IEEE Transactions on Biomedical Engineering*, Vol. 58(10):2956-2960 2011. IF: 2.278
4. Camara O., Sermesant M., Lamata P., Wang L., Pop M., Relan J., De Craene M., Delingette H., Liu H., Niederer S., Pashaei A., Plank G., **Romero D.**, Sebastian R., Wong K.C.L., Zhang H., Ayache N., Frangi A.F., Shif P., Smith N., Wright G.A. Inter-Model Consistency and Complementarity: Learning from ex-vivo Imaging and Electrophysiological Data towards an Integrated Understanding of Cardiac Physiology. *Progress in Biophysics and Molecular Biology*. 107(1):122-133, 2011. IF: 3.964
5. Sebastian R., Zimmerman V., **Romero D.**, Frangi A.F.. Construction of a Computational Anatomical Model of the Peripheral Cardiac Conduction System. *IEEE Transactions on Biomedical Engineering*, 58(12): 3479-82, 2011. IF: 2.278
6. **Romero D.**, Sebastian, R., Bijmens, B., Zimmerman, V., Boyle, PM., Vigmond, EJ., Frangi, AF. Effects of the Purkinje system and cardiac geometry on biventricular pacing: a model study. *Annals of Biomedical Engineering*, 39(4):1388-1398, 2010. IF: 2.374

Book chapters

1. **D. Romero**, F. B. Sachse, R. Sebastian and A.F. Frangi. Towards high resolution computational models of the cardiac conduction system: a pipeline for characterization of Purkinje-ventricular-junctions. *Functional Modeling and Imaging of the Heart*. Springer-verlag Berlin Heidelberg (LNCS 6666), pp. 28-35, 2011.
2. A. Pashaei, C. Hoogendoorn, **D. Romero**, R. Sebastian, O. Camara and A.F. Frangi. Effect of scar development on fast electrophysiological models of the human heart: In-silico study on atlas-based virtual populations. Springer-verlag Berlin Heidelberg (LNCS 6666), pp. 427-436, 2011.
3. **D. Romero**, R. Sebastian, B. H. Bijmens, V. Zimmerman, P. M. Boyle, E. J. Vigmond, A.F. Frangi, The Purkinje System and Cardiac Geometry: Assessing their Influence on the Paced Heart. Lecture Notes in Computer Science. *Functional Modeling and Imaging of the Heart*. Springer-verlag Berlin Heidelberg (LNCS 5528), Nice, France, 2009.

Peer-reviewed conference papers

1. A Pashaei, **D Romero**, R Sebastian, O Camara, AF Frangi. Comparison of phenomenological and biophysical cardiac models coupled with heterogenous structures for prediction of electrical activation sequence. *Computing in Cardiology*, Belfast, 2010.
2. O. Camara, B. H. Bijnens, E. Silva, D. Andreu, S. Oeltze, **D. Romero**, M. De Craene, D. Tamborero, R. Sebastian, L. Mont, M. Sitges A. F. Frangi. Dyssynchrony indices from an electrophysiological contact mapping system predict response to CRT. *MICCAI*, London, UK 2009.
3. **D.Romero**, V Zimmerman, R Sebastian and AF Frangi. Flexible Modeling for Anatomically-Based Cardiac Conduction System. *IEEE Annual International Conference on Engineering in Medicine and Biology Conference (EMBS)*, Buenos Aires, Argentina 2010.
4. **D.Romero**, R.Sebastian, G. Plank, E.J. Vigmond , A.F. Frangi. Modeling the influence of the VV delay for CRT on the electrical activation patterns in absence of conduction through the AV node. *SPIE Medical Imaging, Progress in biomedical optics and imaging. California, USA, February 2008.*

Conference abstracts

1. O. Camara, B. H. Bijnens, E. Silva, D. Andreu, S. Oeltze, **D. Romero**, M. De Craene, D. Tamborero, R. Sebastian, L. Mont, M. Sitges, AF Frangi. Detecting abnormal septal motion by combining spatial and electrical information from endocardial mapping. *European Society of Cardiology Congress (ESC)*, Barcelona, Spain, 2009.
2. R. Sebastian, **D. Romero**, V. Zimmerman, E. Vigmond, B.H. Bijnens, A.F. Frangi. Detailed cardiac electromechanical modeling and simulation. From medical images to simulation. *Euroecho, 12th Annual Meeting of the European Society of Cardiology*. Lyon, France, December, 2008.
3. Bijnens B. , Sebastian R., **Romero D.**, and Frangi A.F, Anatomico-functional model suitable for Cardiac Resynchronization therapy. *4th European Congress for Medical and Biomedical Engineering*, Antwerp, November 23-27, 2008.

Acknowledgements

The road that led to this thesis has been a wild one. So off paved, so much gravel and potholes that it broke my back not once, but twice. No one but me is to blame. But I would do it all again. The journey begins with a friend, Diana Bonilla, who got me a job interview for a project manager position at a lab in Barcelona. Luckily for me, Professor Alejandro Frangi saw potential in me to become a PhD student, and when I say “luckily for me” I mean it because I don’t know how to work; I’ve only known how to study. I would like to thank Alex for the opportunity to be included in his ambitious projects. But sadly my road and his did not align in the maps. I wish him nothing but the best in all his endeavors. Diana has been a friend, a sister and sometimes a mother, and for that I will always love her.

Who would have known that upon arriving in Barcelona with 500 euros for the whole first month, I would have met Hrvoje Bogunovic and Corné Hoogendoorn, whom without knowing my financial burdens would open the doors to their house to me, and offered me to pay the first month of rent after I got my first pay check. That’s a story I always fondly remember. Two of the greatest people I’ve had the pleasure to count as my friends, two of the kindest persons that remain beautiful people.

Dear reader, you might be thinking that I’m writing this with a straight face although with a melancholic feeling; nothing as far off from the hard truth. I’m pretty sure I won’t be able to finish this off while expressing my gratitude to all of “my people”. If I don’t call you by name, know that I know, and I’m thankful, I just found it hard to write this while sober. Know that I know, and that I remember the tall tales we lived through.

To my dear supervisor and friend Rafael Sebastián, know that whenever I tell this story I refer to you as a “mother without titties”. His incredible support among these years, even in those times I deserved a beating instead of his encouraging words, has been fundamental in completing this process, which at many times I wanted to quit. Your technical feedback and your infinite patience with a “know-it-all” punk like me, is nothing but short of praise. Your family, who showed me what a Paella Valenciana should be, and the origins of such a wonderful human being deserve to be recognized here for the beautiful people they are.

Dr friking Oscar Cámara. . . what can I say that I haven’t told you whilst drunk, you kind, dear sir? When I first expected you to come to Cilab for a presentation, I read your papers, and had so many questions for you. But the technical got superfluous when I

discovered the man behind the writing. If I'm every so lucky again in my life, I'll have a boss like you. But I find that very difficult to believe, since very few people will be willing to go skinny dipping in the Mediterranean in November. Or who will be willing to laugh after hearing that his student had had a wet dream about his wife? I'm probably the worst student you ever had, and that you'll probably ever have. I hope you've learned the valuable lessons, because I don't want to go through this again. In any case I will always remember the good times, but I will also remember when I got stuck in my house for two months in which my anxiety would not let me make it further than my street corner, when you came and help me return to society again. For all the things that I'm grateful, I lack the words to express them in the appropriate way. I hope you'll forgive me.

What could I say about the Iranian balls? What could I say that would summarize my gratitude? Because without summarizing it this would become a short story. Ali Pashaei went above and beyond to make my years in Barcelona the most pleasant. All I did for him was to teach him English slang, and the most disgusting, filthy English he had ever encountered. I do wish I made his stay a bit more pleasant too, but our friendship I believe was asymmetrical. My best guess is that Ali always felt he owed the universe (because that's one godless Iranian, if there ever was one) retribution for all the "blessings" he had received while he studied. By my calculations, he already paid with interest by taking me under his wings. And I specially thank him for picking me up at 4 am from a street in Barcelona after I had been crying over a girl. That's a friend by any definition, in any part of the world, in any world of the multiverse.

In my hard times, after the mental health issues had caught up with me, I made some friends who shared many beers with me. Tristan Whitmarsh, I'm forever in your debt for the countless nights when we discussed research, women, life and beyond. The company was mutual, but I do think I got bit over my half from our talks. Thank you for all the support and your friendship. My good friend Rida Sadek and your lovely wife Nardine, you provided a sane point of view in my once crazed up reality. My skills at writing cannot convey the complete message that I want to state. But even more I cannot thank you enough, Rida, for accompanying me to my second back surgery, when I was a cramp up bundle of nerves. I'm ever grateful to you and your incredibly wonderful family. I still want a couple of cooking recipes from your mother! And what to say about the amazing Veselin? My Barcelona experience would have been completely different without you; you made it better. Veselin would uplift my spirit and always make the end of my day better with good music, a cold beer and a great anecdote. He is not your average barman. And I am not your average customer. In his own words, and in his own personal trademark of tough love, I was "the adopted son he never wanted". And he was a great stepfather. Thank you.

For a person with such a bad history of relationships like me, there have been some couples that have helped me keep my hopes high. Examples of this are Arjan and Cata, and Hernán and Issis. Arjan is such a wonderful human being, that I should not begin to list his many attributes, in case anybody got jealous over my description of him. All I can say right now is that he has been and still is an inspiration to me. Cata, such a loving

and caring person, doesn't need the praises from the likes of me to know her worth; my pictorial archives of the time in Barcelona only has very few moments where she wasn't present. Hernán and Issis, are a unit so well-oiled it would be extremely hard to find them making a crank noise. I imagine they work so carefully at it nights to make the engine run so smoothly, they even find the time to adjust the dampers to make everyone else feel comfortable on the day to day ride. And I thank both couples for even taking the time to consider my mental health. I hope that with my fooling around and sometimes over the top "childish" jokes to have brought some laughter into your lives.

I want to send a special thank you to a couple of friends I met in some of the many houses I've lived. And I started sharing flats at 17! So many people have come and gone through those flats. But there are a three that stand out above the rest: Said Ramírez, Don William Acosta and Don Alonso Amaya Angel. When I describe my years of living with Said, I always say that if we had been gay, we would have been the perfect couple. For Don Alonso I will always have love in my heart, for he encouraged me to follow my dreams, to make mistakes, to get back up again and keep on living, loving life and loving the road. Don William Acosta, a great friend, is highly responsible for me going into academia. He got me out from working in bars and to start teaching private lessons, and made me fall in love with teaching. Said Ramírez, he sat down with me almost every day after work, and encouraged me to keep on going. The problems I had seemed trivial to him, but he respected them, as they were important to me, and kept encouraging me to overcome them. For Said it was never too late to change clothes and go out for a beer in Las Ramblas. And besides, cooking with him was never a task or chore us single guys had to do, but a kitchen experiment. I have nothing but gratitude for him for all his moral support throughout the years we live together.

The road took me to places and labs I never thought it would be necessary for me to go through to do a PhD. But I met people, incredible people. All of whom I cannot name here. Maybe in my autobiography. The PMO from the CISTIB was such a great bunch of people, to whom I'm ever so grateful for helping me solve even the most ridiculous problems; for example Milton Hoz de Villa helping remove a virus from my personal laptop (not a trivial or ridiculous problem) on a Sunday. To the group of developers that also contributed greatly to the completion of this thesis. To all the people from the CISTIB, to all of those who have come and gone, a huge hug and a big thank you. I would also like to thank Dr. Frank Sachse and his lovely wife Denise, for opening the doors of their house and making me feel as part of their family during my research stay in Salt Lake city. Thank you Frank for all your encouragement and for being so patient in the making of this thesis.

The "lab" always presented me with extraordinary persons, whose insight into my work is deeply appreciated, just like their support into my personal life like Bart Bijnens, Constantine Butakoff, Ruben Cardenes, Emma Muñoz, Viviana Zimmerman, Mathieu de Craene. I send you all a huge thank you and a big hug. The prequel to this road story includes so many people, it would become a different saga, and one thing I've learned from George Lucas is that many times a story it's better off alone without commentaries.

But even so, my study group from my undergraduate degree deserves a mention here. Lina Ramírez, Luisa García and Roberto Mosquera Escobar, were instrumental in helping me shape my mind and in encouraging me to pursue other types of dreams, off from the industry. Much love and appreciation for them all.

To my family, who has supported me throughout the years, my blood family who are always worried about me, I love you. From my earliest memory I recall my father studying in the living room table. And through example, never through imposition, I learned to study. I thank you for respecting my wishes, and thank you for funding unconditionally within your means and in your own way my path; different from your own, but mine alone. Thank you for being there during my mistakes, and during those times I had to retreat to gather the troops. I am so blessed to have such care from you, and I am also blessed to have had such fortune in my “familia del corazón”. To Rosalba . . . thank you for loving me. Thank you for loving our son.

To all of you . . . gracias totales.